

**ANALYSIS OF COAXIAL BOREHOLE HEAT EXCHANGER FOR GEOTHERMAL  
HEAT AND POWER**

by

Sajjan Pokhrel

B.E., Tribhuvan University, 2013

M.Sc., Wright State University, 2017

A THESIS SUBMITTED IN PARTIAL FULFILLMENT OF  
THE REQUIREMENTS FOR THE DEGREE OF

DOCTOR OF PHILOSOPHY

in

THE FACULTY OF GRADUATE AND POSTDOCTORAL STUDIES

(Mining Engineering)

THE UNIVERSITY OF BRITISH COLUMBIA

(Vancouver)

March 2024

© Sajjan Pokhrel, 2024

The following individuals certify that they have read, and recommend to the Faculty of Graduate and Postdoctoral Studies for acceptance, the dissertation entitled:

Analysis of coaxial borehole heat exchanger for geothermal heat and power

submitted by Sajjan Pokhrel in partial fulfillment of the requirements for

the degree of Doctor of Philosophy

in Mining Engineering

**Examining Committee:**

Seyed Ali Ghoreishi-Madiseh, Assistant Professor, Mining Engineering, UBC  
Supervisor

Scott Dunbar, Professor, Mining Engineering, UBC  
Supervisory Committee Member

John Steen, Associate Professor, Mining Engineering, UBC  
Supervisory Committee Member

Roger Beckie, Professor, Earth, Ocean, and Atmospheric Sciences, UBC  
University Examiner

Bern Klein, Professor, Mining Engineering, UBC  
University Examiner

## **Abstract**

Decarbonization of heat and electricity generation through geothermal energy is increasing, thanks to its universal availability and base load capacity. Although geothermal energy has several advantages compared to other renewable energy sources, more research is necessary to understand the fluid flow and heat transfer processes in diverse geological formations. These geological formations can be complex due to the variability of rock/soil properties, fluid presence, and fluid movement. Heat exchangers employed in such systems can reach thousands of meters, posing challenges for field-test experiments. In addition, mathematical modeling of such systems is a challenging task.

This dissertation is based on two geothermal projects; one focused on power generation and the other on heating. Both projects employ either a coaxial borehole heat exchanger (a single coaxial borehole) or a system of coaxial borehole heat exchangers. For geothermal power, a field-test experiment is carried out in a high-temperature resource well with a thermal gradient of  $0.4^{\circ}\text{C}/\text{m}$ . Experimental results are analyzed and rock properties are measured. In addition, a numerical model is developed to replicate the 500-meter deep field-test experiment. The developed numerical model is validated with the experimental data and is used to understand the subsurface behavior of the geothermal reservoir. Additionally, the performance of the heat exchanger under the complex geological formation, accounting for the presence of subsurface fluid flow, is evaluated. For geothermal heating, a numerical model is developed to study the heat transfer characteristics of a solar-geothermal heating system. The developed numerical model solves the heat and mass transfer process in a rectangular array of 450 coaxial boreholes. It also accounts for energy generation in solar thermal collectors and thermal demand on buildings. The numerical model is used to study energy injection into boreholes, energy extraction from boreholes, thermal

interactions between boreholes, thermal losses from the system, and the performance of the solar-geothermal heating system.

The results showed that subsurface fluid flow has a significant impact on the energy output from geothermal systems. Solar-geothermal heating systems have good potential to decarbonize space and water heating applications in Canada.

## **Lay Summary**

Geothermal energy can overcome intermittent issues of most other renewable sources such as wind and solar. Although geothermal energy is globally available and has a broad range of applications, it has not received adequate attention for its potential contributions to global decarbonization. This dissertation analyzes the performance of a specific type of heat exchanger – coaxial borehole heat exchanger – used in geothermal energy extraction and subsurface thermal energy storage systems. The study includes experimental and numerical analysis of a 500-meter deep geothermal extraction system and numerical analysis of shallow solar-geothermal system. Various subsurface conditions are considered for the installation of heat exchangers, considering the presence or absence of fluid and fluid movement. The key contribution of this research is the development of a numerical tool capable of predicting the behavior of complex geothermal reservoirs.

## Preface

This thesis presents both experimental and numerical evaluations of a coaxial borehole or a system of coaxial boreholes for geothermal heat and power. Four journal articles are the outcomes of this work, and an additional journal article is currently being prepared, in addition to some conference proceedings and presentations. I, Sajjan Pokhrel, am the first author of all the publications.

The experimental results presented in Chapter 3 and Chapter 4 were obtained from Prof. Atsushi Sainoki. I was solely responsible for the analysis of the experimental data, development of the numerical model, conducting validation, performing data analysis, and drafting the original manuscript under the supervision of Prof. Seyed Ali Ghoreishi-Madiseh. Prof. Seyed Ali Ghoreishi-Madiseh also contributed to reviewing the published manuscript from these chapters.

Journal publications from these chapters include:

1. **Pokhrel, S.**, Sasmito, A. P., Sainoki, A., Tosha, T., Tanaka, T., Nagai, C., & Ghoreishi-Madiseh, S. A. (2022). Field-scale experimental and numerical analysis of a downhole coaxial heat exchanger for geothermal energy production. *Renewable Energy*, 182, 521-535.
2. **Pokhrel, S.**, Sasmito, A. P., Sainoki, A., Tosha, T., Tanaka, T., Nagai, C., Samea, P., & Ghoreishi-Madiseh, S. A. (2023). Geothermal energy extraction from natural porous rocks: s study on field testing, experimental analysis, and numerical simulation with the presence of seepage. (under preparation).

The following is the article publications from Chapter 5. Not all sections of these publications are included in this thesis to make the document coherent. The 1+3D numerical model was conceptualized by Seyed Ali Ghoreishi-Madiseh. I was solely responsible for the 1+3D numerical

model development in Python, its validation, data analysis, and drafting of the manuscripts. Prof. Seyed Ali Ghoreishi-Madiseh contributed to reviewing all these manuscripts.

3. **Pokhrel, S.**, Amiri, L., Poncet, S., & Ghoreishi-Madiseh, S. A. (2023). Reduced order 1+ 3D numerical model for evaluating the performance of solar borehole thermal energy storage systems. *Journal of Energy Storage*, 66, 107503.
4. **Pokhrel, S.**, Amiri, L., Zueter, A., Poncet, S., Hassani, F. P., Sasmito, A. P., & Ghoreishi-Madiseh, S. A. (2021). Thermal performance evaluation of integrated solar-geothermal system; a semi-conjugate reduced order numerical model. *Applied Energy*, 303, 117676.
5. **Pokhrel, S.**, Amiri, L., Poncet, S., Sasmito, A. P., & Ghoreishi-Madiseh, S. A. (2022). Renewable heating solutions for buildings; a techno-economic comparative study of sewage heat recovery and solar borehole thermal energy storage system. *Energy and Buildings*, 259, 111892.

# Table of Contents

<b>Abstract</b> .....	<b>iii</b>
<b>Lay Summary</b> .....	<b>v</b>
<b>Preface</b> .....	<b>vi</b>
<b>Table of Contents</b> .....	<b>viii</b>
<b>List of Tables</b> .....	<b>xiii</b>
<b>List of Figures</b> .....	<b>xiv</b>
<b>List of Symbols</b> .....	<b>xviii</b>
<b>List of Abbreviations</b> .....	<b>xxi</b>
<b>Acknowledgments</b> .....	<b>xxiii</b>
<b>Dedication</b> .....	<b>xxv</b>
<b>Chapter 1: Introduction</b> .....	<b>1</b>
1.1 Renewables and future goals .....	2
1.2 Geothermal energy .....	3
1.3 Limitations of current geothermal energy systems.....	5
1.4 Towards closed-loop geothermal.....	6
1.5 State of the art – closed loop geothermal.....	8
1.6 Technical challenges of closed-loop geothermal .....	10
1.7 Thesis objectives .....	10
1.8 Thesis overview .....	11
<b>Chapter 2: Literature Review</b> .....	<b>13</b>
2.1 Geothermal history.....	13
2.2 Geothermal energy and mining.....	14

2.3	Closed-loop geothermal systems .....	15
2.4	Closed-loop heat exchangers .....	18
2.4.1	Experimental studies.....	20
2.4.2	Analytical studies.....	22
2.4.3	Numerical studies.....	22
2.4.3.1	Single borehole numerical modeling .....	23
2.4.3.2	Multiple boreholes numerical modeling .....	25
2.5	Contributions to the existing literature .....	27

**Chapter 3: Experimental Analysis of a Field-Scale Coaxial Heat Exchanger for Geothermal Power.....29**

3.1	Introduction.....	30
3.2	Methodology .....	30
3.3	Experimental results.....	36
3.4	Rock properties analysis .....	44
3.5	Conclusions.....	49

**Chapter 4: Numerical Simulation of a Field-Scale Coaxial Heat Exchanger for Geothermal Power.....50**

4.1	Introduction.....	50
4.2	Methodology .....	51
4.2.1	Geometry and meshing .....	51
4.2.2	Initial and boundary conditions .....	53
4.2.2.1	Porous media boundary conditions.....	55
4.2.3	Governing equations .....	56

4.2.4	Assumptions of the numerical model .....	58
4.2.5	Numerical scheme.....	60
4.3	Seepage calibration and validation process .....	61
4.4	Numerical results validation and error analysis.....	62
4.5	Discussion on seepage velocities .....	66
4.6	Results.....	71
4.6.1	Effect of seepage.....	71
4.6.2	Parametric analysis .....	73
4.6.2.1	Effect of flowrate .....	73
4.6.2.2	Effect of inlet temperature .....	75
4.6.2.3	Effect of ground thermal conductivity.....	78
4.6.2.4	Effect of insulator pipe thermal conductivity .....	81
4.7	Conclusions.....	83
<b>Chapter 5: Reduced Order 1+3D Numerical Model for Evaluating the Performance of</b>		
<b>Coaxial Boreholes in Solar Geothermal Heating System.....</b>		<b>84</b>
5.1	Introduction.....	85
5.2	System schematics .....	86
5.3	Building description.....	87
5.4	Methodology.....	88
5.4.1	1+3D model development.....	88
5.4.1.1	Governing equations .....	90
5.4.1.2	Initial and boundary conditions .....	92
5.4.2	Conjugate model development .....	94

5.4.3	Building thermal demand.....	96
5.4.3.1	Fresh air intake.....	97
5.4.3.2	Envelope thermal loss.....	97
5.4.3.3	Hot water demand.....	97
5.4.4	Solar field design.....	99
5.4.5	Economic analysis.....	103
5.4.6	Integrated model development.....	105
5.4.7	Grid independence test.....	108
5.5	Model validation.....	109
5.5.1	Single borehole validation.....	109
5.5.2	Multiple boreholes validation.....	110
5.6	Computational cost.....	111
5.7	Results.....	112
5.7.1	Base case scenario.....	112
5.7.2	Parametric analysis.....	115
5.7.2.1	Effect of depth variation.....	115
5.7.2.2	Effect of center-center distance variation.....	118
5.7.2.3	Effect of delta temperature ( $\Delta T$ ) variation.....	120
5.8	Economic and environmental analysis.....	122
5.8.1	Capital expenditure (CAPEX).....	122
5.8.2	Cost of energy (COE).....	123
5.8.3	Cost savings and global perspective.....	125
5.8.4	Payback period.....	126

5.9	Conclusions.....	128
<b>Chapter 6: Discussion of Findings.....</b>		<b>130</b>
6.1	Overview of research problems .....	130
6.2	Major findings.....	131
6.3	Contribution to knowledge .....	133
6.4	Limitations and future work.....	135
<b>References.....</b>		<b>138</b>
<b>Appendices.....</b>		<b>154</b>
	Appendix A : Fluent UDF.....	154
	Appendix B : Seepage velocity calibration.....	167
	Appendix C :Other publications .....	172

## List of Tables

Table 3-1 Properties of rocks measured in the lab.....	46
Table 4-1 Material properties used in the simulation. ....	55
Table 4-2 Grid independence test results.....	61
Table 4-3 Calibrated seepage velocity with depth.....	66
Table 5-1 Solar thermal collector system parameters.....	102
Table 5-2 Cost estimation for the natural gas heating system. ....	103
Table 5-3 Cost estimation for Solar thermal collector system.....	104
Table 5-4 Cost estimation for BTES system.....	104

## List of Figures

Figure 1-1 Global emissions scenarios (Source: IEA, 2021).....	2
Figure 1-2 Global sectoral emissions, 2021 [4].....	3
Figure 1-3 Enhanced geothermal system 1. Reservoir 2. Pump house 3. Heat exchanger 4. Turbine hall 5. Production well 6. Injection well 7. Hot water to district heating 8. Porous sediments 9. Observation well 10. Crystalline bedrock [5].....	4
Figure 1-4 Conventional geothermal system (a) for heat and (b) for power generation [7].....	6
Figure 1-5 Closed-loop geothermal (a) for space heating [8], (b) for power generation [9].....	7
Figure 1-6 Closed-loop geothermal: A new power category.....	7
Figure 1-7 Next-generation deep drilling technology [16]. .....	9
Figure 2-1 First commercial geothermal power plant, 250kW, Larderello, Italy, 1913. [17] .....	13
Figure 2-2 Mining and geothermal map on a global scale [8].....	15
Figure 2-3 Closed-loop geothermal for district heating [12].....	17
Figure 2-4 Closed-loop geothermal for power generation [25].....	17
Figure 2-5 Schematics of coaxial BHE (left) and U-tube BHE (right).....	19
Figure 3-1 Drilling equipment installation set-up for the experiment. ....	32
Figure 3-2 Drilling procedure during the experiment.....	32
Figure 3-3 Detailed dimension of the borehole (OD and ID are the outer and inner diameters of the steel pipe; and $\emptyset$ is the outer diameter of the drill hole). ....	33
Figure 3-4 Schematics of the experiment. ....	34
Figure 3-5 Temperature control unit.....	35
Figure 3-6 Experiment setup during the water circulation test.....	35

Figure 3-7 Estimation of well equilibrium temperature from Horner plot method for a depth of 350 m. ....	38
Figure 3-8 Undisturbed ground temperature and corresponding saturation temperature. ....	40
Figure 3-9 Outlet temperature results during water circulation test. ....	40
Figure 3-10 Experimental temporal evolution of ground temperature during extraction.....	42
Figure 3-11 Experimental temporal evolution of ground temperature during recovery.....	43
Figure 3-12 Comparing initial temperature with the last day of extraction and the first and last day of recovery. ....	43
Figure 3-13 Rock samples tested: (a and c) vuggy silica; and (b and d) massive silica (Courtesy: Professor Sainoki from Kumamoto University). ....	45
Figure 3-14 Thermal conductivity and specific heat capacity of vuggy silica (a) and massive silica (b). ....	48
Figure 4-1 Numerical model construction: (a) Different domains considered in the analysis (geometry not to scale); (b) Meshing scheme at the inlet and outlet of the CBHE; and (c) Generated hexahedral mesh of the whole domain. ....	52
Figure 4-2 Comparing outlet temperatures: experimental vs numerical results. ....	64
Figure 4-3 Validation results during extraction on different days.....	65
Figure 4-4 Validation results during recovery on different days.....	66
Figure 4-5 Map of Beppu Hydrothermal Field and red STAR sign is the well location. Thick curves show isotherms in °C at 100 m below sea-level. Shaded areas are two-phase zones. Dashed lines A and K are the Asamigawa and the Kamegawa faults respectively, and dashed line N is an unnamed fault. Elevation contours (m) above mean sea level [112]......	68
Figure 4-6 Comparing outlet temperature with and without the calibrated seepage. ....	72

Figure 4-7 Parametric study on flowrate variation. ....	75
Figure 4-8 Parametric study results on inlet water temperature. ....	78
Figure 4-9 Parametric study results on thermal conductivity of ground. ....	81
Figure 4-10 Parametric study on insulator pipe thermal conductivity.....	82
Figure 5-1 Solar-geothermal heating system schematics.....	87
Figure 5-2 (a) Co-axial borehole heat exchanger during heat extraction, (b) top and isometric view of the three-dimensional geometry of the BTES domain.....	89
Figure 5-3 Top discretized view of the domain section with a borehole in it (left) and a conceptual figure representing source and non-source term elements (right). ....	90
Figure 5-4 (a) Domain discretization of a conjugate model, and (b) magnified top view with the four boreholes inlet. ....	96
Figure 5-5 Annual thermal power and energy demand of the building.....	99
Figure 5-6 Available solar irradiation for the studied location.....	100
Figure 5-7 Solar thermal collector efficiency for different HTF temperatures. ....	100
Figure 5-8 Integrated numerical model (a) Conceptual diagram and (b) Flowchart. ....	107
Figure 5-9 Outlet temperature variation after 124 hours with different mesh sizes in the axial and radial directions.....	109
Figure 5-10 Temporal evolution of the outlet temperature for a single borehole. Comparison between the present numerical result and field test experimental data from Morita et al. ....	110
Figure 5-11 Temporal evolution of the outlet temperature for multiple boreholes. Comparison between the developed 1+3D numerical code and results from ANSYS Fluent.....	111

Figure 5-12 Temporal evolutions of the (a) Cumulative total energy, (b) Solar thermal collector efficiency with time, (c) BTES injection inlet temperature and extraction outlet temperature, and (d) Average ground temperature. Results obtained by the 1+3D numerical model. .... 114

Figure 5-13 Temporal evolutions of the (a) Average BTES temperature, (b) Borehole outlet temperature during extraction, (c) Total solar yield from solar thermal collector system, and (d) BTES thermal losses. Results obtained by the 1+3D numerical model. .... 117

Figure 5-14 Temporal evolutions of the (a) Average BTES temperature, (b) Borehole outlet temperature during extraction, (c) Total solar yield from solar thermal collector system, and (d) BTES thermal losses. Results obtained by the 1+3D numerical model for 3 values of the center-center distance between 2 boreholes. .... 120

Figure 5-15 Temporal evolutions of the (a) Collector outlet temperature and (b) BTES outlet temperature during the extraction cycle. Results obtained by the 1+3D numerical model for 2 values of the temperature change during the injection phase. .... 121

Figure 5-16 Capital costs in US \$ of (left) Natural gas heating system, (right) solar-geothermal system. .... 123

Figure 5-17 COE comparison for two systems. .... 124

Figure 5-18 Annual cost savings for the solar-geothermal system (the star sign denotes the current energy rates). .... 126

Figure 5-19. The payback period for capital costs of US\$ 700/kW of installed capacity (the star sign denotes the current energy rates). .... 127

Figure 5-20 Payback period for capital costs of US\$ 805/kW of installed capacity (the star sign denotes the current energy rates). .... 127

## List of Symbols

### *Greek symbols*

$\eta$	<i>Efficiency</i>
$\mu$	<i>Viscosity (<math>N s m^{-2}</math>)</i>
$\rho$	<i>Density (<math>kg m^{-3}</math>)</i>
$\sigma$	<i>Stefan-Boltzmann constant (<math>W m^{-2} K^{-4}</math>)</i>
$\tau$	<i>Tensor</i>
$\varphi$	<i>Porosity</i>
$\mathcal{E}$	<i>Emissivity (<math>Js^{-1}m^{-2}K</math>)</i>
$\epsilon$	<i>Dissipation rate (<math>m^2 s^{-3}</math>)</i>
$\nabla$	<i>Gradient</i>

### *Other symbols*

$A$	<i>Contact area of heat exchanger (<math>m^2</math>)</i>
$a$	<i>Thermal diffusivity (<math>m^2 s^{-1}</math>)</i>
$C$	<i>Specific heat capacity (<math>J Kg^{-1} K^{-1}</math>)</i>
$D$	<i>Diameter (<math>m</math>)</i>
$d$	<i>Particle or pore diameter (<math>m</math>)</i>
$G$	<i>Solar irradiance (<math>W m^{-2}</math>)</i>
$\vec{g}$	<i>Acceleration due to gravity (<math>m s^{-2}</math>)</i>
$h$	<i>Convective heat transfer coefficient (<math>W m^{-2} K^{-1}</math>)</i>
$K$	<i>Absolute permeability (<math>m^2</math>)</i>

$KE$	<i>Turbulent kinetic energy (<math>m^2 s^{-2}</math>)</i>
$k$	<i>Thermal conductivity (<math>W m^{-1} K^{-1}</math>)</i>
$L$	<i>System length (m)</i>
$l$	<i>Representative elementary length (m)</i>
$\dot{m}$	<i>Mass flowrate (<math>kg s^{-1}</math>)</i>
$N$	<i>Number of days or number of solar collectors</i>
$Nu$	<i>Nusselt number</i>
$p$	<i>Pressure (<math>N m^{-2}</math>)</i>
$Pr$	<i>Prandtl number</i>
$\dot{Q}$	<i>Rate of heat transfer (W)</i>
$R$	<i>Thermal resistance (<math>m^2kW^{-1}</math>)</i>
$r$	<i>Radius (m)</i>
$S_h$	<i>Source term</i>
$t$	<i>Time(s)</i>
$T$	<i>Temperature (K)</i>
$t'$	<i>Time-scale (s)</i>
$v$	<i>Velocity (<math>m s^{-1}</math>)</i>

### *Subscripts*

$A$	<i>Ambient</i>
$b$	<i>Base reference</i>
$c$	<i>Collector</i>
$c,g$	<i>Collector gross area</i>

<i>eff</i>	<i>Effective</i>
<i>f</i>	<i>Fluid</i>
<i>f1</i>	<i>Initial temperature</i>
<i>f2</i>	<i>Final temperature</i>
<i>f_a</i>	<i>Fresh air</i>
<i>fl</i>	<i>Floor</i>
<i>fs</i>	<i>Fluid-solid</i>
<i>g</i>	<i>Ground</i>
<i>h_l</i>	<i>Heat loss</i>
<i>h_w</i>	<i>Hot water</i>
<i>i</i>	<i>Initial</i>
<i>p</i>	<i>Pressure</i>
<i>pc</i>	<i>Per collector</i>
<i>r</i>	<i>Roof</i>
<i>s</i>	<i>Solid</i>
<i>sol</i>	<i>Solar</i>
<i>STER</i>	<i>Storage to extraction</i>
<i>Sur</i>	<i>Surrounding</i>
<i>T</i>	<i>Turbulent</i>
<i>tot</i>	<i>Total</i>
<i>w</i>	<i>Wall</i>
<i>win</i>	<i>Window</i>

## List of Abbreviations

2D	Two dimensional
3D	Three dimensional
BHE	Borehole Heat Exchanger
BTES	Borehole Thermal Energy Storage
CAD	Canadian Dollar
CAPEX	Capital Expenditure
CBHE	Coaxial Borehole Heat Exchanger
C-C	Centre to Centre distance
CFD	Computational Fluid Dynamics
CH <sub>4</sub>	Methane
CO <sub>2</sub>	Carbon dioxide
COE	Cost of Energy
COP	Coefficient of Performance
DTS	Distributed Temperature Sensor
DOE	Department of Energy
GJ	Gigajoules
GHG	Green House Gas
GeoDH	Geothermal District Heating
GSHP	Ground Source Heat Pump
Gt	Gigatons
GW <sub>e</sub>	Gigawatts of electric energy

GW	Gigawatt
GW <sub>TH</sub>	Gigawatts of thermal energy
HDD	Heating Degree Days
HLF	Heat Lost Factor
HTF	Heat Transfer Fluid
IEA	International Energy Agency
LFA	Laser Flash Apparatus
LMTD	Log Mean Temperature Difference
MW	Megawatt
MWe	Megawatts of electric energy
PV	Photovoltaics
ROM	Reduced Order Models
SF	Solar Fraction
TJ	Terajoules
TWh	Terawatt hour
UDF	User-Defined Function
USA	United States of America
US\$	United States Dollar
US¢	United States Cent

## **Acknowledgments**

I extend my heartfelt gratitude to my thesis supervisor, Prof. Ali Madiseh, for his unwavering support and mentorship throughout my study here at UBC. His financial and moral support during these years has been invaluable, greatly aiding my academic journey. His continuous inspiration and empowerment have driven me to continually improve and strive for excellence.

I would like to express my sincere appreciation to all the committee members of my thesis; Scott Dunbar and John Steen, for providing valuable feedback that significantly enhanced the quality of this work.

A special mention of gratitude goes to Prof. Agus P. Sasmito from McGill University for his expert guidance throughout various phases of the thesis. I am grateful to Prof. Atsushi Sainoki from Kumamoto University for providing me with the opportunity to collaborate on the geothermal project and for sharing the experimental test results. I wish to acknowledge Prof. Leyla Amiri for her insightful guidance during our collaborative projects. I would also like to extend my thanks to all the co-authors of the published manuscripts.

I am deeply indebted to the International Research Organization for Advanced Science and Technology (IROST) for sponsoring my tenure as a visiting research fellow in Japan during the project. Additionally, I express my sincere appreciation to the MITACS Accelerate Research Internship Award and the UBC Transdisciplinary Fellowship for Climate Emergency Award for their support during my Ph.D. studies.

My gratitude also goes to Adel Ahmadihosseini for his invaluable assistance in conducting the experimental work on rock thermal properties. I wish to acknowledge all the members of the Advanced Mine Energy Systems (AMES) lab at UBC Mining Engineering department for their collaborative efforts.

I would like to extend special thanks to my parents, whose unwavering support has been instrumental throughout my educational journey and has brought me to this point. Additionally, I am grateful to my two brothers, Santosh and Saroj, for their constant presence during both the good and challenging times.

Last but not least, I would like to acknowledge my wife, Jharana Poudel, for her unconditional love, infinite understanding, patience, and unwavering support. I am deeply grateful to her for taking care of our baby during my busy schedule over the past six months. This achievement is also yours! And to our son, Ardhiv, for giving us reasons to smile at all the small things that matter. I love you both!

Sajjan Pokhrel

Vancouver, Canada

September 2023

*~ To my family ~*

## Chapter 1: Introduction

“The most important thing to know about prehistoric humans is that they were insignificant animals with no more impact on their environment than gorillas, fireflies or jellyfish.”

– Yuval Noah Harari [1].

From primitive humans to modern Homo sapiens, even considering just the past 50 years, the population of the entire planet has doubled [2], and so too have greenhouse gas (GHG) emissions [3]. Today, global fossil fuel consumption exceeds 100 million barrels per day, emitting over 40 gigatons (Gt) of CO<sub>2</sub> each year [4]. There are also multiple other spillover effects on health and the environment. The repercussions are not limited to specific areas such as offshore oil drilling in the Arctic and oil sands mining in Canada, but affect every individual around the world. Hence, to avert the worst outcomes of climate change, countries should unite for a shared goal of achieving net zero emissions by 2050. This can only be accomplished by reducing CO<sub>2</sub> emissions by 40 Gt/year, as shown in Figure 1-1. Based on Figure 1-1, even if all the countries achieve their pledged emission reductions, only 45% of the target reduction will be achieved.

It is also important to acknowledge that approximately one-third of today's emissions come from electricity and heat (Figure 1-2). Therefore, it is of utmost importance that we prioritize decarbonizing heat and electricity to create a cleaner and more sustainable future for us and future generations. The path ahead is challenging but achievable with strong will and determination. This thesis presents research projects aimed at decarbonizing the heat and electricity sectors through the utilization of renewable energy technology, particularly geothermal energy.

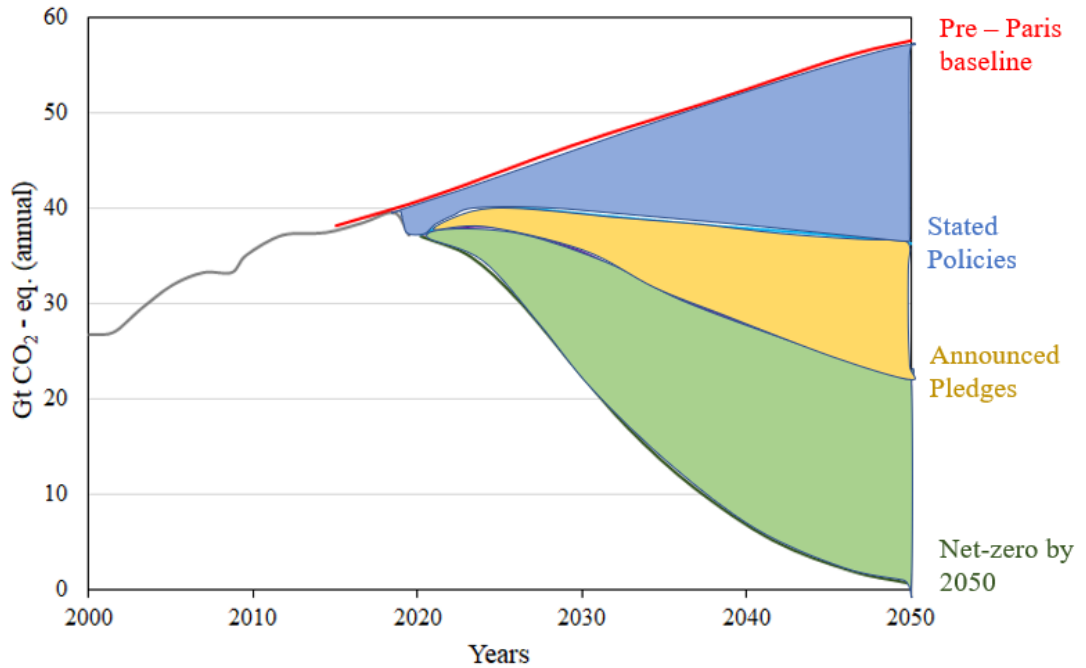
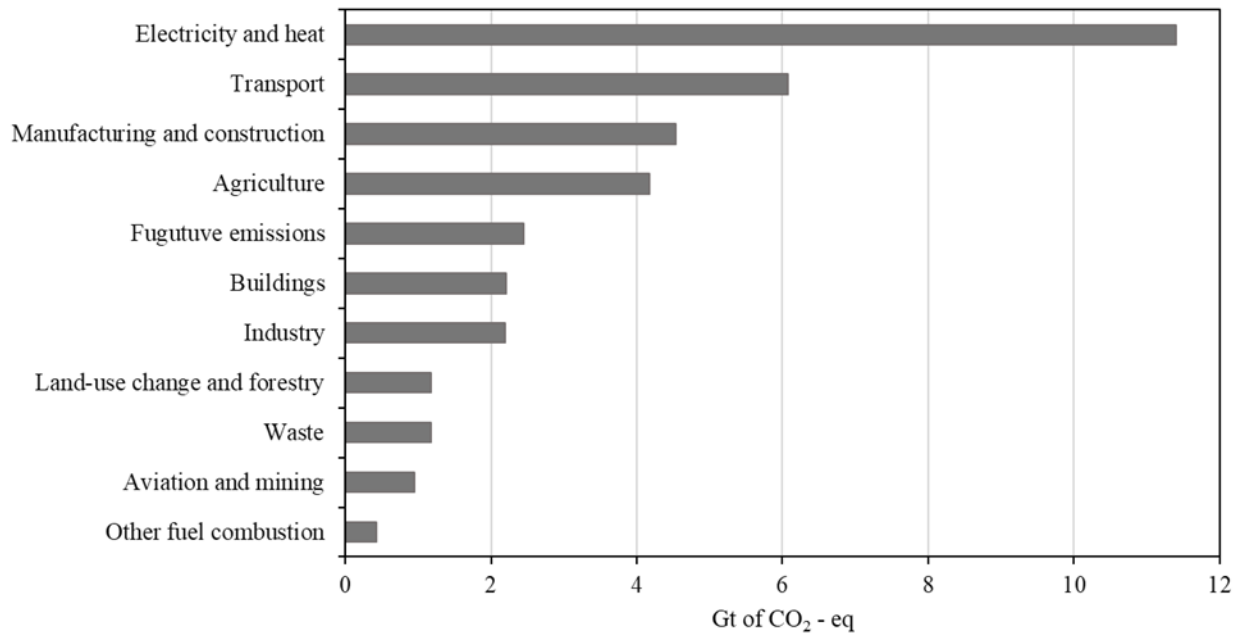


Figure 1-1 Global emissions scenarios (Source: IEA, 2021).

## 1.1 Renewables and future goals

Renewable energy sources are emerging as a viable alternative to traditional energy sources to counter the environmental and economic consequences of fossil fuels. Renewable energy sources such as solar and wind power have shown great promise, but they come with their own set of challenges, the largest of which is intermittent availability. A small portion of the Sahara Desert is enough to power the world by tapping solar energy with photovoltaics (PV) collectors. However, the story raises the question of feasibility. Solar energy needs to be stored overnight, but no current battery storage system can store enough energy to supply global demand for an hour. This story is same for wind technology. This realization has prompted the search for renewable energy technologies that can serve as a base load, around the clock, Geothermal energy has emerged as a potential candidate.



**Figure 1-2 Global sectoral emissions, 2021 [4].**

## 1.2 Geothermal energy

Geothermal energy can overcome the intermittency issue of wind and solar. Geothermal is a base load energy source, meaning it provides a constant supply of energy, is available 24/7, and is not affected by weather conditions. This also avoids the need for energy storage systems making it a reliable solution to the world energy needs. Another important advantage of geothermal is that, given the availability of a good geothermal gradient, it could be used for heat or electricity depending on the user needs. In many energy systems, meeting heating demand involves generating electricity and then converting it into heat, which reduces the overall efficiency of the system. However, the geothermal system is flexible and can be designed to produce either heat or electricity based on the end-user requirement. Colder countries such as Canada, could benefit from

direct heat from geothermal systems because space and water heating constitutes more than 80% of total energy in residential buildings, and a significant portion of heating in other sectors including manufacturing and mining.

Geothermal as the name suggests is a combination of two words: ‘geo’ and ‘thermal’, which means the heat from the earth. Thermal energy from the Earth’s core is utilized in the form of heat or electricity for end-use. Since ancient times, geothermal energy has been used for different applications such as natural hot water bathing and fish farming. However, more advanced technologies, such as geothermal power generation and direct heat utilization for different residential and industrial activities, have been used to tap geothermal energy for the past 100 years.

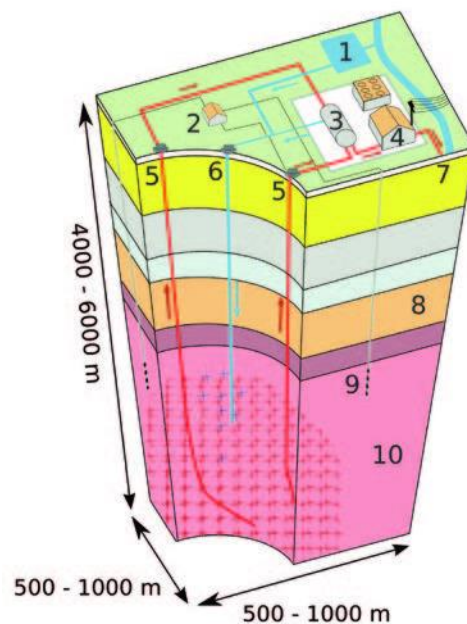


**Figure 1-3 Enhanced geothermal system 1. Reservoir 2. Pump house 3. Heat exchanger 4. Turbine hall 5. Production well 6. Injection well 7. Hot water to district heating 8. Porous sediments 9. Observation well 10. Crystalline bedrock [5].**

### **1.3 Limitations of current geothermal energy systems**

Geothermal energy, despite having several advantages over other renewable energy sources, a long history, and the installation of the first commercial power plant in Italy in 1913, paradoxically generates very little power and energy. With a capacity of only 16 GWe and 107 GW<sub>TH</sub>, [6] geothermal lags significantly behind wind and solar energy, which each have a capacity of approximately 1000 GWe. This disparity of low geothermal harvesting is attributed to the limitations of current geothermal technology, which relies on a two-hole extraction-injection system. Figure 1-4 depicts schematics of open-loop geothermal systems in which hot geothermal fluid is recovered to power turbines or heat buildings before being injected back underground. However, the requirement for both geothermal fluid and high temperatures restricts its widespread application. Although deep regions of the earth have high temperatures, the presence of fluid is inconsistent. Such geothermal systems also present environmental concerns through changes to geothermal fluids and underground water systems due to the extraction of subsurface fluid. The corrosive properties of geothermal fluids also cause faster degradation of turbines, heat exchangers, and other machinery, reducing the effectiveness and lifespan. Consequently, the limitations of conventional geothermal energy raise concerns about its expandability and feasibility.

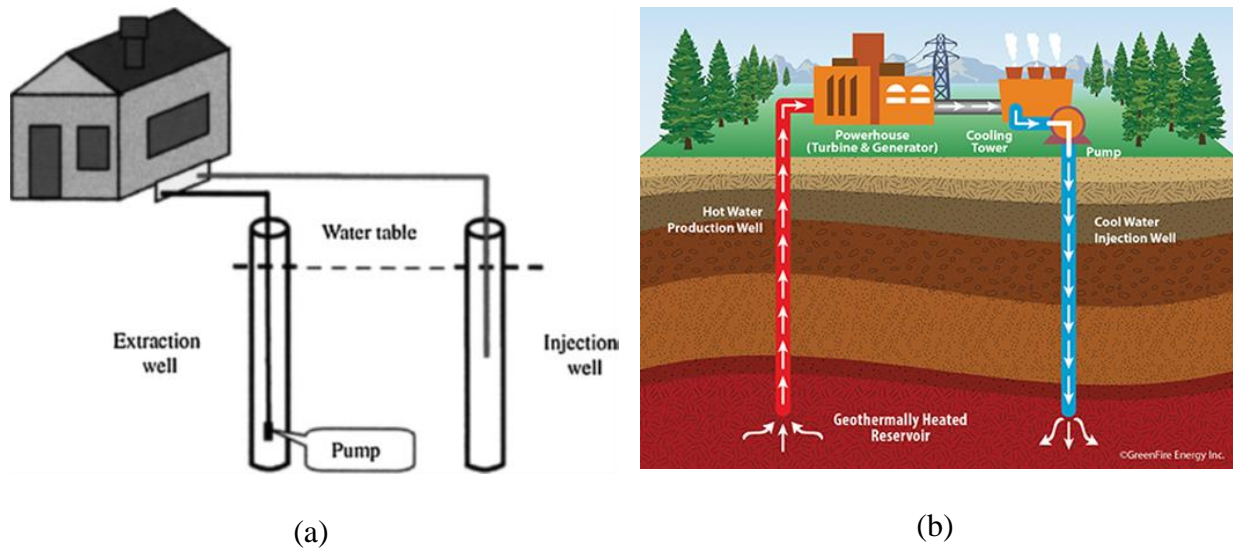


Figure 1-4 Conventional geothermal system (a) for heat and (b) for power generation [7].

#### 1.4 Towards closed-loop geothermal

In recent years, a groundbreaking advancement in geothermal energy has emerged: the closed-loop geothermal system. Figure 1-5 show closed-loop geothermal systems for heating and power generation. Figure 1-5(a) represents heating systems typically found at shallower depths, while Figure 5-1(b) illustrates power generation systems that can extend to depths of several kilometers. Unlike traditional methods, this innovative approach focuses on exchanging heat solely between the fluid in the geothermal heat exchanger and the subsurface fluid or solid mass, ensuring greater sustainability. These systems consist of a smaller surface footprint and does not necessitate a porous and permeable subsurface with geothermal fluid in it. Based on this principle, it also unlocks the universal and scalable potential of geothermal energy by harnessing the ubiquitous presence of heat beneath our feet. Figure 1-6 depicts closed-loop geothermal as the sole source of energy that is clean, scalable, and baseload - capable of providing consistent heat and power on

demand. With its scalability, reliability, and environmental friendliness, closed-loop geothermal has the potential to revolutionize the energy landscape in the coming decades.

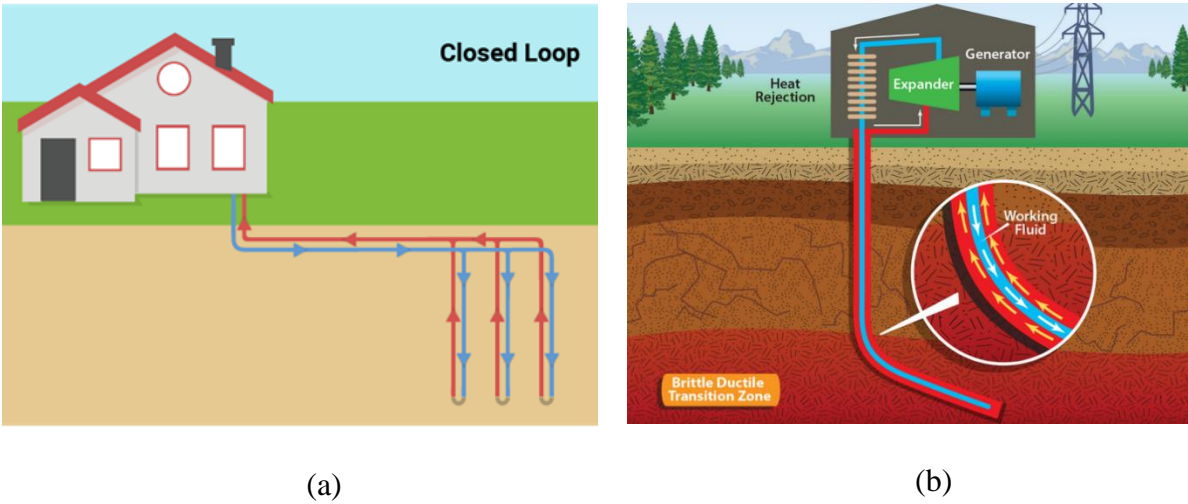


Figure 1-5 Closed-loop geothermal (a) for space heating [8], (b) for power generation [9].

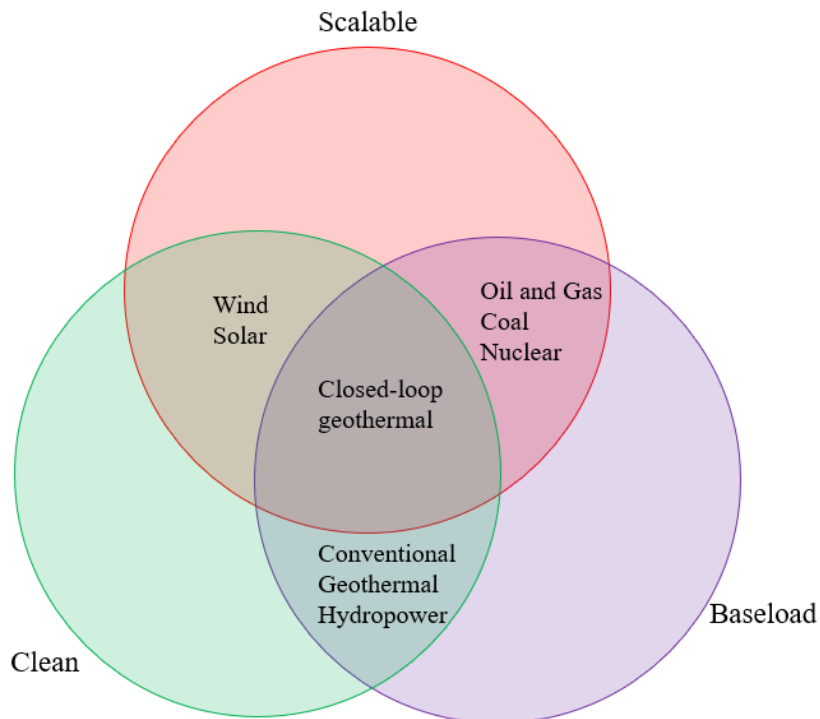


Figure 1-6 Closed-loop geothermal: A new power category.

## **1.5 State of the art – closed loop geothermal**

Closed-loop geothermal power generation systems are still in the early stages of development, with notable pioneer projects such as GreenFire Energy 1.2 MWe installation in the Coso geothermal field (2020) [10] and Eavor Technology 1 MW project in Alberta, Canada (2021) [11]. Another significant endeavor, backed by a 91.6 million euro grant from European innovation funding, involves an 8 MWe project currently under construction in Germany, reaching a depth of 4500 meters [12]. These modern geothermal systems have emerged relatively recently, contrasting with the century-long history of conventional geothermal methods. One remarkable aspect of closed-loop systems is their potential for repurposing abandoned oil and gas wells for energy extraction. The US Department of Energy (DOE) awarded US\$ 8.4 million for accessing geothermal potential from abandoned oil and gas wells in 2022 [13]. Over the past few years, more than a dozen start-ups have emerged, specializing in closed-loop geothermal technology.

Closed-loop geothermal heating, both at an individual level and on a larger scale for district heating, has garnered increased attention as well. While individual building heating using closed-loop geothermal systems has been in practice since the 1940s, the implementation of geothermal district heating projects has become a topic of significant discussion in recent times. Geothermal District Heating (GeoDH), utilizes the heat stored beneath the Earth surface to warm entire neighborhoods, municipalities, offices, and industrial buildings through a well-connected distribution network. A notable advancement in this field involves the integration of geothermal heating with solar thermal collectors, specifically designed for seasonal heating requirements in cold climatic regions such as Canada. In solar-geothermal systems, solar thermal energy is accumulated in boreholes during the summer, and subsequently utilized during the extended and

harsh winter period for space and water heating purposes. Noteworthy examples of solar-geothermal district heating initiatives include the Brødstrup solar-geothermal heating project in Denmark [14], serving 1500 customers, and the Drake Landing solar-geothermal community heating project in Alberta, providing heat to 52 detached houses [15].

For both closed-loop geothermal heat and power systems, a considerable chunk of total investment is dedicated to the drilling process. Certain companies are focusing on refining millimeter wave drilling technology [16], which utilizes radiation to access highly heated rock formations, as illustrated in Figure 1-7. The anticipated breakthrough in drilling technology holds the potential to revolutionize the next generation of closed-loop geothermal systems. By significantly reducing the levelized cost (cost over its entire lifecycle) of geothermal systems, it may even render them more cost-effective compared to most other energy technologies.

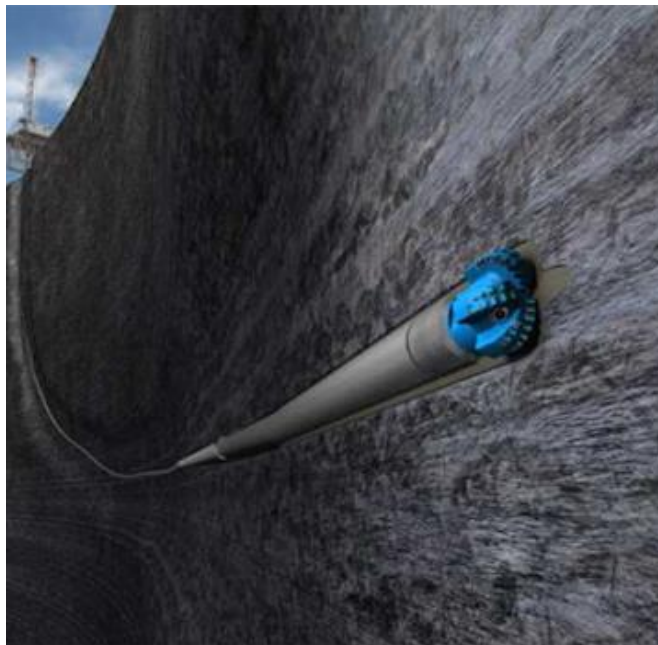


**Figure 1-7 Next-generation deep drilling technology [16].**

## **1.6 Technical challenges of closed-loop geothermal**

Closed-loop geothermal systems face two primary challenges: improving drilling techniques and maximizing thermal efficiency. The drilling challenge is also shared with the oil and gas industry, where dedicated professionals are diligently working to develop technology and reduce drilling costs. Another focal point involves comprehending heat transfer mechanisms, optimizing heat exchangers, and enhancing overall system performance. The focus of this thesis lies in investigating heat transfer and improving the efficiency of a specific type of heat exchanger used in closed-loop geothermal systems. The type of closed-loop heat exchanger discussed in this thesis is called a Coaxial Borehole Heat Exchanger (CBHE). This thesis endeavors to enhance the comprehension, efficiency, and feasibility of closed-loop geothermal systems through field-test experiments and the development of numerical models for a CBHE.

## **1.7 Thesis objectives**

This thesis aims to examine the long-term thermal performance of a CBHE in two distinct applications: geothermal power generation and geothermal heating.

For geothermal power, the research commences with experimental work and subsequently employs numerical modeling to outline a roadmap toward the ultimate objective, which is to evaluate the long-term performance of the system. The following specific objectives are proposed to accomplish this goal:

1. Analyze field-test experimental results obtained from the proposed geothermal power generation system utilizing a CBHE.
2. Measure and calibrate the thermophysical properties of subsurface rocks.

3. Develop and validate a numerical simulation model that accurately solves the conjugate heat and mass transfer phenomena in a CBHE and the porous, permeable rock layers.
4. Investigate the impact of seepage (groundwater flow) on the performance of the geothermal system.
5. To conduct sensitivity analysis on various design and operating parameters of a CBHE.

In the context of geothermal heating, this thesis focused on the application of CBHE for solar-geothermal heating in two sizeable residential buildings located in Ontario, Canada. This study develops a numerical model that could solve fluid flow and heat transfer mechanisms in a system of CBHEs used in solar-geothermal systems. Specific objectives of the work include:

1. Develop a numerical model to solve for heat and mass transfer processes in the system ( $N \times M$ , where  $N$  and  $M$  are integers) of CBHEs.
2. Extend the numerical model to incorporate solar thermal collectors and building load, and perform dynamic system-level modeling of the solar-geothermal heating system.
3. Perform dynamic simulations and design a solar-geothermal system for the considered building, considering their specific requirements and conditions.
4. Study the long-term performance analysis of solar-geothermal systems.

## **1.8 Thesis overview**

The next chapter of this thesis delves into a comprehensive literature review on the utilization of CBHE for various applications in heating and power generation. Chapter 2 is organized into three primary segments: experimental literature, analytical literature, and numerical literature. Following the literature review, Chapter 3 analyzes the findings of a field-test experiment conducted in Japan that utilized a CBHE for a proposed geothermal power system. Chapter 4

discusses the development of a Computational Fluid Dynamics (CFD) numerical model for the CBHE employed in this field-test experiment. The objective of the numerical model is to understand the reservoir behavior and analyze heat exchanger performance. Chapter 5 is about the use of CBHEs for solar-geothermal heating applications. This chapter presents the model development, design, and analysis of solar-geothermal systems for large-scale building heating applications. Finally, the conclusions of this work are presented in Chapter 6, encompassing key findings and design recommendations, followed by suggestions for future research endeavors.

## Chapter 2: Literature Review

### 2.1 Geothermal history

Extraction of geothermal energy for and by human use dates back to more than a thousand years ago where archaeological evidence suggests that the indigenous people used it for hot springs for both spiritual and practical reasons. However, the first successful pilot-scale electricity generation from geothermal sources took place in Italy in 1904 before Larderello, Italy became home to the first commercial geothermal power plant in 1913 [17]. After a few decades in the 1960s, with some advanced research and development, the United States became the major producer of geothermal power with the Geysers geothermal power plant generating 11 MW of electricity, the biggest at that time. Even today, the US leads the race of geothermal power generation with about 3.8 GW out of 16 GW generated globally [18]. According to IEA, in a net-zero scenario, by 2030, total geothermal power generation will increase to 330 TWh from 94 TWh today, an anticipated increase of more than 250% [19].

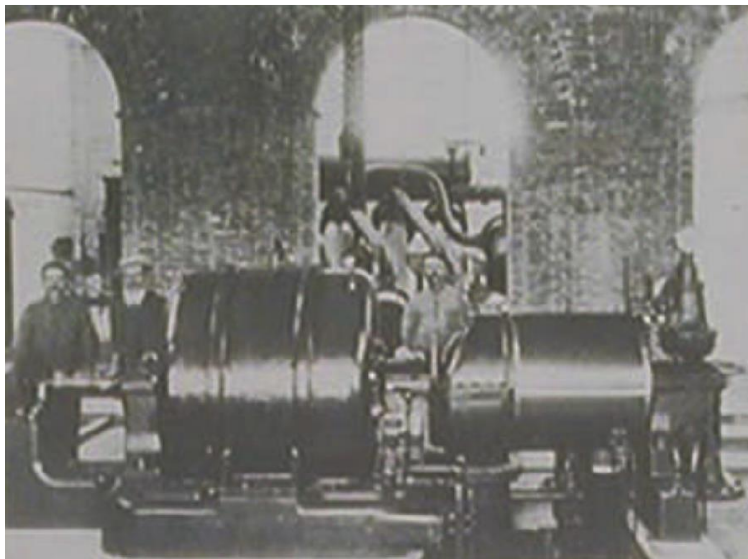


**Figure 2-1** First commercial geothermal power plant, 250kW, Larderello, Italy, 1913. [17]

## 2.2 Geothermal energy and mining

This section analyses the connections between the mining sector and the potential use of geothermal resources for different mining activities. Mining is one of the most energy-intensive industries emitting about 4 to 7 % of global industrial greenhouse gas (GHG) today [20]. There is a great potential to supply renewable energy to mining activities thanks to the geothermal potential near mine sites. The reason is that precious metals such as gold, copper, and silver tend to precipitate and deposit in response to the boiling and mixing of deep geothermal fluids. Areas with co-occurrence of mineral deposits and geothermal potential are illustrated in Figure 2-2. This picture is adapted from Patsa et al. [21] and portrays worldwide locations of current geothermal power stations, global mine locations, and smelter operations around the world. Some of the high-opportunity areas include the west coast of the USA, Central America, Chile, Peru, and East Africa. For example, California and Nevada have a total of 64 geothermal power plants with a generation potential of 3086 MW of electricity.

As geothermal energy can be used as heat and electricity, it can be used for several mining operations. Some of the activities requiring thermal energy and could be supplied from geothermal heat are evaporation of highly concentrated solutions, enhanced heap leaching in lithium extraction, preheating iron ore concentrate slurry, seawater desalination, and space and fresh air heating with ground source heat pumps.

In contrast, in some of the underground deep mines, geothermal energy can be problematic too. Excess thermal energy is exacerbated by auto compression of air, explosives, and other machinery. In addition to ventilation, deep mines also require refrigeration to cool down the temperature and bring it to human comfort level. Hence, geothermal extraction technology is required for such mine operations too.

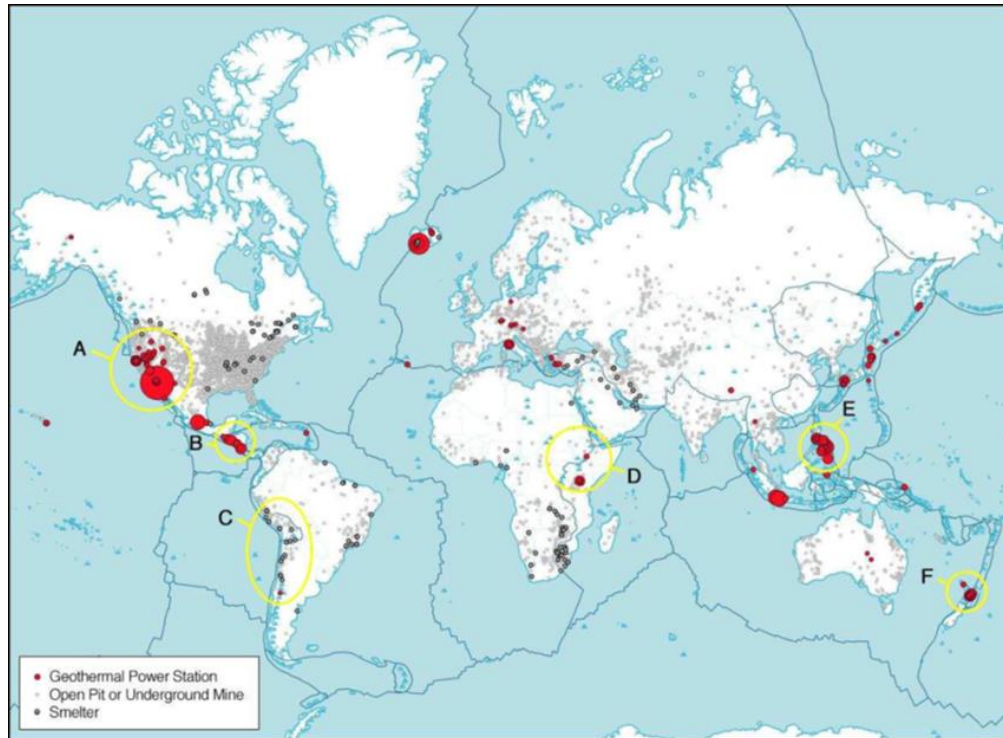


**Figure 2-2 Mining and geothermal map on a global scale [8].**

### **2.3 Closed-loop geothermal systems**

Some information about closed-loop geothermal is mentioned in the previous chapter. As this is the overarching theme of this work, to provide additional context and maintain a cohesive narrative, we will further explore the intricacies of this particular geothermal system.

Closed-loop geothermal systems have successfully addressed the limitations associated with conventional geothermal systems. Figure 2-3 and Figure 2-4 represent other types of closed-loop geothermal systems for district heat and power, respectively. Unlike traditional open-loop systems, which extract fluid from the subsurface to produce thermal energy, closed-loop systems use sealed Borehole Heat Exchangers (BHEs) to absorb and transport heat. This method eliminates the need for extraction and instead relies on the transfer of thermal energy between the fluid in the heat

exchanger and the subsurface. The benefits of closed-loop geothermal are numerous. Not only is it a greener and more sustainable option, but it also has a smaller surface footprint and can be installed in areas where open-loop systems are not feasible. It is estimated that only 2 percent of the geothermal resources reside in permeable regions where the use of an open-loop geothermal system is feasible [22]. Hence, with closed-loop technology, deeper locations around the globe can be explored for their geothermal potential.

Furthermore, closed-loop systems have the potential to be installed in thousands of decommissioned oil and gas fields, sharing a co-benefit with fossil fuel operations. For example, the Z-44 Chayvo well drills to more than 12 km to extract oil and gas. This depth is more than 15 times the tallest skyscraper - Burj Khalifa. The leakage of methane ( $\text{CH}_4$ ) from decommissioned oil and gas exploration and production wells is of environmental concern as well [23].  $\text{CH}_4$  and its leakage can have adverse consequences given its global warming potential of 24 over a 100-year timescale [24]. Capturing geothermal energy from such depths and temperatures could extract historically impossible renewable electricity and help to address the methane leakage problem. In addition to its environmental advantages, closed-loop systems consume little to no process water and operate with a lower risk of contamination to ground or surface water. Another significant point to include is that the well can be drilled in any direction and can evolve into multiple branches from specific depths. An example of such a system is presented in Figure 2-4. These systems have a higher surface area, which enhances energy production.

In closed-loop geothermal systems, different types of Borehole Heat Exchangers (BHEs) can be employed. This thesis focuses on a specific type of heat exchanger that can be used in closed-loop geothermal systems. The following section provides a literature review of the major heat exchanger types used in closed-loop geothermal systems.

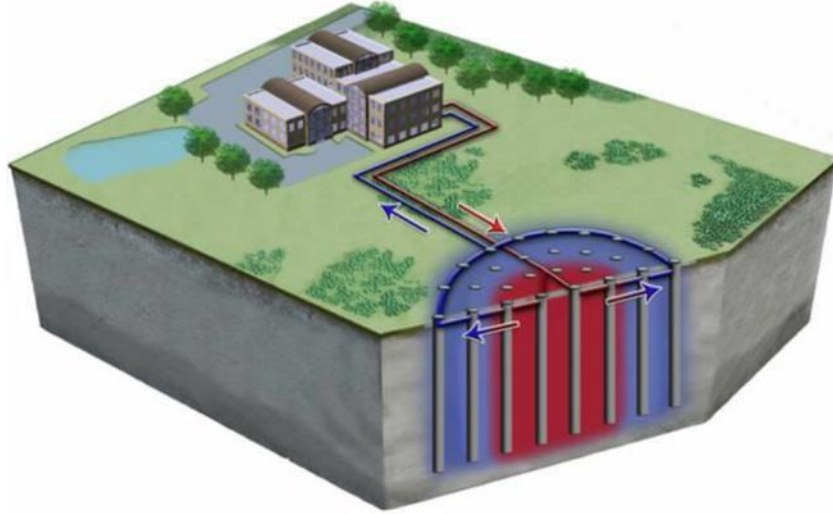


Figure 2-3 Closed-loop geothermal for district heating [12].

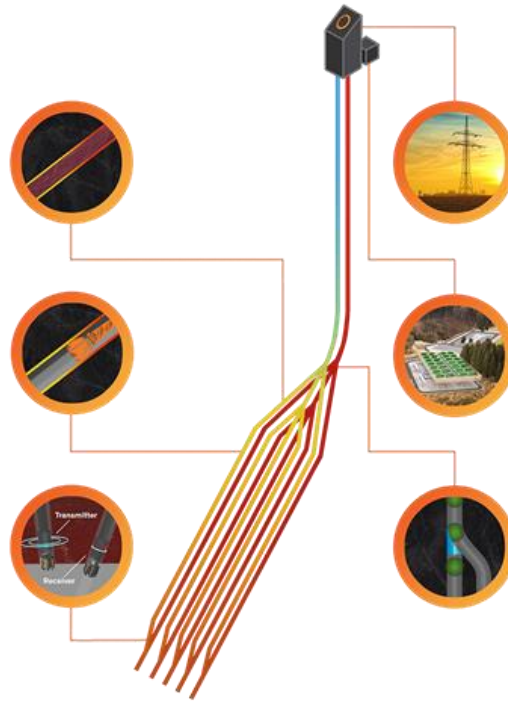


Figure 2-4 Closed-loop geothermal for power generation [25].

## 2.4 Closed-loop heat exchangers

The use of closed-loop BHEs for geothermal energy extraction has been studied extensively for the past 30 years from shallow to deep ground and aquifers. U-tube and coaxial are the most widely used BHEs according to the literature. A schematic diagram of these two types of heat exchangers is shown in Figure 2-5. The main difference between these BHEs lies in the design and configuration. U-tube BHEs have two separate pipes forming a U-shaped loop, while coaxial borehole heat exchangers have an inner pipe within an outer pipe.

A substantial volume of research is performed comparing the performances of these two BHEs. An experimental investigation to compare U-tube and coaxial BHE determined that the coaxial system needs less pumping power, is less turbulent for the same flow rate, incurs less drilling cost, and requires easier installation [26]. Numerical analysis to study the thermal behavior of BHEs revealed that for balanced thermal load and intermittent operating modes, the coaxial configuration provides better thermal performance due to the higher thermal capacitance [27]. A thermal response test demonstrated that the local borehole resistance for the coaxial heat exchanger is significantly lower than for U-pipes [28]. A performance comparison demonstrated that the coaxial collector has the most consistent thermal and hydraulic performance over the tested range of power and flow conditions [29]. A comparison between coaxial, single U-tube, and double U-tube BHE concluded that the most beneficial is the coaxial type [30]. Numerical analysis to compare BHEs found that with 500 m of well depth, 117.21 °C of temperature is reached with U-tube while with coaxial 131.25 °C is reached [31]. The reason was attributed to the heat loss in the returning pipe of the U-pipe. An overwhelming majority of past research suggests coaxial BHE performs better than U-tube BHE and hence is gaining more attention.

Two pipes are arranged concentrically in a Coaxial BHE (CBHE) as shown in Figure 2-5(left), the outer pipe is made of conducting material, while the inner pipe is made of insulating material. Cold fluid flows down from the annulus region and the outer conducting pipe exchanges thermal energy with the surrounding rock/soil to increase the fluid temperature. This hot fluid is carried back to the surface with minimum possible heat loss to its surroundings from the inner insulated pipe.

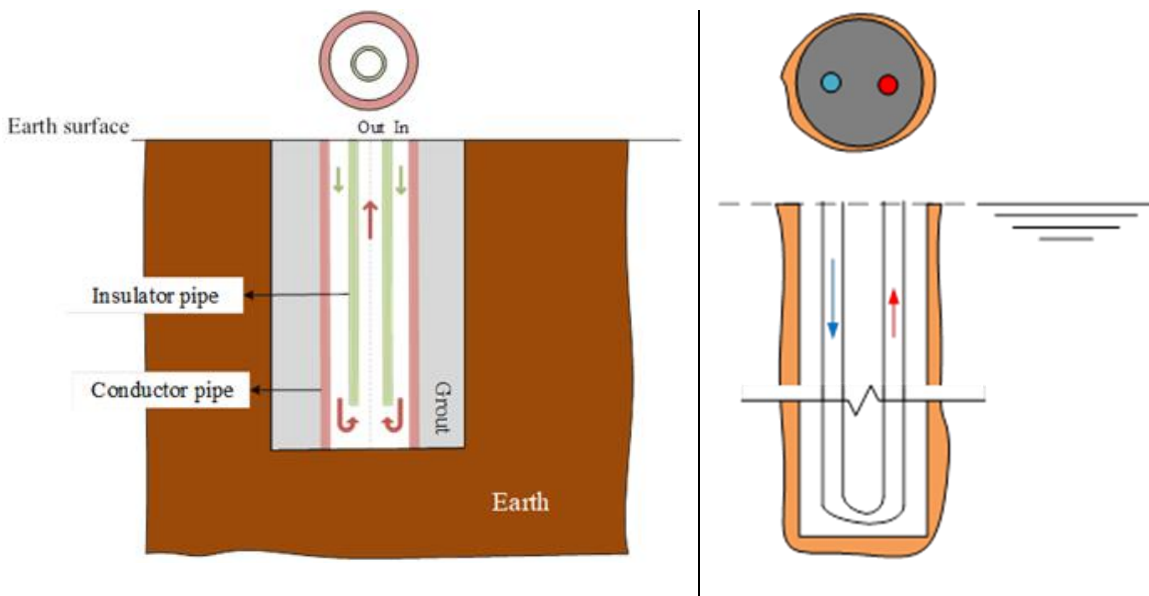


**Figure 2-5 Schematics of coaxial BHE (left) and U-tube BHE (right).**

Early literature on CBHE was presented by Horne in 1980 for space heating application barely based on conductive heat transfer in the soil assuming a quasi-steady state flow consideration [32], while the proof of concept for electrical power generation was first illustrated in 1985 [19]. Earliest experimental work to prove the concept of the CBHE for power generation application was carried out successfully in 1991 in Hawaii from a depth of 876.5 m drills with a maximum output of 540

$\text{kW}_{\text{TH}}$  [33]. More recent work on CBHE is carried out in Iran [34], Mexico[31], Ecuador [35], Italy[36], Turkey [37], United States [38], China [39], and South Africa [40]. A thermodynamic exergy and energy analysis of CBHE coupled to an Organic Rankine Cycle showed the first and second law efficiency of 10.62 % and 23.15 % [36]. A thermo-economic analysis of CBHE for geothermal power generation from a 2500 m deep existing geothermal well predicted a payback period of 2.5 years [37]. Literature suggests that there is a possibility that the CBHE can be operated without pumping for a long duration because of the gravity head arising in CBHE [38]. A wide variety of research is performed focusing on design characteristics and operational parameters of the system. Design characteristics include optimum diameter ratio of internal and external pipe for minimum pressure drop [40], insulation pipe material and its role in systems performance [36], [41], [42], and rock fracturing and using high conductivity material to fill the fractures [43]. Accordingly, operational parameters include flow rate variation [44], inlet fluid temperature effects [45], and heat transfer fluid chosen such as  $\text{CO}_2$  or water [46]. Both conduction and convection heat transfer mechanisms take place in closed-loop geothermal systems. Heat transfer in the borehole is caused by forced convection, but heat transfer in the rock is caused by conduction or a combination of conduction and convection, depending on the amount of seepage in the soil. Recently, many experimental, analytical, and numerical studies have been performed to study the heat transfer characteristics of CBHE.

#### **2.4.1 Experimental studies**

Several experimental works have been done on CBHE systems for heat and power. Most experimental investigations on CBHEs predominantly revolve around their usage in laboratory-scale setups or shallow ground-source heat pump (GSHP) systems, which are less than 100 m deep

[47], [48], [49]. Laboratory-scale setups, while controlled, often fail to replicate the true soil conditions found in the field. A few CBHE field-tests in the existing literature are worthy of mention here. The proof of concept of utilizing CBHE for power generation was first performed in 1991 in Hawaii from a depth of 856.5 m drill [50]. Wang et al. conducted a field-test investigation of CBHE in China and measured the outlet temperature from the heat exchanger for approximately five consecutive days [51]. The CBHE was employed in a building heating application, and their results indicated an average Coefficient of Performance (COP) for the heat pump unit of 6.4. They also measured the outlet temperature of the fluid from the heat exchanger but did not measure the subsurface temperature distribution of the ground. Another field-test experiment on the existing well was performed by Dai et al. in China, where they measured the outlet temperature from the system for 12 days. The heat output from the system was about 275 kW after two weeks of continuous extraction. [52]. Another notable field-test experiment on CBHE was performed by Huang et al. [53] on a 2044 m long CBHE in 2019. They recorded the outlet temperature for 60 days and also used the distributed fiber temperature sensors to measure the formation temperature at different depths. Therefore, from 1991 to 2019, there has been progress in terms of monitoring the outlet temperature for longer periods and measuring the subsurface temperature distribution at different stages of the extraction process. This progress has greatly contributed to understanding reservoir behavior and improving knowledge in the field. However, it is noticed that many of the previous studies have overlooked the recovery pattern of the well, which is of great importance in the understanding and design of geothermal systems. The recovery pattern refers to how the reservoir recovers its heat after the extraction process is halted.

### **2.4.2 Analytical studies**

Various analytical methods used in modeling the CBHE system are the composite cylindrical heat source method [54], finite line source method [55], [56] convolution theorem method [57], Fourier equation of heat transport method [58], and infinite line source method [59]. The common shortcoming of these analytical models is that they are often based on the assumptions of linearity, and steady-state conditions. They also assume a simplified conduction heat transfer in the ground as thermal resistance, rather than taking a conjugate approach in which transient convection in the well is directly coupled with transient conduction or convection in the ground. Besides, several of these approaches assume a constant temperature along the wall of the heat exchanger. This means the heat flux along the depth of the borehole is constant which is not the true representation of the physics. This can be overcome through the use of numerical methods.

### **2.4.3 Numerical studies**

The numerical modeling approach of CBHE can be divided into two broad categories: single borehole and multiple boreholes. The complexity of numerical modeling increases significantly when moving from a single borehole to multiple boreholes due to an increase in domain size, variations in fluid flow, and thermal interactions among the boreholes in the system. Hence a high-fidelity numerical model is developed to analyze a single borehole while reduced order models are common in analyzing a system of boreholes that demand less computational resource. This thesis also presents the development of two different numerical methods: one for modeling a single borehole and another for modeling a system of boreholes. The following section discusses the existing literature on numerical methods used for both a single borehole and a borehole system.

### 2.4.3.1 Single borehole numerical modeling

Numerical methods used for a single borehole CBHE analysis consist of finite difference [33], [60], [61], finite element [62], [63], [64], and finite volume methods [51], [65], [66], [67]. Several of them consider an axisymmetric approach [68][69] and 2D formulations [61], [66], [70], [71], [72] while some of them consider a full 3D numerical analysis [37], [51], [59]. Theo et al.[73] developed a Computational Fluid Dynamics (CFD) numerical model of CBHE of 2100 m depth for power generation application. They assumed an axisymmetric approach reducing from a 3D to a 2D model. Henrik et al. [71] performed the numerical evaluation of CBHE at 165 m of depth. They performed a 2D numerical approach to model the heat transfer process around the borehole while the borehole and the fluid in the heat exchanger are simulated as one-dimensional features. Although several numerical works in CBHE based on a single-dimensional or two-dimensional analysis can be cited, an analysis to compare three different approaches: fully analytical, semi-numerical, and fully numerical is performed by Hewei et al. [74]. They concluded that a full three-dimensional numerical model better predicts the performance of the system especially for the early transient time. They also found that the cylindrical-surface source model and the empirical correlation overestimated the outlet temperature by a maximum of 5 K. Hence, the three-dimensional behavior of fluid flow, heat transfer, and turbulence should be solved to accurately predict the heat transfer phenomenon in such systems, which 2D simulations and analytical solutions cannot predict accurately.

A few three-dimensional approaches are made for the modeling of CBHE and are worthy to mention here. A 3D heat transfer numerical simulation of geothermal power production work is done by Younes et al., [65] for a bottom hole temperature of 159.8°C and 4423 m depth from an abandoned petroleum well. They evaluated the effects of geothermal gradient and mass flow rate

on fluid outlet temperature considering the pure conductive heat transfer in the rock formation. Zhihua et al. [51] performed a fully three-dimensional numerical analysis of 2000 m deep CBHE but assumed a soil constant temperature and neglected the thermal conductivity of the conductor pipe. Chao et al. [75] performed a full-scale three-dimensional numerical model of a CBHE but the study was limited to a shallow depth of 50 m due to the computational cost. In addition, the numerical model accounted for only conduction heat transfer in the soil. Wang et al. [51] performed a numerical investigation with different rock properties at different depths. However, in their model, they neglected the thermal conductivity of the outer conductor pipe and the grout. They also assumed that the soil temperature remain constant throughout the depth. Some studies have explored the presence of different types of rock layers at varying depths [76], [77].

None of the three-dimensional models discussed above include the influence of groundwater movement, which could have a substantial impact on heat transfer characteristics. There have been several analytical and experimental studies on the effect of seepage on borehole heat exchanger performance [78], [79], [80], [81], but very few numerical studies have accounted for this effect [82], [83], [84], [85]. These include the 2D approach [82], the pseudo 3D approach [83], and the full 3D approach [84][85][86].

Tolooiyan et al. [82] investigated the impact of seepage velocity on heat exchanger performance and found that even a minor seepage velocity of 0.16m/day significantly enhances the efficiency of the heat exchanger. Brunetti et al. [83] developed a pseudo-3D model to study the influence of groundwater flow on the heat exchanger in an aquifer layer, using a reduced-order model instead of a conjugate approach. Li et al. [84] created a numerical model for shallow ground-source heat pump systems, considering saturated/unsaturated soil effects on heat exchanger performance.

Wang et al. [85] developed a numerical model to analyze the effect of ground water movement on heat exchangers for ground source heat pump systems, concluding that seepage enhances heat transfer and system performance. Chen et al. [86] explored borehole heat exchanger performance with groundwater seepage in surrounding rock, finding that horizontal seepage and proper borehole spacing improve performance. However, all these models are shallow geothermal systems and assumed arbitrary seepage velocity values rather than measuring in-situ seepage characteristics in the soil, presenting challenges in examining the effect of seepage in permeable layers below the ground surface. While some research has been conducted on porous media seepage characteristics, most of these projects have artificially created porous media in controlled laboratory environments. They utilize setups such as packed beds of spheres [87], uniform sand or gravel particles [88], [89] or artificial fractures to study Enhanced Geothermal Systems (EGS) [90], [91]. In these engineered systems, identifying porous parameters is relatively straightforward compared to the challenges posed by naturally occurring porous soil or rock, where such heat exchangers are deployed for geothermal power extraction.

#### **2.4.3.2 Multiple boreholes numerical modeling**

Numerical modeling on multiple boreholes is more challenging than a single borehole due to the large domain size, the requirement of exceedingly large mesh count, and thus the computational resources. To provide a context, a 100 m deep borehole requires more than a million fine meshes to perform an accurate simulation and could take from several hours to many days for a single run relative to the machine's capacity. Large-scale district heating systems – where these multiple boreholes are installed - typically involve more than 100 boreholes, resulting in a tremendous demand for computational resources. In a district heating system of this kind, the inlet temperature

of the boreholes and the flow rate change in accordance with the thermal demand. Even modeling a small range of 2 to 20 boreholes with dynamic inlet temperature and heat transfer fluid (HTF) flow rate poses a challenge for achieving a converged solution with the use of existing commercial numerical solvers [92], [93].

To overcome these issues of computational demand and convergence, simulating such large systems with reduced-order models (ROMs) is a commonly adopted approach [94], [95][96]. ROMs are simplified mathematical representations of complex mathematical processes that can reduce computational resource requirements while maintaining the essential dynamics and behavior of the system. Substantial effort has been made in developing ROM to evaluate a system of boreholes [93], [97]. Reduced-order techniques are used to solve the energy equation in recent literature [98], [99], considerably improving computational performance. These ROMs incorporate heat transfer interactions between boreholes within a cluster, as well as different design configurations, and operational strategies [100], [101], [102]. Zueter et al. [103], developed a reduced-order algorithm that only needs 1% as much computational time as the established models. In this context, Pokhrel et al. [68] proposed a semi-conjugate model that reduces the computational cost of a multiple boreholes numerical model by 430 times.

A collection of multiple boreholes in a district heating application is also referred to as a Borehole Thermal Energy Storage (BTES) system. These systems of boreholes are used to store thermal energy and supply it to meet user demand, hence the name is known as a Borehole Thermal Energy Storage System (BTES). The system of boreholes in this thesis is also referred to as BTES.

These published ROMs focus primarily on the BTES system but often overlook the system-level analysis approach or fail to integrate other system components such as building demand and thermal losses. There are some commercially available software including TRANSYS, Energy

Plus, and GLEHEPRO that can simulate building load and BTES systems relying on g-functions to compute the dimensionless temperature. These g-functions assume a constant heat load and offer a semi-analytical expression of the temperature produced by a finite/infinite line source or finite cylindrical source subjected to a constant heat flux per unit length of the borehole [104]. More work should be done to develop a comprehensive numerical model of the BTES system and conduct a system-level analysis to gain a deeper understanding of its behavior.

## **2.5 Contributions to the existing literature**

This dissertation consists of three distinct works associated with the next three chapters of this thesis.

Firstly, a field-test experiment is performed in a 500 m deep CBHE for geothermal energy extraction. The experimental analysis that is performed as a part of this thesis is the advanced form compared to all of the above-mentioned field-test analyses in the past. The current study is performed under a high-temperature resourced well with a thermal gradient of  $0.4\text{ }^{\circ}\text{C}/\text{m}$  compared to a low geothermal gradient in published literature. The experiment is done for 30 days of extraction followed by a recovery period of 23 days. This is the first type of geothermal resource exploration in the literature that contains the recovery temperature profile of the subsurface with the use of a Distributed Temperature Sensing (DTS) system. Hence, this work generates a new set of extraction-recovery data with the state-of-the-art experimental methodology which is unavailable in the existing literature. This set of data could be used as a reference for future experimental work.

Secondly, the numerical modeling of the field test CBHE was undertaken. This model of a 500 m deep CBHE addresses the shortcomings identified in previous numerical studies related to the

modeling of CBHE. It presents a three-dimensional numerical model of a 500 m CBHE to solve the conjugate fluid flow and heat transfer process with accurate geometrical details, in-situ geological properties, and in-situ subsurface temperature distribution. The 3D numerical model is designed to solve fluid flow and heat transfer processes in the heat exchanger and the geothermal reservoir characterized by porous volcanic rocks and seepage fluid velocity that changes with depth. A significant contribution of this research lies in the ability of the model to include the effect of seepage in a geothermal reservoir in combination with collected experimental data.

The final chapter of this thesis concerns the development of a reduced-order numerical model to solve fluid flow and heat transfer processes in a system of  $N \times N$  boreholes or BTES used in the solar-geothermal system. In the proposed numerical model, one-dimensional fluid flow and heat transfer in the boreholes is accompanied by a three-dimensional conduction process in the surrounding rock strata. It overcomes the shortcomings of previous models by simulating the  $N \times N$  array of boreholes numerically, incorporating the dynamic behavior of solar thermal collectors and building thermal demand, and different energy losses in the solar-geothermal system. These advancements in the literature present an elegant and comprehensive solution to advance the understanding and design of solar-geothermal systems.

## Chapter 3: Experimental Analysis of a Field-Scale Coaxial Heat Exchanger for Geothermal Power

### Preface

This chapter presents the results obtained from the field-test experiment conducted on a 500 m deep geothermal system utilizing a Coaxial Borehole Heat Exchanger (CBHE). Part of this chapter and the following chapter have been published in the *Journal of Renewable Energy*. Additionally, an article is currently in preparation, highlighting the most recent and updated outcomes of the research.

- **Pokhrel, S.**, Sasmito, A. P., Sainoki, A., Tosha, T., Tanaka, T., Nagai, C., & Ghoreishi-Madiseh, S. A. (2022). Field-scale experimental and numerical analysis of a downhole coaxial heat exchanger for geothermal energy production. *Renewable Energy*, 182, 521-535.
- **Pokhrel, S.**, Sasmito, A. P., Sainoki, A., Tosha, T., Tanaka, T., Nagai, C., Samea, P., & Ghoreishi-Madiseh, S. A. (2023). Geothermal energy extraction from natural porous rocks: study on field testing, experimental analysis, and numerical simulation with the presence of seepage. (under preparation).

### **3.1 Introduction**

The experimental analysis of a 500 m deep coaxial borehole heat exchanger is presented and analyzed in this study. The experiments are carried out on a high-temperature resourced well with an average thermal gradient of 0.4 °C/m. The experiment involves 30 days of extraction, followed by 23 days of recovery. During extraction, fluid is injected into the heat exchanger, and thermal energy is extracted from the reservoir while during recovery, no heat extraction is made and the well is left to recover. Experimental findings are expressed and analyzed in terms of flowrate in the heat exchanger, inlet and outlet temperatures of the flow, and subsurface temperature distribution profiles over time. This in-situ ground temperature distribution profile is measured using a Distributed Temperature Sensing system. Additionally, the characteristics of rocks sampled from the nearby site are analyzed. Laboratory tests are conducted on two distinct rock formation types obtained from different depths within the geothermal reservoir. By combining the extraction and recovery temperature profiles of the reservoir with the properties of the rock formations, an avenue for interesting discussions is opened. This chapter delves into the comprehensive analysis of how the geothermal reservoir responds to extraction and recovery and how the rock formations influence the process.

### **3.2 Methodology**

The field test was performed near Beppu, Oita, Japan, at an elevation of 500 meters from sea level and 1 kilometer west of the Alum hot spring. The first stage of the experiment was the drilling, which was carried out using a drilling rig as displayed in Figure 3-1. The total depth of the drill is 500 m which was accomplished in steps, as shown in Figure 3-2. Firstly, drilling was done for an initial 50 m in length, followed by a steel pipe set. The diameter of the initial excavation is 444.5

mm, while the outer and inner diameters of the steel pipe set are 355.6 mm and 339.8 mm, respectively. After this step, drilling was extended to 200 m of depth which was again followed by a steel pipe set in the peripheral boundary. The diameter of this drill is 311.3 mm while the internal and external diameters of the steel pipe setting for this depth are 244.5 mm and 224.4 mm, respectively. The last step excavates to 500 m deep which is followed by the steel pipe setting to complete the drilling process. The detailed dimensions of the heat exchanger are also presented in Figure 3-3. After this step, the innermost insulator pipe was installed. This central tube has internal and external diameters of 114.3 mm and 103.88 mm, respectively. The steel pipe has a relatively high thermal conductivity since it is meant to exchange heat with the surrounding rock mass. Grout fills the space between the steel pipe and the drill hole wall. Grout is also the outer layer of the CBHE. After drilling, the various pieces of equipment necessary for the experiment were installed. Figure 3-4 depicts the schematics of the experimental setup. Similarly, Figure 3-5 and Figure 3-6 represent the set-up of the temperature control unit during the experiment and the picture taken during the experiment, respectively. Different components of the experiment include CBHE, a flowrate regulating valve, a water pump, a water tank, a steam separator, a Distributed Temperature Sensor (DTS), and a temperature sensor at the borehole outlet.



Figure 3-1 Drilling equipment installation set-up for the experiment.

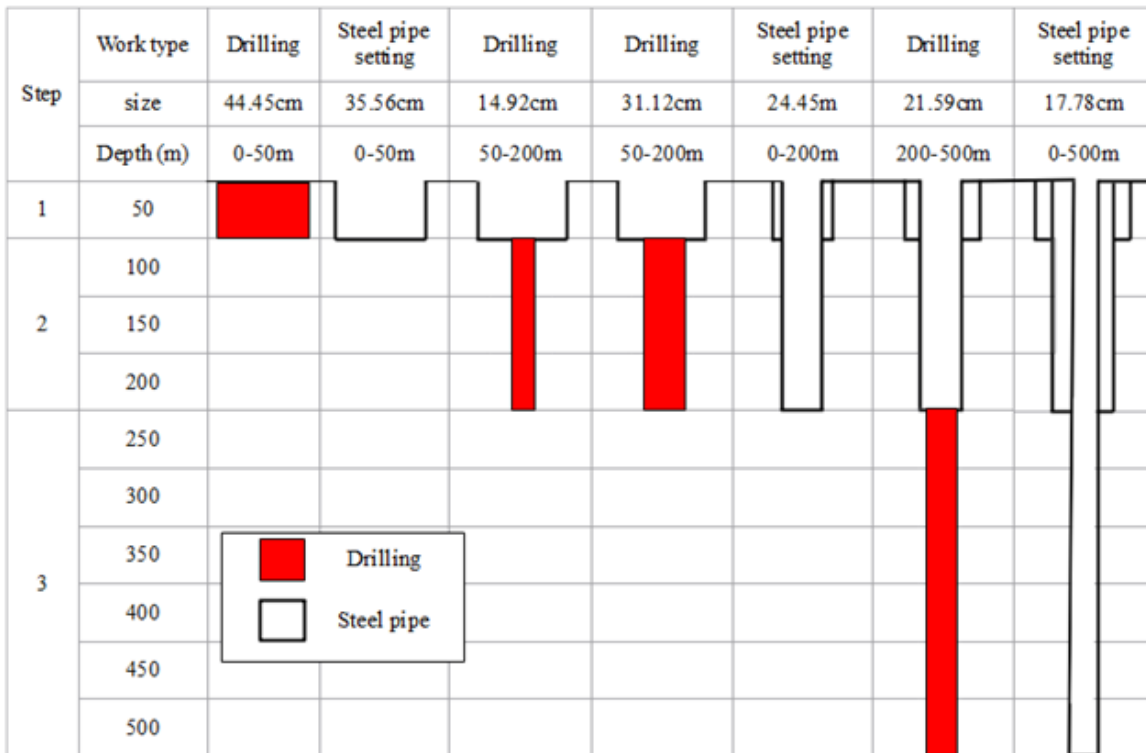
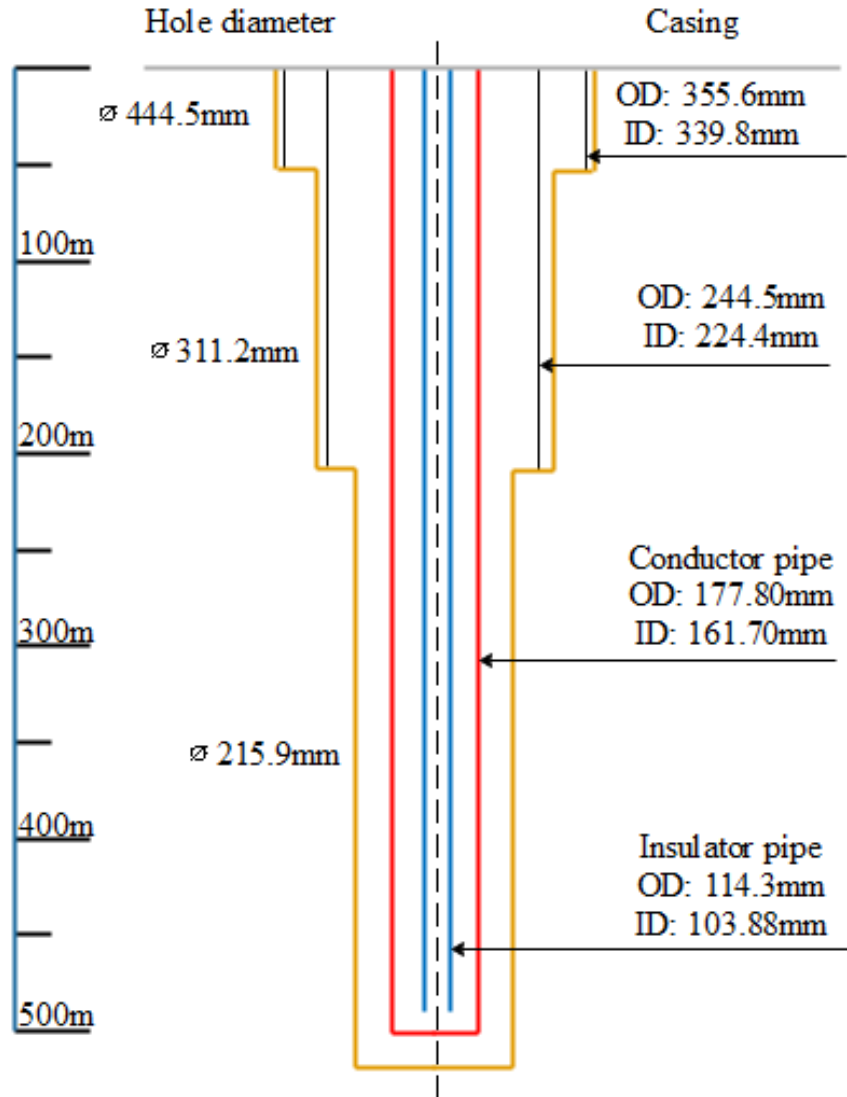


Figure 3-2 Drilling procedure during the experiment.



**Figure 3-3 Detailed dimension of the borehole (OD and ID are the outer and inner diameters of the steel pipe; and  $\varnothing$  is the outer diameter of the drill hole).**

The next step is the experiment or water circulation test. The constant flow rate of water at a given temperature is pumped into the CBHE during the water circulation test. The water flow interacts with the heat flux supplied at the boundary of the conductor pipe, causing it to heat up. The innermost pipe of the heat exchanger is made of a material with very low thermal conductivity, transporting hot water to the surface with insignificant thermal energy loss. The temperature of the

outlet water is determined by a sensor mounted at the outlet. Hot water from the CBHE, having a higher temperature, evaporates upon contact with the lower atmospheric pressure compared to the pressure inside the CBHE caused by the hydrostatic force. As a result, a steam separator is used to isolate the steam generated by the system. The separated fluid is sent to the water tank, where it is mixed with cold water to achieve the desired temperature. A pump is used to draw water from the tank to the flowrate controller, which also tests the overall mass flow rate into the system. The DTS is installed through the depth of the borehole which measures the temperature distribution of the ground using optical fiber functioning as a linear sensor. This is an important device for understanding the depth and temperature change over time after the circulation starts.

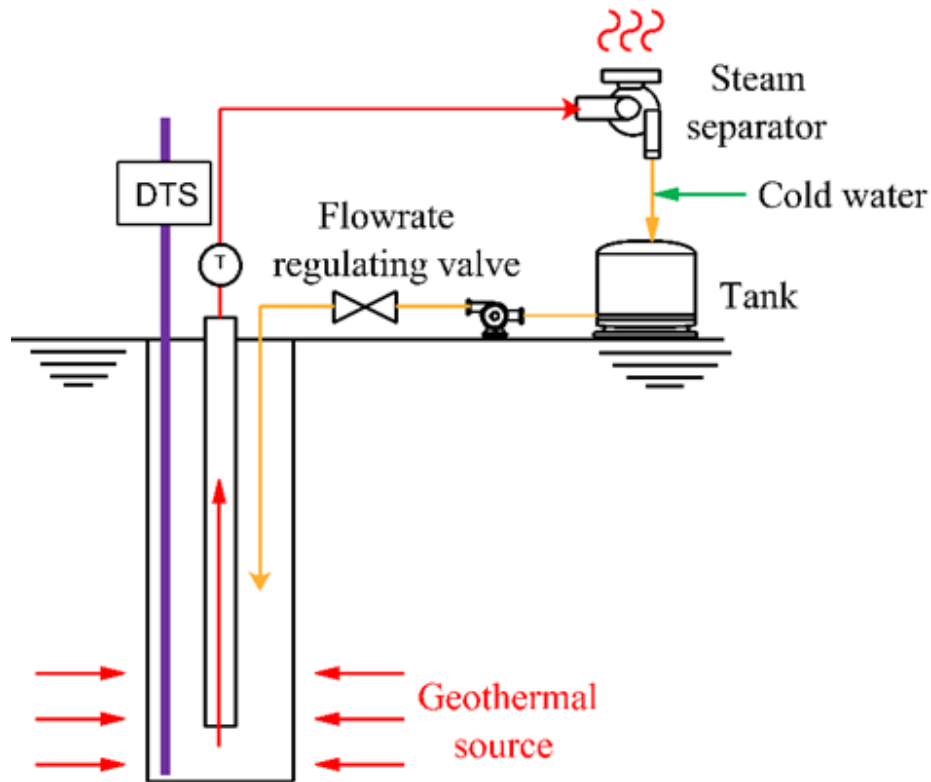


Figure 3-4 Schematics of the experiment.



**Figure 3-5 Temperature control unit.**



**Figure 3-6 Experiment setup during the water circulation test.**

The experiment consists of two distinct stages: extraction and recovery. During extraction, water is continuously injected at a flow rate of 100 l/min (liters per minute) for the first 30 days. Throughout the circulation period, the inlet temperature of the water is kept constant at 70°C, and the outlet temperature is monitored. Subsurface temperature measurements are taken at various times during the circulation. The temperature distribution profile is measured by utilizing DTS, which can measure the temperature of the strata at every level of the heat exchanger wall. During the extraction phase, temperature measurements are taken along the borehole after the 1<sup>st</sup> day, 5<sup>th</sup> day, 15<sup>th</sup> day, and 30<sup>th</sup> day. The recovery stage begins once the circulation is stopped. Recovery is measured in terms of the temperature distribution profile along the heat exchanger. Temperature measurements are taken for a total of 23 days, with measurements taken on the 1<sup>st</sup> day, 5<sup>th</sup> day, 15<sup>th</sup> day, and 23<sup>rd</sup> day.

### **3.3 Experimental results**

The undisturbed ground temperature, (also known as the static formation temperature or well equilibrium temperature), is the first experimental result. It is of utmost importance as it determines the geothermal potential. The well equilibrium temperature was determined based on the Horner plot method [105]. The temperature recorded at a point in time during logging operations does not represent the true static temperature, as the mass surrounding the drill hole is disturbed by drilling and circulation during the drilling process [106]. Instead, a better approach is to use a series of logs to estimate static formation temperature. Dowdle and Cobb [107] validated the Horner plot method proposed by Timko and Fertl [108] to measure the static temperature of the well, and it continues to be widely used. We also used this approach to determine the well equilibrium

temperature based on a series of recorded recovery temperatures. The formula used to calculate the equilibrium bottom-hole temperature is given by:

$$T_{ws} = T_i - C \log \left( \frac{t_k + \Delta t}{\Delta t} \right) \quad (3.1)$$

where,  $t_k$  is the circulation time in hours,  $\Delta t$  is the time after circulation ceases,  $T_i$  is the static formation temperature and  $T_{ws}$  is the bottom-hole shut-in temperature, and C is a constant. Circulation time is the time taken for the drilling process plus the water circulation test, which is 771 hours, whereas shut-in times are the times at which the recovery temperatures are recorded. For each meter of depth at which the well temperature is recorded, a semi-log plot of  $T_{ws}$  vs.  $\left( \frac{t_k + \Delta t}{\Delta t} \right)$  is plotted, and the plot is extrapolated to a time ratio of unity to yield  $T_i$ . Figure 3-7 represents the plot obtained for a depth of 350 m, for which the well equilibrium temperature is obtained as 177.1°C. Using a similar approach, well equilibrium temperatures were obtained for all depths. The well equilibrium temperatures for different depths are presented in Figure 3-8.

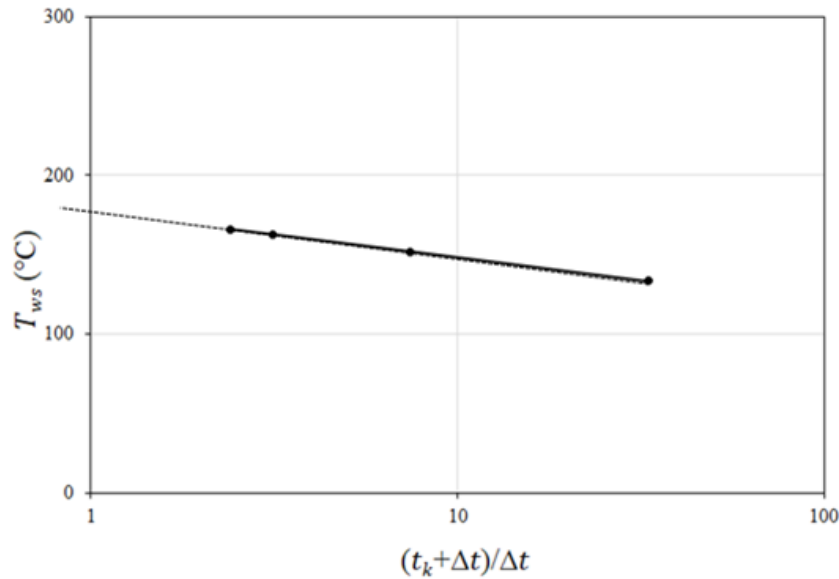


**Figure 3-7 Estimation of well equilibrium temperature from Horner plot method for a depth of 350 m.**

The undisturbed ground temperature ranged from 20°C near the surface to 204°C at the bottom of the well (500 m), corresponding to 0.37°C/m or 370°C/km. This is a good geothermal gradient and could be suitable for power generation applications. Generally, geothermal gradients for different locations are found between 0.03°C/m-0.10°C/m based on available literature [65], [109][33], [61], [70]. The saturation temperature represents the temperature at which water would start boiling at the hydrostatic pressure corresponding to the depth. The figure indicates that water would exist in a liquid state within the reservoir at all depths from 0-500 m. This is due to the saturation temperature curve consistently exceeding the measured undisturbed ground temperature at all depths.

For this location, some of the literature assumes the presence of two-phase zones in the vicinity of the current well, about 500 m of elevation above sea level, at shallow depths [110], [111]. Some

existing literature mentions that the two-phase zone may start at a lower elevation than the current well location, possibly below 300 m above sea level [112]. No other literature discussing the phases at this elevation range was found. Based on the findings and the equilibrium temperature profile of the well, it is reasonable to assume that the fluid within the rock layers primarily exists in a liquid form rather than as steam. Continuous thermal energy extraction for hot water bathing purposes from more than 2,000 wells in the region might have resulted in the gradual transition from a steam-dominated zone to a water-dominated zone over time. It is worth noting that shallower depths are also affected by the vertical infiltration of surface waters, and at times, weather conditions can impact the presence of water or two-phase fluids.

From the current experiment, it is also observed that the thermal gradient along the depth of the well is not uniform. Typically, as depth increases, so does the geothermal temperature. However, this does not hold for depths ranging between 140 m and 185 m. Higher subsurface temperatures are observed at this range compared to depths ranging between 185 m and 400 m.

Figure 3-9 represents the water circulation test results in terms of water outlet temperature. A maximum outlet temperature of 169.5°C was obtained approximately an hour after the experiment began. The corresponding thermal output power from the system is calculated at 691 kW. After reaching the peak temperature, the outlet temperature decreased significantly, eventually dropping below 100°C after 240 hours of testing. At the end of extraction, the temperature was at 98.0°C and the corresponding thermal output power from the system was calculated at 195 kW.

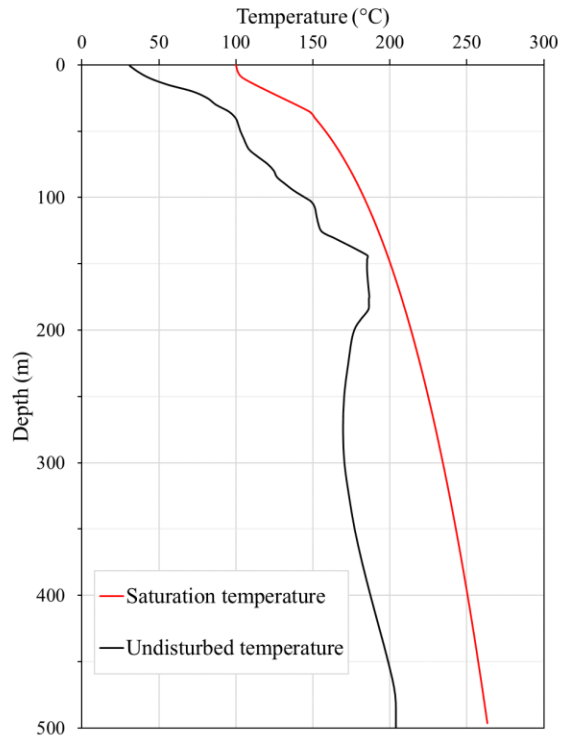


**Figure 3-8 Undisturbed ground temperature and corresponding saturation temperature.**

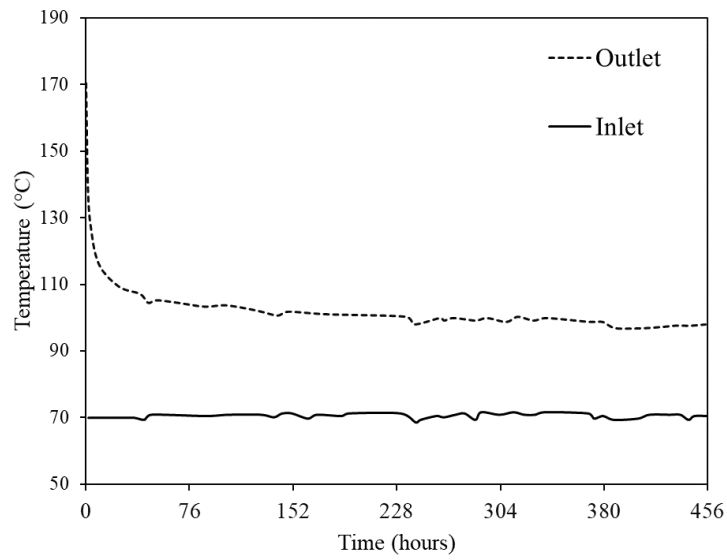


**Figure 3-9 Outlet temperature results during water circulation test.**

As stated earlier, experimental results also consist of the subsurface temperature distribution profiles during extraction and recovery. The subsurface temperature profile refers to the temperature along the steel pipe of the CBHE. Temperature profiles during extraction and recovery are presented in Figures 3-10 and 3-11, respectively. During the extraction process, the bottom well temperature decreased to 123.3 °C, 113.7 °C, 109.6 °C, and 107.2 °C at the end of days 1, 5, 15, and 30, respectively. Similarly, during the recovery process, the bottom well temperature recovered to 156.4 °C, 176.8 °C, 188.0 °C, and 191.9 °C at the end of days 1, 5, 15, and 23, respectively.

Further analysis of the subsurface temperature profile during extraction and recovery, specifically between the last day of extraction and the first day of recovery, revealed a significant difference in recovery pattern in the regions ranging between 135 m and 185 m as shown in Figure 3-12. The temperature recovery pattern between the shallow region (0 m-135 m) and the deeper region (185 m-500 m) of the reservoir differed significantly as well. The temperature in the shallow region (0 m-185 m) exhibited a faster recovery rate compared to the deeper region (185 m-500 m). This faster recovery is due to the presence of a layer with higher thermal conductivity or the presence of advection due to seepage. Further insight is gained through the analysis of the rock properties within the reservoir which is elaborated in detail in the subsequent section.

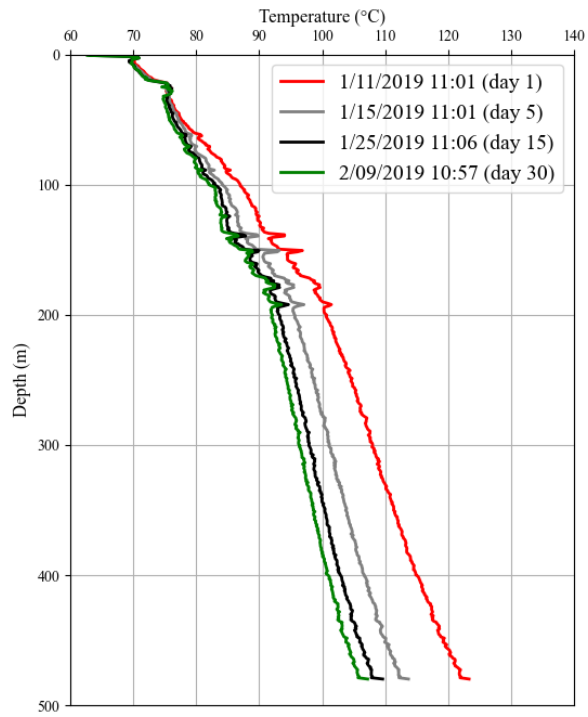


**Figure 3-10 Experimental temporal evolution of ground temperature during extraction.**

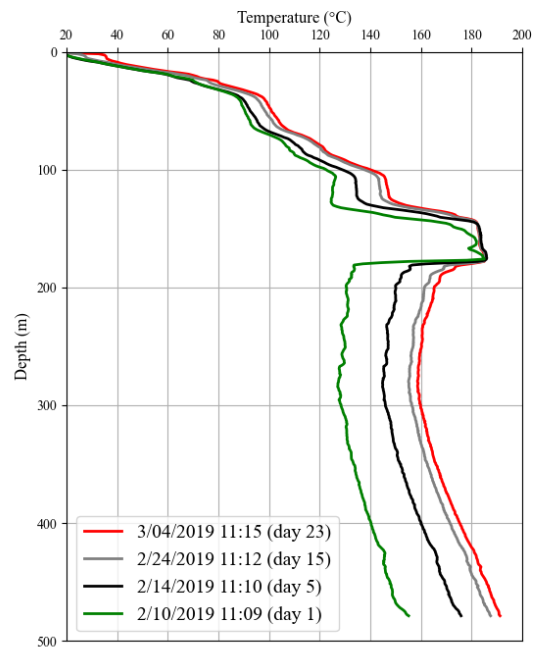


**Figure 3-11 Experimental temporal evolution of ground temperature during recovery.**

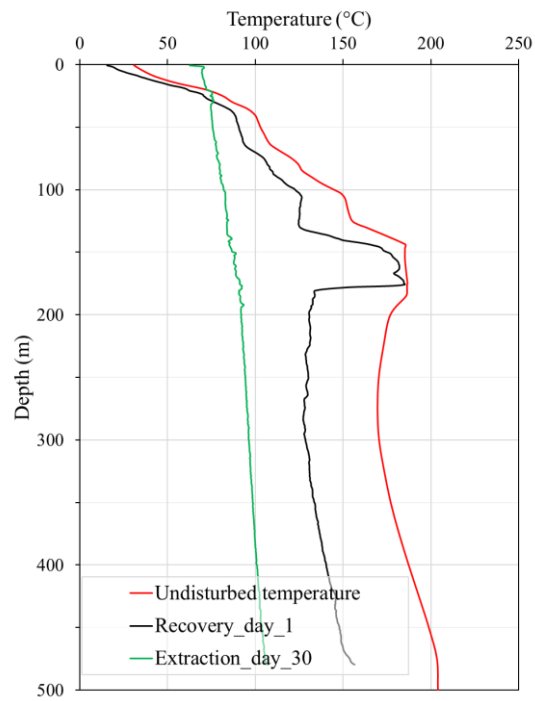


**Figure 3-12 Comparing initial temperature with the last day of extraction and the first and last day of recovery.**

### **3.4 Rock properties analysis**

Due to the unavailability of the rock samples from the experiment site, proxy rock samples from a nearby location were collected and analyzed. This was decided following communication with Professor Atsushi Sainoki, who has been involved in research on silicified rocks in that region for a long time. The rock samples were collected from a nearby gold mine with a similar composition, as indicated in the literature, and verified by Dr. Sainoki and other research team members. There is historical evidence that gold was mined from this location between 1903 and 1916 [111]. It was concluded that the strata consisted of silicified andesite below the first 15 meters of soil. The composition of the rock is also validated by a number of other past publications [110], [113]. The formation of these silica rocks is attributed to the cooling and solidification of magma or lava rich in silica, which is common in active volcanic regions near the drill site. The rock characteristics were noted at different depths. Figure 3-13 shows the rock samples obtained from elevations ranging from 15 m-185 m and 185 m-500 m.

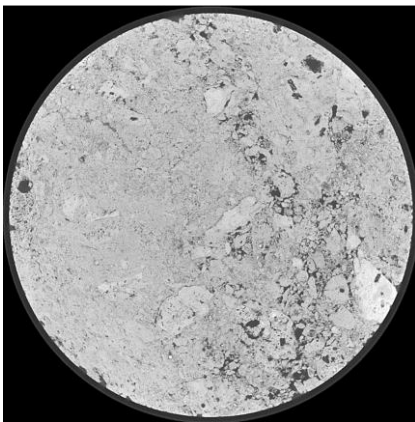
Figure 3-13(a) and Figure 3-13(c) represent rocks found in the shallower region, at depths ranging from 15-185 meters. In this thesis, these rock types are referred to as “vuggy silica”, characterized by their high silica content and numerous cavities known as "vugs". Vugs are irregular pores formed due to the dissolution of soluble minerals other than silica by acidic geothermal fluid, resulting in leached silicified rocks. Such deposits can serve as important reservoirs of groundwater. In contrast, Figure 3-13(b) and Figure 3-13(d) represent rock from deeper depths, characterized by its uniform texture and without major visible pores/cavities— hereinafter referred to as massive silica in this thesis.



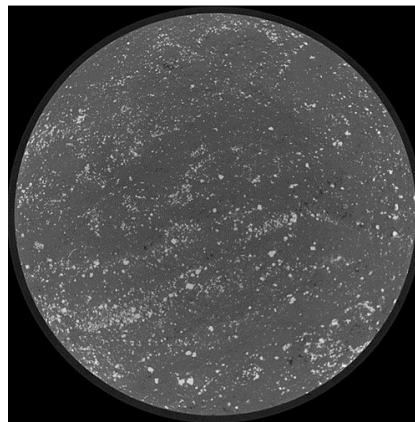
(a)



(b)



(c)



(d)

**Figure 3-13 Rock samples tested: (a and c) vuggy silica; and (b and d) massive silica (Courtesy: Professor Sainoki from Kumamoto University).**

The next step was to measure the physical, thermal, and hydraulic properties. Laboratory tests were performed to measure the hydraulic conductivity, porosity, thermal conductivity, specific heat, and density. Hydraulic conductivity and porosity tests were conducted in Professor Sainoki's research lab at Kumamoto University. Water permeability test was conducted using the flow pump

method. Figure 3-13 shows the specimen for the permeability test. The diameter and height of samples are 49.5 mm and 28.0 mm, respectively. The results of permeability and porosity tests are presented in Table 3-1.

**Table 3-1 Properties of rocks measured in the lab.**

<b>Rock type</b>	<b>Porosity (%)</b>	<b>Hydraulic conductivity (m/s)</b>
Vuggy silica	25.04	$3.57 \times 10^{-8}$
Massive silica	2.78	$9.74 \times 10^{-9}$

Laser Flash Apparatus (LFA) 427 was used to measure the temperature-dependent thermal diffusivity and specific heat capacity of vuggy silica using Laser-Flash method. In this method, thermal properties are determined based on the thermal response of a sample after exposing it to a short burst of radiant energy. With the measured thermal diffusivity and specific heat capacity, thermal conductivity was calibrated using Equation (3.2).

$$k(T) = a(T) \cdot C_p(T) \cdot \rho \quad (3.2)$$

Where,  $k$  is thermal conductivity [units W/(mK)],  $a$  is thermal diffusivity [units  $m^2/s$ ],  $C_p$  is specific heat [units J/(kg K)] and  $\rho$  is the bulk density [units  $kg/m^3$ ] that is assumed to be independent of temperature. The thermal and physical properties of the massive silica were calculated by assuming that the pores were filled with the same material that constitutes the vuggy silica rock type. Equation (3.3), Equation (3.4), and Equation (3.5) were used to calculate thermal conductivity, density, and specific heat of massive silica [114]. Here, subscripts  $m$ ,  $s$ , and  $f$  represent the porous medium (vuggy silica), solid medium, and fluid medium, respectively.

Symbols  $k$ ,  $\varphi$ ,  $\rho$ , and  $c$  are thermal conductivity, porosity, density, and specific heat capacity, respectively.

$$k_m = (1 - \varphi) k_s + \varphi k_f \quad (3.3)$$

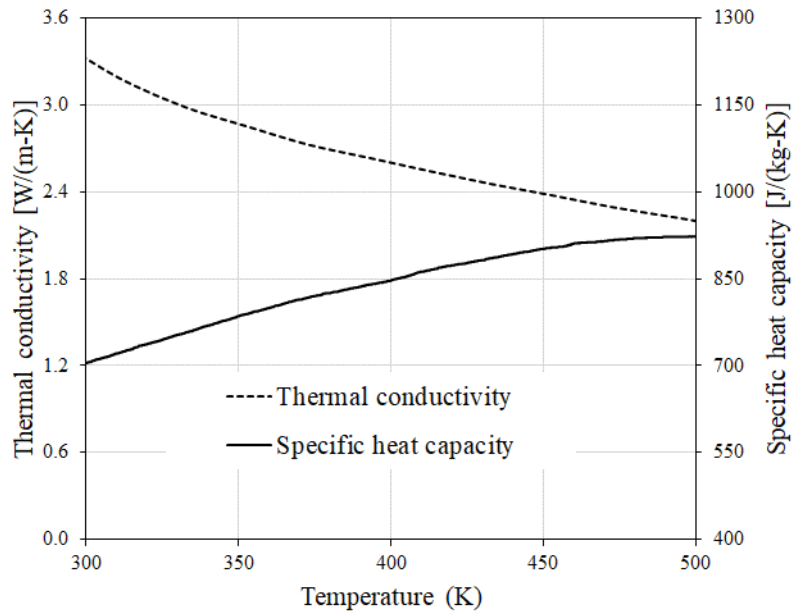
$$\rho_m = (1 - \varphi) \rho_s + \varphi \rho_f \quad (3.4)$$

$$(\rho c)_m = (1 - \varphi) (\rho c)_s + \varphi (\rho c_p)_f \quad (3.5)$$

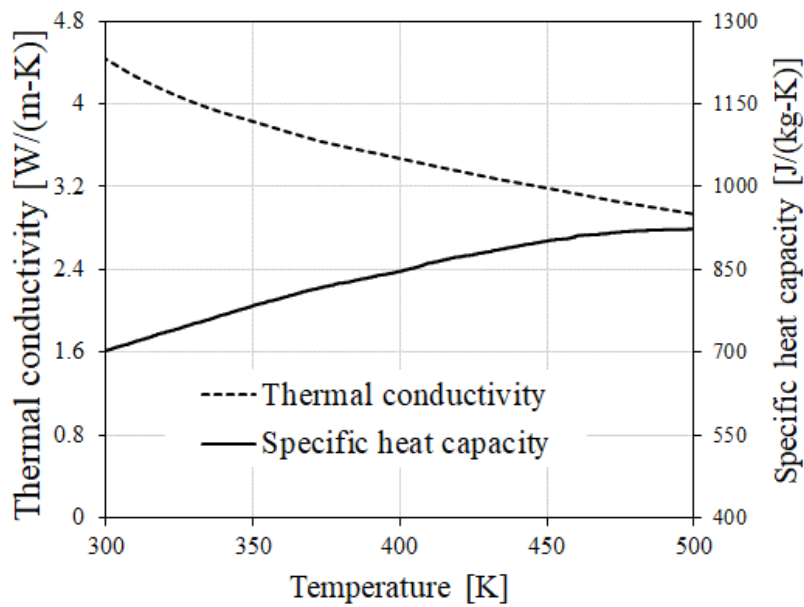
Density of vuggy silica and massive silica were obtained as 2245 kg/m<sup>3</sup> and 2911 kg/m<sup>3</sup>, respectively. For vuggy silica, the specific heat capacity ranged from 704 to 923 J/(kg K), while the thermal conductivity ranged from 3.2 to 2.2 W/(mK) within the temperature range of 300 K to 500 K. Similarly, for massive silica, thermal conductivity ranged from 4.2 to 2.8 W/(mK) within the temperature range of 300 K to 500 K. Figure 3-14 presents the results of thermal conductivity and specific heat capacity of these rock types.

The analysis of the rock properties, particularly at shallower depths, reveals a porosity of 25% and a hydraulic conductivity value of  $3.57 \times 10^{-8}$  m/s. This indicates the presence of fluid in the pores of the shallow rocks, whereas no such presence is observed in the deeper regions. While it is evident that the shallower region contains fluid, it remains challenging to determine whether the seepage fluid is air or water and whether it is at rest or in motion. Moreover, predicting the seepage velocity at various depths proves to be equally subtle. To gain further insights into this intriguing phenomenon, a comprehensive numerical model is developed in the subsequent chapter of this thesis. This model aims to shed light on the dynamic behavior of the seepage fluid and provide a

clear understanding of its movement and velocity variations in the rock formations. Through this model, we endeavor to resolve the complexities of fluid behavior at different depths.



(a)



(b)

Figure 3-14 Thermal conductivity and specific heat capacity of vuggy silica (a) and massive silica (b).

### **3.5 Conclusions**

This chapter presents the insightful results derived from the field-test analysis of a 500 m deep coaxial borehole heat exchanger. The focus of the analysis centers on the outlet temperature and the subsurface temperature distribution of the reservoir during both the extraction and recovery processes. Additionally, extensive laboratory investigations were conducted to further study the properties of the reservoir. The experiments revealed a notable peak outlet temperature of approximately 170°C, occurring about an hour after the initiation of the experiment, followed by a stable temperature of slightly below 100°C during the subsequent days. Rock samples acquired from different elevations showed distinct characteristics. The shallower zone exhibited vuggy silica with identifiable pores, suggesting an advective dominant area. In contrast, the deeper regions displayed massive silica with minimal porosity (and lower permeability), indicative of a conductive dominant region. Building on these significant findings, the next chapter delves into the development of a numerical model to gain deeper insights into the behavior of the reservoir and further augment our understanding of this complex geological system.

## **Chapter 4: Numerical Simulation of a Field-Scale Coaxial Heat Exchanger for Geothermal Power**

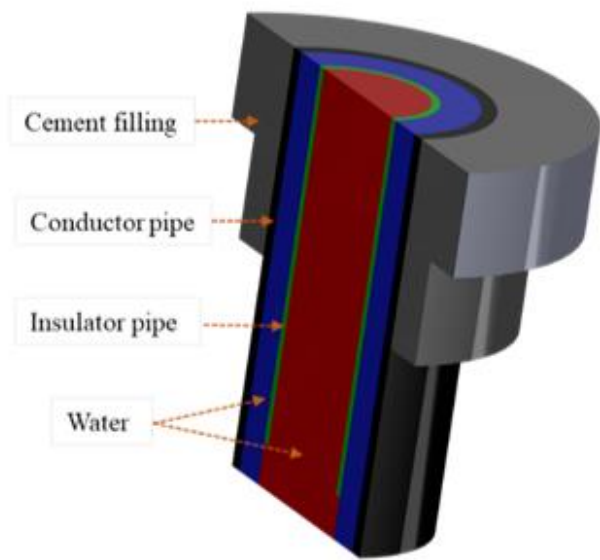
### **4.1 Introduction**

This chapter presents the development and results of the numerical model for the field-scale experimental test discussed in chapter 3. To complement the experimental findings, a 3-dimensional numerical model is developed that couples the heat and mass transfer processes in the heat exchanger as well as the reservoir. The developed numerical model in combination with experimental findings is used to analyze the physical behavior of the geothermal system. The model is validated against the experimental data, in terms of the outlet temperature and temperature distribution profiles during both extraction and recovery periods. A significant finding from the developed numerical model is the calibrated seepage velocity in the porous rock formation, which matches the subsurface extraction and recovery temperatures observed during the experiment. Furthermore, the validated numerical model is utilized to analyze the long-term performance of the geothermal system over 30 years, considering various design and operating conditions. An analysis is conducted to assess the impact of seepage on the system over the lifetime of the project. Results reveal that the thermal output from the system increases by 19.5% due to the calibrated seepage, compared to a pure conductive model with no seepage in the formation. Furthermore, the total energy output from the coaxial borehole heat exchanger system ranges between 113.3 TJ to 141.5 TJ based on varying design and operating conditions.

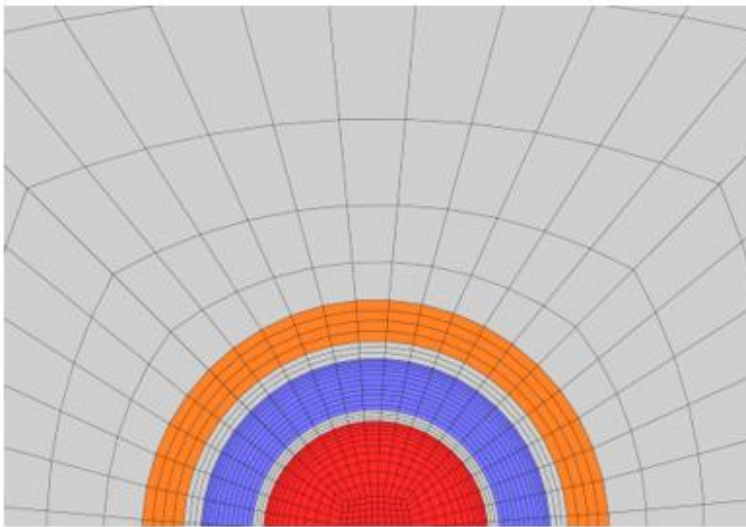
## **4.2 Methodology**

### **4.2.1 Geometry and meshing**

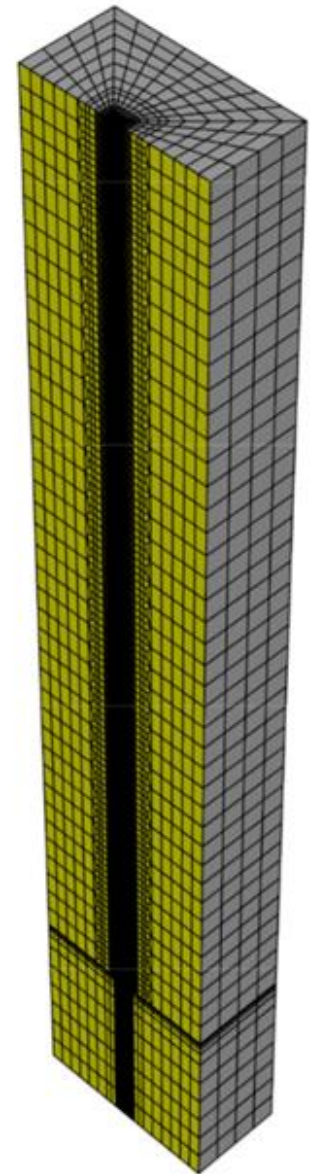
To perform the numerical analysis, a full-scale three-dimensional control volume in a Cartesian coordinate system is developed. The top rectangular section of the geometry is  $100\text{ m} \times 100\text{ m}$  and the considered domain depth is  $600\text{ m}$ . Due to the symmetry of the problem, half of the geometry is considered, resulting in a symmetric plane about the vertical  $y$ -axis. The system constitutes four solid domains and a fluid domain. Ground, conductor pipe, insulator pipe, and cement filling are the four solid regions, while the fluid region is inside the annulus and the inner pipe as shown in Figure 4-1(a). The blue color of the fluid region represents the water in the inlet tube of the heat exchanger, whereas the red color represents the water in its outlet tube. Hexahedral meshes are generated throughout the domain as depicted in Figure 4-1(b) and Figure 4-1(c). Figure 4-1(b) is the magnified mesh on the surface of the heat exchanger. Here, the red color represents the outlet, the blue color represents the inlet, and the orange color represents the cement fillings. The mesh element is intentionally made finer near the center of the domain. This mesh is generated in ICEM CFD and is transferred to ANSYS Fluent for simulation.



(a)



(b)



(c)

**Figure 4-1 Numerical model construction: (a) Different domains considered in the analysis (geometry not to scale); (b) Meshing scheme at the inlet and outlet of the CBHE; and (c) Generated hexahedral mesh of the whole domain.**

#### 4.2.2 Initial and boundary conditions

Initial conditions in the simulation are based on the in-situ initial temperature of the subsurface as determined by a temperature sensor during the experiment. To enforce the initial temperature distribution profile in the numerical model, a User-Defined Function (UDF) is generated and compiled. A UDF allows users to customize the software by writing code in the C programming language, providing additional functionalities beyond the standard features. Likewise, variable rock properties are attributed to varying depths, and distinct seepage velocities are assigned to different depths.

The analysis assigns a mass flow inlet boundary condition with a constant mass flow rate and a pressure outlet boundary condition at the fluid exit. Walls between cement filling and ground, conductor pipe and cement filling, conductor pipe, and the annulus region, and insulator pipe with the annulus and inner pipe are modeled as coupled walls. In Fluent, this is a thermal condition to couple two-sided walls where the wall zone has a fluid or solid region on each side. A far boundary independence study was conducted to determine a suitable distance of the walls from the heat exchanger axis. The findings showed that for the duration of the circulation test, there was no influence on the wall temperature at 50 m from the central axis. Hence, a Dirichlet boundary condition is used on the side walls and the bottom wall. This Dirichlet boundary condition defines the value of temperature directly at the far wall of the domain. The far boundary wall temperature is a function of depth and is identical to the measured ground temperature profile with the DTS as discussed in section 3.3, and implemented via a UDF. The initial condition that assigns the initial temperature distribution of the subsurface is represented by Equation (4.1) while the far-field wall temperature is constant and is represented by Equation (4.2) and is kept unchanged over time. Both

of these equations are a function of depth. The initial temperature profile and the wall temperature profile are shown in Figure 3-7 in the previous chapter.

$$T_{(x,y,z,t=0)} = T_{init}(x, y, z) \quad (4.1)$$

$$T_{(walls,t)} = T_{(x,y,z)} \quad (4.2)$$

Similarly, a Neumann boundary condition is used at the top surface, through which a convective heat flux is introduced into the system that can be either positive or negative depending on the temperature difference between the ground surface and the ambient temperature. Convective heat transfer is represented by Equation (4.3), where  $T_a$ , and  $T_{wall}$  are the ambient and ground surface temperatures, respectively. Heat loss or gain via radiation is not considered in the analysis.

$$\dot{Q} = -k_g \left. \frac{\partial T_g}{\partial n} \right|_{topwall} = h(T_{wall} - T_a) \quad (4.3)$$

Table 4-1 presents the physical properties of the various materials used in the study, excluding rock. As explained in chapter 3, laboratory tests were conducted to measure the hydraulic, thermal, and physical properties of the rock samples acquired from a nearby location with similar characteristics. The properties of the conductor and insulator pipes align with the user specifications provided by the manufacturer.

**Table 4-1 Material properties used in the simulation.**

<b>Material name</b>	<b>Density (kg/m<sup>3</sup>)</b>	<b>Specific heat (J/kgK)</b>	<b>Thermal Conductivity (W/mK)</b>	
1	Water	998.2	4182	0.6
2	Insulated inner pipe	5240	310	0.35
3	Conductor pipe	7850	470	46.1
4	Cement	1830	1900	1.0

As mentioned in chapter 3, two different rock layers were identified in the reservoir: a shallower region and a deeper region located below 185 m. As discussed in chapter 3, deeper regions constitute rocks with lower permeabilities that justify the use of a purely conductive model. Whereas, due to the presence of seepage at shallower depths, a conductive-convective heat transfer process is more justifiable.

#### **4.2.2.1 Porous media boundary conditions**

The porosity and hydraulic conductivity of the rock were measured through laboratory measurements. Porosity is an input parameter used in the numerical model for the porous domain. However, the hydraulic conductivity could not be directly used to calculate the velocity field due to the lack of experimental data on pressure. Instead, the adopted approach was calibrating the velocity field to match the experimental temperature distribution profiles during both extraction and recovery. It was also assumed that the seepage velocity field is horizontal and is a function of depth. Consequently, the boundary condition for the porous media was defined by the porosity

value and a fixed seepage velocity that changes with depth. Hence the seepage velocity boundary condition at the boundary wall can be represented as:

$$U = U_{specified}(z, t) \quad (4.4)$$

### 4.2.3 Governing equations

The conservation of mass (in the absence of source term) and momentum for the flow of an incompressible fluid is given by Equation (4.5) and (4.6), respectively. To simulate heat transfer, solving the energy equation is an important part of the process. There are different types of heat transfer mechanisms based on material composition. In impermeable, non-porous rocks, conductor pipe, insulator pipe, and grout, only pure conduction occurs, as there are no fluids present. The conduction is described by Equation (4.7). In Equations (4.5) to (4.7), the velocity vector of the fluid phase is denoted by  $\vec{v}$ , while  $p$  represents the pressure of the fluid. The density of the fluid is represented by  $\rho$ , and  $\bar{\tau}$  denotes the stress tensor. The acceleration due to gravity is represented by  $\vec{g}$ . Temperature is denoted by  $T$ , and  $t$  represents time. Thermal conductivity is represented by  $k$ , while  $C_p$  represent the specific heat capacity.

$$\nabla \cdot \vec{v} = 0 \quad (4.5)$$

$$\rho \frac{\partial}{\partial t}(\vec{v}) + \rho \vec{v} \nabla \cdot \vec{v} = -\nabla p + \nabla \cdot \bar{\tau} + \rho \vec{g} \quad (4.6)$$

$$\rho C_p \frac{\partial}{\partial t} T = \nabla \cdot (k \nabla T) \quad (4.7)$$

Equation (4.8) is the fluid energy equation in the heat exchanger. The effective thermal conductivity,  $k_{eff}$ , is used in this equation, which is the sum of the fluid thermal conductivity and turbulent thermal conductivity. The turbulent thermal conductivity is defined using the second term on the right-hand side of Equation (4.9). In addition, the effective thermal conductivity depends on the dynamic viscosity,  $\mu_t$ , and turbulent Prandtl number,  $Pr_t$ .

$$\rho C_p \frac{\partial}{\partial t} T + \rho C_p \vec{v} \cdot \nabla T = \nabla \cdot (k_{eff} \nabla T + (\bar{\vec{v}}_{eff} \cdot \vec{v})) \quad (4.8)$$

$$k_{eff} = k_f + \frac{C_p \mu_t}{Pr_t} \quad (4.9)$$

Similarly,  $K-\epsilon$  turbulence model is applied in the heat exchanger fluid flow. This is a two-equation turbulence model which allows the determination of both, turbulent kinetic energy,  $KE$ , and its dissipation rate,  $\epsilon$ . Equations (4.10) and (4.11) are solved concurrently with the continuity and momentum equation to predict the behavior of the turbulent flow. Turbulence equations are linked to the momentum equations through the Reynolds stress tensor term in Equation (4.6)

$$\frac{\partial(\rho k)}{\partial t} + \nabla \cdot (\rho k \vec{v}) = \nabla \cdot (\mu_{eff} \nabla k) + P_{KE} - \epsilon \quad (4.10)$$

$$\frac{\partial(\rho \epsilon)}{\partial t} + \nabla \cdot (\rho \epsilon \vec{v}) = \nabla \cdot (\mu_{eff} \nabla \epsilon) + \frac{\epsilon}{k} (C_{\epsilon 1} P_{KE} - C_{\epsilon 2} \rho \epsilon) \quad (4.11)$$

Here,  $\mu_{eff}$  is the effective viscosity,  $P_{KE}$  is the turbulent production term, and  $\epsilon$  is the dissipation rate of turbulent kinetic energy. Equation (4.11) governs the evolution of the dissipation rate  $\epsilon$  of turbulent kinetic energy. In this equation  $C_{\epsilon 1}$  and  $C_{\epsilon 2}$  are empirical constants whose values are the default values in the solver.

Heat transfer in porous rocks involves both conductive heat transfer in the solid domain and advective heat transfer in the pores filled with fluids. In this simulation, both the fluid and solid phases are assumed to be in thermal equilibrium. The justification for this assumption is described in the following section. Energy equations for solid and fluid phases are given by Equations (4.12) and (4.13), respectively. In these equations, based on the assumption of local thermal equilibrium,  $T_s = T_f = T$ , where  $T_s$  and  $T_f$  are the temperatures of solid and fluid phases, respectively. The porosity of the material is denoted by  $\varphi$ . Subscripts  $s$  and  $f$  represent solid and fluid phases, respectively.

$$(1 - \varphi)(\rho C_p)_s \frac{\partial T_s}{\partial t} = (1 - \varphi)\nabla \cdot (k_s \nabla T_s) \quad (4.12)$$

$$\varphi(\rho C_p)_f \frac{\partial T_f}{\partial t} + (\rho C_p)_f v \cdot \nabla T_f = \varphi \nabla \cdot (k_f \nabla T_f) \quad (4.13)$$

#### 4.2.4 Assumptions of the numerical model

The fluid and the rock matrix in the reservoir are in local thermal equilibrium, implying that in the discretized control volume (pore scale), there is no temperature difference between the rock and the porous fluid at any point in time ( $T_s = T_f = T$ ). It should also be noted that there are no heat source terms in either of the two mediums in porous media to cause a substantial difference in temperature between the two mediums. The required conditions for this assumption are also extensively discussed in the literature. In naturally occurring geothermal volcanic rocks, the particle dimension  $d$  is of a much smaller order than the system dimension  $L$ , yielding  $L/d \gg 1$ , and the variation of temperature across  $d$  is negligible compared to that across  $L$  for both the solid

and fluid phases. Additionally, the considered geothermal system also satisfies the criteria mentioned by Kaviany [115]:  $K^{1/2} \ll d < l \ll L$ , where  $l$  represents the representative elementary length of a porous medium and  $K$  is the permeability of the medium. In terms of mathematical formulation, Carbonell and Whitaker [116] presented length-scale and time-scale conditions based on which the assumption of local thermal equilibrium can be made. According to them, the time scale must satisfy the conditions listed in Equations (4.14), (4.15), (4.16), and (4.17). In Equations (4.14), (4.15), (4.16), and (4.17),  $\varphi$  represents the porosity of the porous medium. Subscripts  $s$  and  $f$  represent the solid and fluid mediums, respectively.  $\rho$  is the density of the medium,  $C_p$  is the specific heat capacity,  $k$  is thermal conductivity,  $A_{fs}$  is the interfacial area density of the porous medium, and  $t'$  is the time scale of the system.

$$\frac{\varphi(\rho C_p)_f l^2}{t'} \left( \frac{1}{k_f} + \frac{1}{k_s} \right) \ll 1 \quad (4.14)$$

$$\frac{(1 - \varphi)(\rho C_p)_s l^2}{t'} \left( \frac{1}{k_f} + \frac{1}{k_s} \right) \ll 1 \quad (4.15)$$

Similarly, length scales must satisfy the following conditions:

$$\frac{\varphi k_f l^2}{A_{fs} L^2} \left( \frac{1}{k_f} + \frac{1}{k_s} \right) \ll 1 \quad (4.16)$$

$$\frac{(1 - \varphi) k_s l}{A_{fs} L^2} \left( \frac{1}{k_f} + \frac{1}{k_s} \right) \ll 1 \quad (4.17)$$

Similarly, Minkowycz et al. [117] concluded that a sufficiently high Sparrow number is necessary to ascertain the state of the local thermal equilibrium, where the Sparrow number is defined by

$$S_p = Nu_{r_h} \left( \frac{k_f}{k_{eff}} \right) \left( \frac{l}{r_h} \right)^2 \quad (4.18)$$

Where,  $r_h$  represents the hydraulic radius of the mean pore, calculated as the ratio of the surface area to the volume of the mean pore. Additionally, the value of  $Nu_{r_h}$  is a constant analogous to a Nusselt number and is approximately equal to 1. The current geothermal system model satisfies all the above-listed criteria, and hence, a thermal model based on local thermal equilibrium is adopted.

#### **4.2.5 Numerical scheme**

A pressure-based solver and the SIMPLE algorithm were chosen for pressure-velocity coupling in Fluent. A second-order upwind discretization scheme was applied in both space and time. Convergence criteria for each of the scalar species were set to  $10^{-6}$ , and for the temperature, it was set to  $10^{-9}$ . The fixed time-stepping method was used to obtain the desired results over the anticipated timeframe. The simulation was run on a LINUX-based High-Performance Computing system given the large mesh count and the requirement to run several simulations.

#### **Mesh sensitivity analysis**

To make results independent of the mesh size, the mesh independence test was conducted by varying the mesh size from coarse to fine. The pressure loss in the pipe and the outlet temperature from the coaxial borehole were measured as variables to access mesh independence. The mesh with element counts of 7.9 million was chosen out of three meshes as presented in Table 4-2. The difference in pressure loss with this mesh count is 0.31% of the pressure loss of the most refined mesh. Similarly, the change in outlet temperature from the coaxial borehole after 456 hours was

within 0.04% of the value corresponding to the most refined mesh (Mesh 3). These adjustments were deemed to be within an acceptable range. For the considered mesh, the smallest element size in the radial direction in the borehole is 0.0015 meters, grout is 0.0021 meters, conductor and insulator pipe is 0.0011 meters, and ground is 0.01 meters.

**Table 4-2 Grid independence test results.**

<b>Parameter</b>	<b>Mesh 1</b>	<b>Mesh 2</b>	<b>Mesh 3</b>
Total number of nodes	5,774,135	7,933,195	10,474,235
Total number of elements	4,631,456	6,720,888	9,569,485
Size of the smallest element (m)	0.0032	0.00079	0.00032
The pressure difference between the inlet and outlet (Pa)	8,512.73	8,666.29	8,693.11
The pressure difference between two consecutive meshes (Pa)	153.56	26.82	Reference
Pressure difference	1.77 %	0.31%	Reference
Outlet temperature (°C)	95.53	95.51	95.47
Temperature difference	0.06%	0.04%	Reference

### **4.3 Seepage calibration and validation process**

In accordance with the aforementioned geometry, mesh generation, utilization of thermophysical and hydraulic rock properties, and the implementation of initial and boundary conditions, the simulation was executed by the solver. Initially, the simulation was conducted under the assumption of negligible fluid movement in the rock formation. However, this assumption failed

to align with the outlet temperature results, as well as the profiles for extraction and recovery temperatures obtained within the reservoir. Subsequent to multiple iterations and rigorous tests, various adjustments were made to the seepage velocity across different layers of the reservoir. These adjustments aimed to achieve a correlation with the extraction and recovery temperature profiles within the reservoir. For reference, the outcomes of some tested cases, along with their corresponding results, have been detailed in Appendix B. Ultimately, through successive iterations, a seepage velocity assumption was determined that yielded the most accurate match with both the extraction-recovery profiles and the outlet temperature from the heat exchanger during the field-test experiment.

#### **4.4 Numerical results validation and error analysis**

Figure 4-2 illustrates a comparison of the outlet temperature results obtained through both experimental and numerical methods. The peak temperature reached 166.2°C during the numerical analysis, whereas it was 169.5°C during the experiment. With a base temperature of 70°C, this discrepancy amounts to 4.7% compared to the experimental data. Another notable error of 4.5% is observed approximately after 10 hours of extraction. This corresponds to 115.9°C compared to 119.0°C in the experimental results. However, the average error diminishes as time progresses.

In Figure 4-3, the experimental results of subsurface temperature distribution are presented with the numerical results for various days of extraction. During extraction, the highest discrepancy is observed at a depth of 100 m on the first day of extraction. For this depth and time, the experimental temperature obtained was 87.0°C, while the corresponding numerical value is 82.6°C, resulting in a maximum error of 5.1%. All other errors in temperature profiles during the extraction were less than this value. Likewise, Figure 4-4 presents a comparison between the experimental and

numerical results of subsurface temperature distribution during the recovery period spanning different days. It was observed that the maximum error of 6.9% occurred on the 5th day of the recovery. The experimental temperature obtained at a depth of 120 m on this day was 134.6°C, while the numerical temperature at the same time and depth was calculated as 143.9°C.

The calibrated seepage velocities corresponding to different depths are presented in tabular format in Table 4-3. Notably, the investigation revealed a maximum seepage velocity of  $5e-5$  m/s within the shallower region spanning 20-40 m, concurrently representing the peak velocity within the reservoir. Recalling the extraction period, a substantial temperature rise in the heat exchanger becomes evident at depths between 20-40 m. Across all extraction days, temperatures increase from 70°C to 76°C within the 40 m depth range. This substantial temperature rise finds its validation in the calibrated seepage velocity.

Furthermore, comparatively, a higher seepage velocity is also observed with the 140-185 m depth interval. This region not only experiences a comparatively higher temperature gain within the HTF during the extraction but also demonstrates a swift recovery process. Interestingly, even after the first day of recovery, nearly the entirety of the temperature drop encountered during extraction is reclaimed. The calibrated seepage velocity for this depth registers at  $7e-6$  m/s. Similarly, in the depth bracket of 40-140 m, a seepage velocity of  $1e-6$  m/s is calibrated. This velocity would best match the extraction and recovery profile, rendering it the optimal choice for this particular depth range.

Another significant point is that, within the depth range of 185-500 m, in accordance with the measured hydraulic properties of rock samples, this region is characterized by a purely conductive mechanism. This conductive process is also validated with the numerical results.

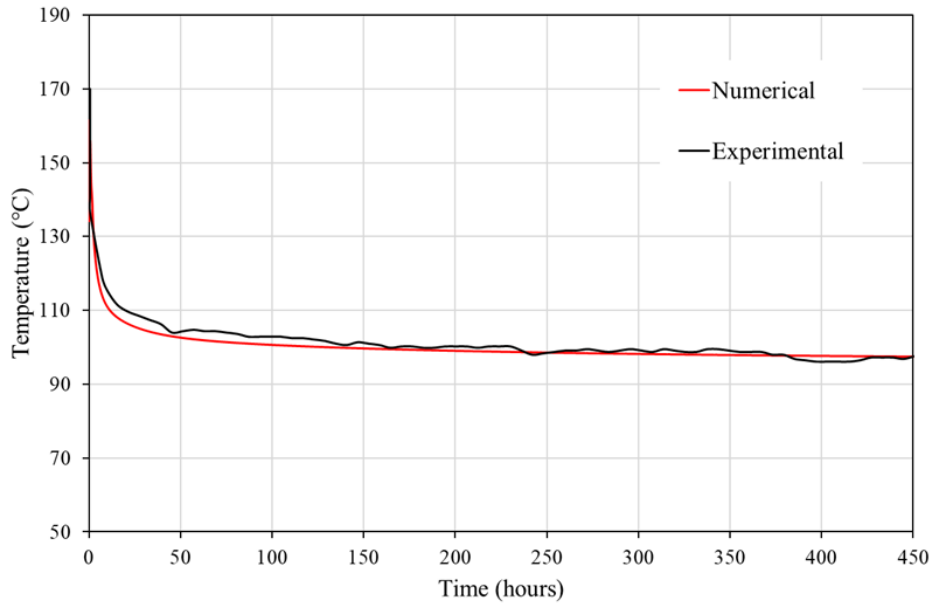
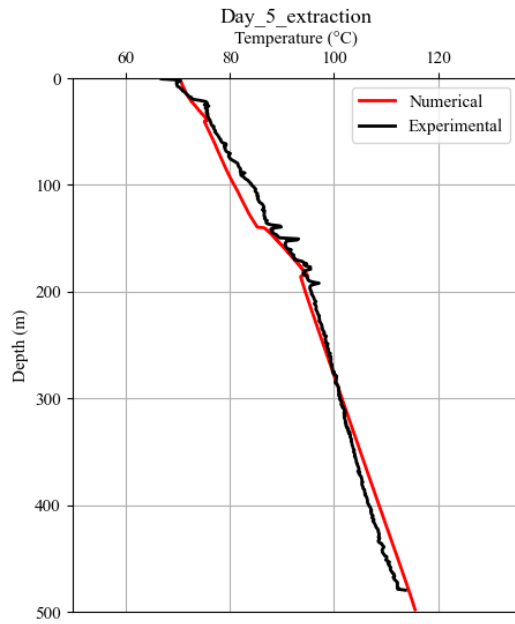
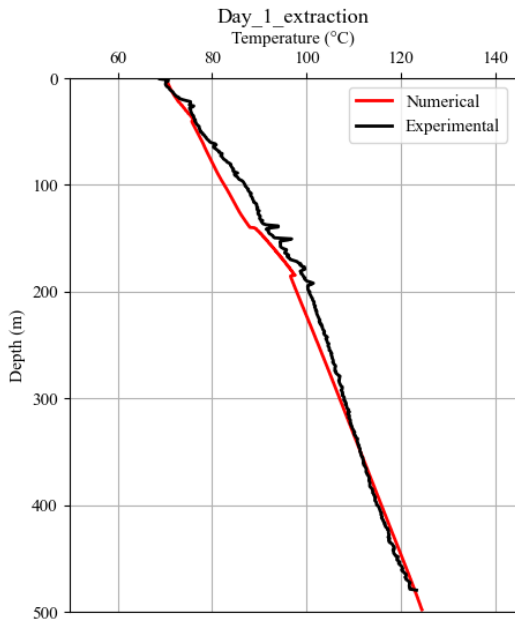


Figure 4-2 Comparing outlet temperatures: experimental vs numerical results.



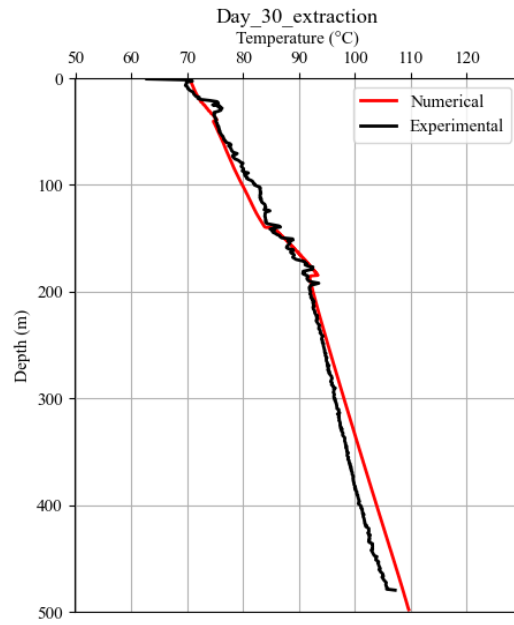
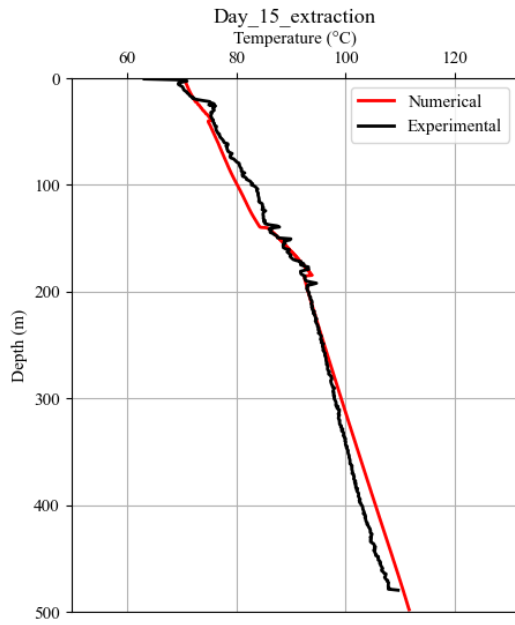
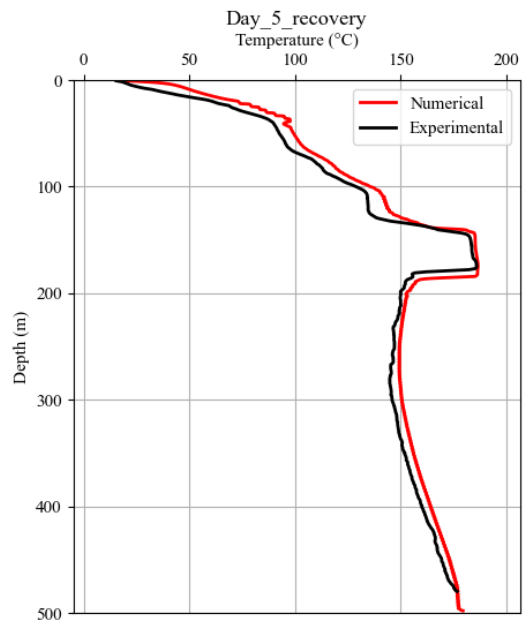
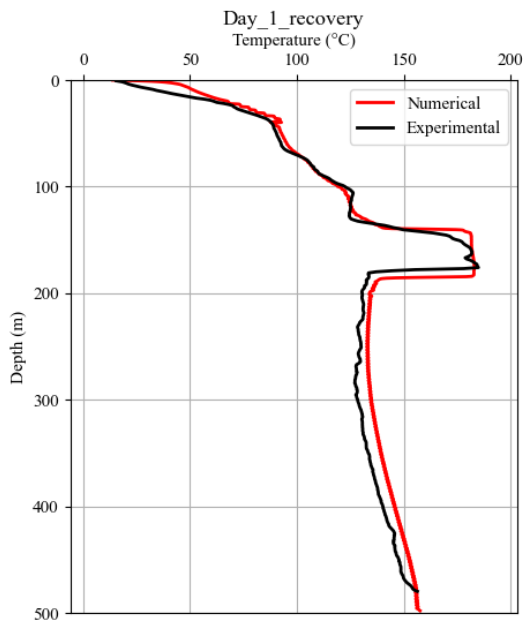
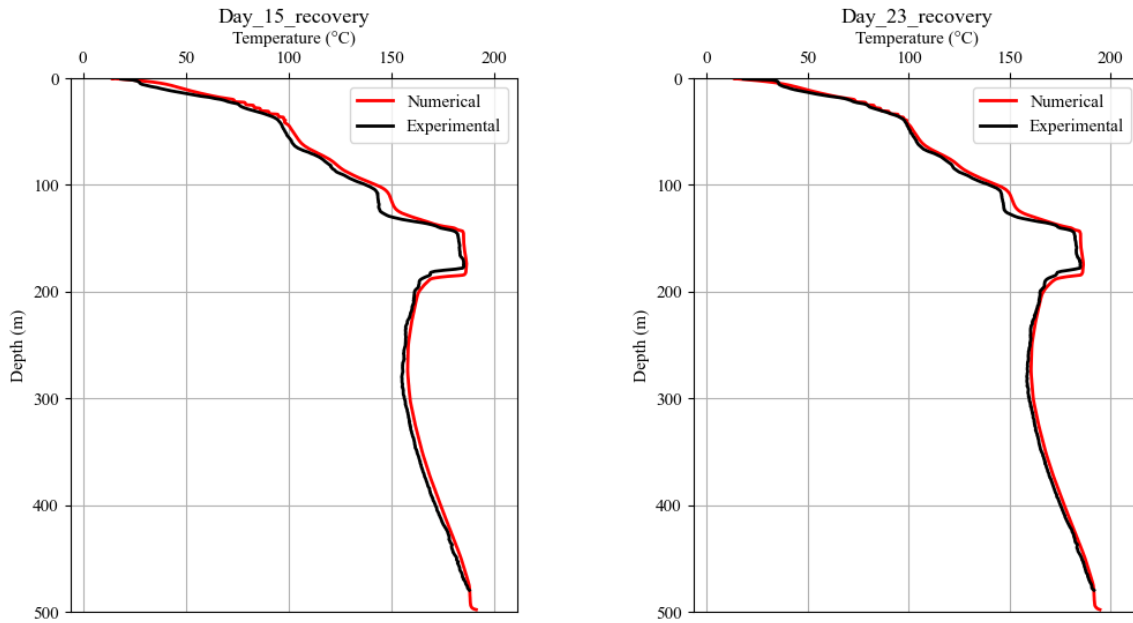


Figure 4-3 Validation results during extraction on different days.





**Figure 4-4 Validation results during recovery on different days.**

**Table 4-3 Calibrated seepage velocity with depth.**

Depth (m)	Seepage velocity (m/s)	Seepage velocity (m/year)
0-20	0.0	0.0
20-40	$4.75 \times 10^{-5}$	1498.0
40-140	$10^{-6}$	31.5
140-185	$7.0 \times 10^{-6}$	220.7
185-500	0.0	0.0

#### 4.5 Discussion on seepage velocities

This section delves deeper into calibrated seepage velocities at different depths, drawing insights from previous literature on the Beppu geothermal system. Firstly, it is essential to comprehend the

topography of Beppu hydrothermal field. The red star in the topography map (Figure 4-5) signifies the location of the current well, situated at an elevation of approximately 500 meters above sea level. The well is positioned on the slope of Mount Garan, which faces Beppu Bay, situated approximately 13 kilometers away from the mountain peak. Precipitation and other thermal discharges from underground sources flow towards the bay through these slopes.

Yusa & Ohsawa [112] discuss the temperature readings of a 300-meter deep well near the current site but at a different elevation (marked as "BGRL" in Figure 4-5). This well was situated at an elevation of approximately 250 m or slightly lower, whereas the current well is positioned roughly 500 meters above sea level. Although this study was conducted in the southern part of Beppu (approximately 3-4 kilometers south of the current well), it points to a significant lateral flow at a depth of 250 m from the well location towards Beppu Bay. A depth of 250 meters in this well corresponds to a depth of 450 meters in the current well. Based on our findings, a pure conduction model is validated for this depth in the current well. This validation affirms the heterogeneity of groundwater movement and its depth variation from the north to the southern region of Beppu.

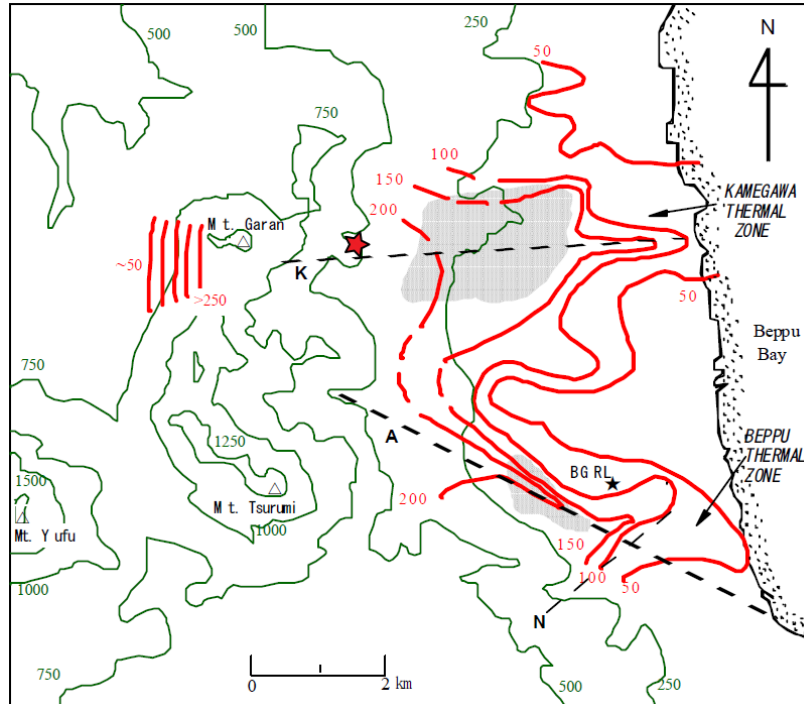


**Figure 4-5** Map of Beppu Hydrothermal Field and red STAR sign is the well location. Thick curves show isotherms in °C at 100 m below sea-level. Shaded areas are two-phase zones. Dashed lines A and K are the Asamigawa and the Kamegawa faults respectively, and dashed line N is an unnamed fault. Elevation contours (m) above mean sea level [112].

Another significant point from past literature is the presence of a fault zone in the vicinity of the well location. Although the exact depths of these fault zones have not been precisely determined, their influence on the geothermal system is evident. Along this flow path, thermal water from the geothermal system in this region ultimately reaches Beppu Bay [112]. Kitaoka and Sturchio also corroborate the existence of a fault zone (referred to as the Kamegawa fault) that passes through the current well location, extending towards Beppu Bay, which is responsible for transporting hot water towards the coast [110], [118]. Literature also points to another prominent fault known as the Asamigwa fault, located approximately 2-3 kilometers south of the current borehole. While the

Asamigwa fault does not interact with the area near the well site, the Kamegawa fault could impact the well directly.

Although the literature is unanimous regarding the flow of thermal water towards Beppu Bay, both at the surface and subsurface levels, quantifying this flow rate and velocity at different depths has proven to be a challenging task. In addition to the surrounding velocity, obtaining temperature data is also expected to pose a significant challenge. According to Allis & Yusa [113], most of the wells drilled for recreational purposes are private, and their owners intend to use the wells immediately, leaving very little chance to obtain temperature data at a later date.

On this note, Allis & Yusa [113] suggested a turnover time of 10-50 years in the shallow regions of this hydrothermal system. This would lead to about 1300 m/year of fluid flow rate, considering about 13 km of distance from Garan peak to Beppu Bay. They also suggested relatively high transmissivities of 100-800 Darcy-m in the shallow region. Another study was performed to observe the vertical velocity of approximately 60 m/year in the region with a residence time of about 50 years [110]. The current study is the most advanced form of experimental data collected in the recent history of the Beppu geothermal system. Hence, based on our findings, we conclude the following points for specific depths at the current well location.

- 0-20 m depth: It is crucial to note that the temperature at this shallow depth is influenced by the water temperature in the heat exchanger annulus during the extraction. This is because the temperature sensor is located at the inner wall of the conductor pipe, and it reads the temperature profile near the immediate vicinity of the heat exchanger. Additionally, during extraction, heat transfer occurs from the inner insulator pipe outward toward the surrounding formation because the water within the inner tube is at a higher temperature. Hence, temperature measurements during the recovery period provide a better

assessment of this depth. The maximum well recovery temperature at the end of the 23<sup>rd</sup> day at 20 m depth reached 71.6°C. The equilibrium temperature obtained for this depth is slightly above the water inlet temperature, which is set at 70°C. Therefore, the presence of lower-temperature seepage could potentially drain thermal energy from the annulus region. However, during the entire extraction period, this phenomenon was not observed. Instead, there was a minor increase in water temperature within the annulus region. This can be attributed to heat transfer from the inner pipe to the outer pipe during the extraction process. Hence, for this depth, a pure conductive zone is identified with no observable fluid movement.

- 20-40 m depth: For this depth, a sharp temperature gain in the CBHE inlet water was observed for all the days of extraction. The temperature gain is certainly higher than the temperature gain due to heat transfer from the inlet pipe to the outer pipe as the temperature increase rate of water in the annulus is higher than that in the shallow region of 0-20 m of depth. According to the simulation results, this sharp gain in water temperature could only be justified with comparatively higher seepage velocity. The seepage velocity obtained for this depth is  $5e-5$  m/s or 1500 m/year. This water is likely coming from hot springs around Mount Garan peak towards Beppu Bay in shallow permeable layers. It is also important to note that the hydraulic conductivity measured on the collected rock sample (Table 3-1) may not truly reflect this higher seepage velocity. A high-pressure gradient ( $\sim 1000$  Pa/m) is needed for such a velocity to exist in accordance with the measured hydraulic conductivity, which is not physically possible. Hence, at this depth, perhaps due to the presence of highly fractured and jointed rocks, a higher flow velocity of subsurface fluid might be present. Another cause of this high flowrate would be the presence of the

Kamegawa fault around this depth and a high flowrate of hydrothermal fluid moving via this fault.

- 40-140 m depth: At this depth, the water temperature in the annulus of the heat exchanger exhibits a moderate rate of increase during extraction. Additionally, it recovers temperature more rapidly compared to the pure conduction model. The velocity that aligns with the recovery profile and provides the best fit for the extraction profile is 31.5 m/year.
- 140-185 m depth: This is the region with higher flow velocity. Even after the first day of the recovery process, almost all of the initial temperature for this depth was recovered. The recovery temperature could only be justified with a velocity of 220.7 m/year. The recovery pattern for some smaller ranges of velocities is presented in Appendix B for reference. This range of flow rate could also be caused by the presence of highly fractured or jointed rocks or the presence of a fault at this depth.
- 185-500 m depth: A pure conductive model for this depth would match both the extraction and recovery temperatures in accordance with the examined rock properties.

## **4.6 Results**

With the validated numerical model, we conducted additional simulations to forecast the performance of the heat exchanger under varying conditions. Initially, we investigated the impact of seepage within the formation, and we conducted a sensitivity analysis in the subsequent section of this chapter.

### **4.6.1 Effect of seepage**

In this section, the effect of calibrated seepage on the performance of the CBHE is analyzed. For this purpose, the outlet temperature from the CBHE system in two different cases is compared;

between the validated numerical model with calibrated seepage velocity and another case, which is a pure conductive case with no presence of fluid. The subsurface initial temperature distribution profile and the far boundary temperature are identical in both cases. Figure 4-6 represents the comparison between these two scenarios. It is found that the outlet temperature from the CBHE system reduces from 87.0°C to 83.5°C when the simulation is switched to a pure conductive model. This corresponds to a decrease in average power from 128.3 kW to 103.2 kW and a reduction of total thermal energy by 19.5% over a 30-year timeframe. Hence the presence of seepage has a considerable effect on the thermal output from the CBHE system.

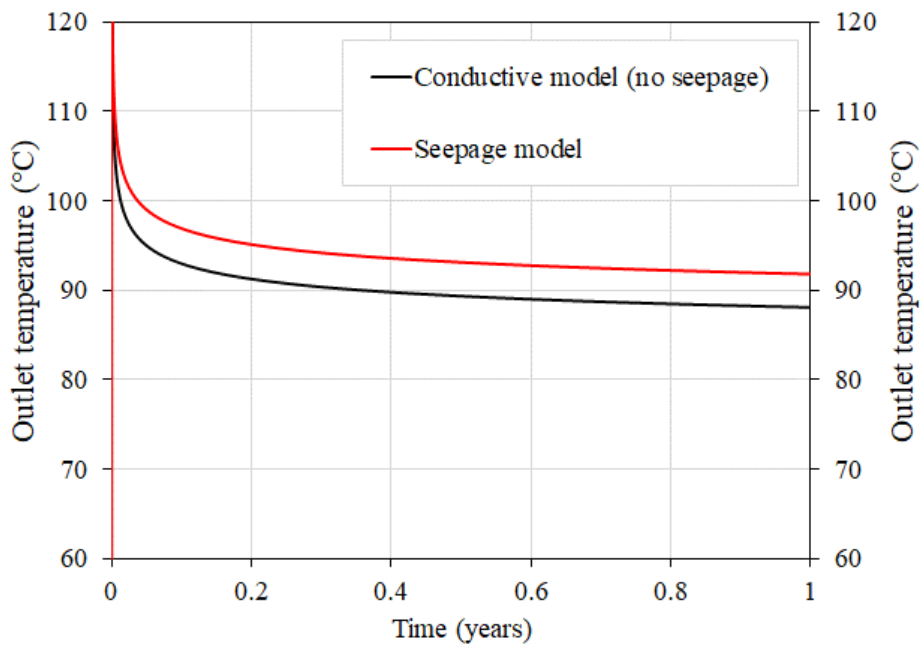


Figure 4-6 Comparing outlet temperature with and without the calibrated seepage.

## **4.6.2 Parametric analysis**

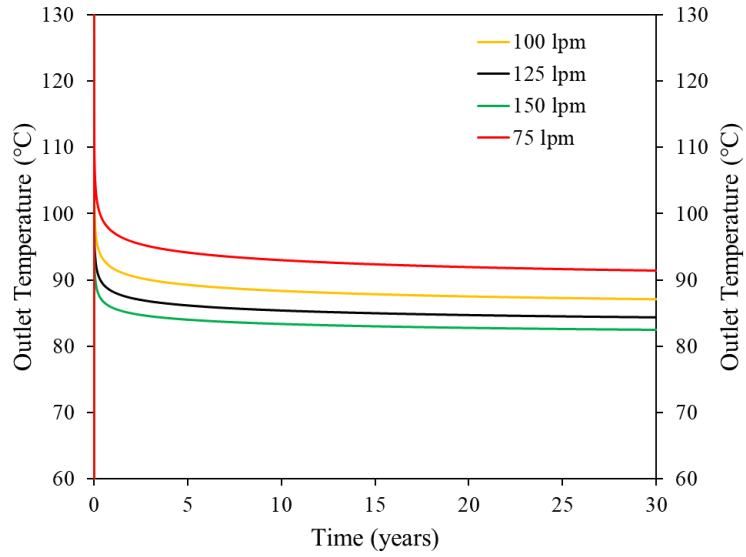
Multiple simulations were conducted to study the impact of design and operational parameters on the CBHE system thermal energy output. Parametric analyses were carried out for a continuous period of 30 years in each scenario. The parameters under scrutiny included flow rate, inlet water temperature, ground thermal conductivity, and thermal conductivity of the insulating pipe.

### **4.6.2.1 Effect of flowrate**

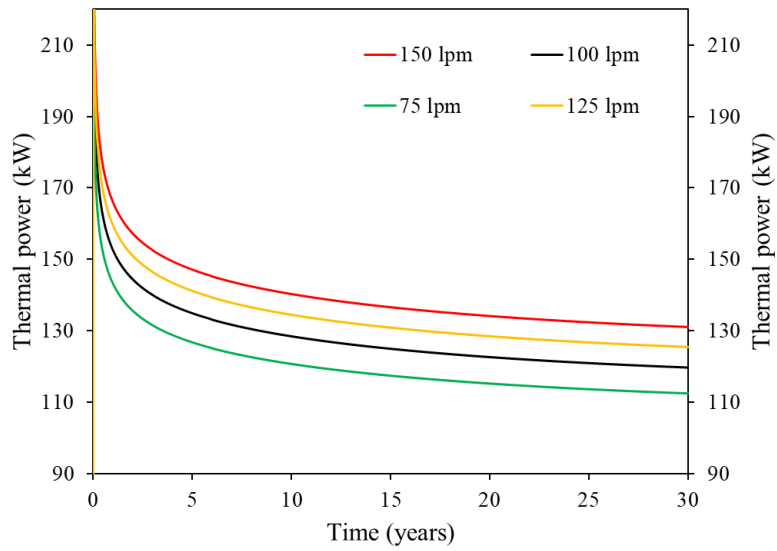
Here, the flow rate of the CBHE system is adjusted to observe its impact on outlet temperature and thermal power output. All other operational parameters are held constant throughout the simulation, including an inlet water temperature of 70°C. Four distinct flow rates are examined, ranging from 75 lpm (or l/min) to 150 lpm with increments of 25 lpm. Outlet temperature, thermal power output, and pressure loss are calculated through the simulation over 30 years.

Figure 4-7(a) and Figure 4-7(b) illustrate the simulation results in terms of outlet temperature and output thermal power, respectively. Similarly, Figure 4-7(c) presents the total pressure loss and total thermal energy yield during the testing duration. Increasing the flow rate leads to a reduction in the outlet temperature, while the thermal power from the system concurrently increases. The outlet temperatures at the end of the 30-year period are determined as 91.4°C, 87.0°C, 84.3°C, and 82.4°C for flow rates of 75 lpm, 100 lpm, 125 lpm, and 150 lpm, respectively. The average thermal power output during the simulation period increases from 120 kW to 140 kW when the flow rate is increased from 75 lpm to 150 lpm. Furthermore, with the same change in flow rate, the total thermal energy generated over 30 years grows by 18.5 TJ, while the pressure loss in the pipe rises from 5.5 kPa to 16.5 kPa. Although higher power output is achieved with a greater flow rate, this comes at the expense of compromised quality of thermal output power and increased pumping

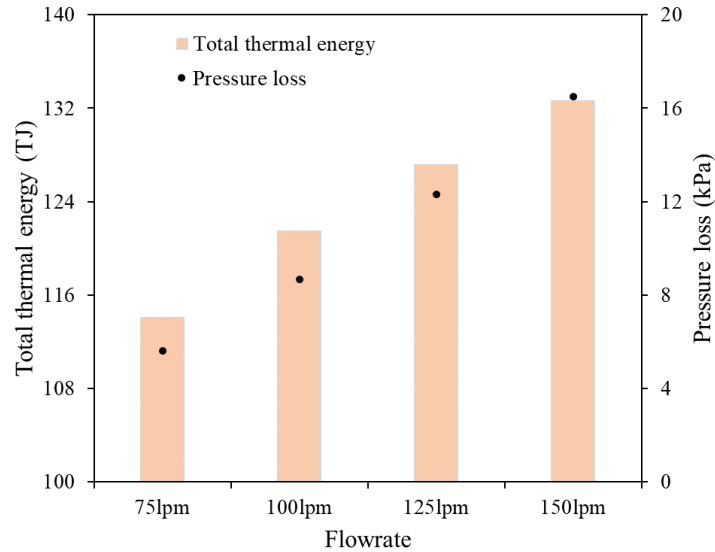
power requirements. Hence, optimization is necessary to determine the most suitable flow rate considering both cost and the application of the generated thermal energy.



(a)



(b)



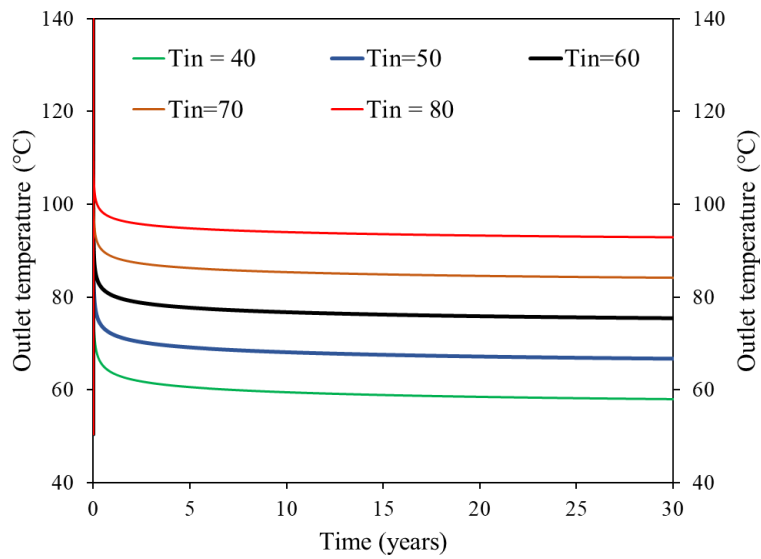
(c)

**Figure 4-7 Parametric study on flowrate variation.**

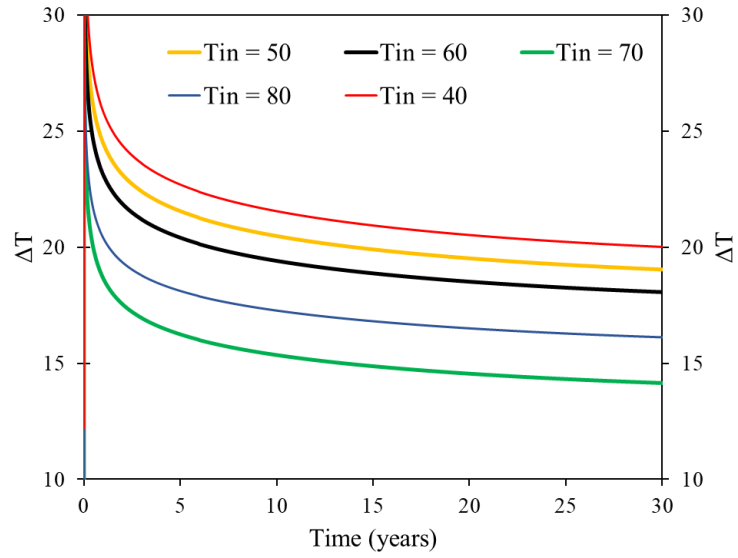
#### 4.6.2.2 Effect of inlet temperature

During the numerical analysis, the inlet temperature was varied within the range of 40°C to 80°C, and its influence was documented in relation to the outlet temperature, total energy generation, average thermal power output, and temperature gained by the Heat Transfer Fluid (HTF) in the heat exchanger. It is evident that when the inlet temperature is higher, the outlet temperature of the water is also higher, as demonstrated in Figure 4-8(a). Consequently, the temperature change of the water within the heat exchanger is presented to provide a deeper insight into the system performance. The most significant temperature change is observed for the lowest inlet water temperature, resulting in the highest power output under this operating condition. Temperature differences of 16.1°C and 20.0°C are recorded for inlet temperatures of 80°C and 40°C, respectively, as illustrated in Figure 4-8(b).

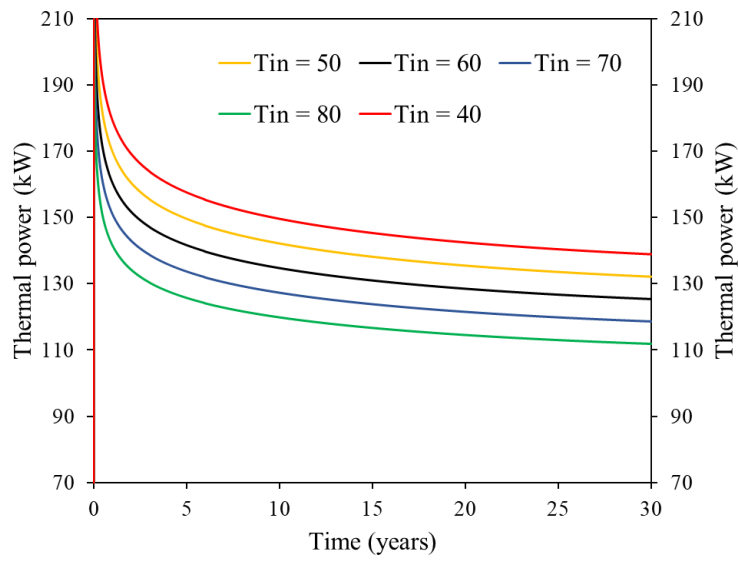
Similarly, lower inlet temperatures yield higher average thermal power outputs; however, this comes at the expense of compromised thermal energy quality. According to Figure 4-8(c), an average power output of 149.5 kW is achieved for an inlet water temperature of 40°C, while an output power of 119.75 kW is attained for an inlet temperature of 80°C. This discrepancy also affects the total thermal energy generated over thirty years, shifting from 141.5 TJ to 113.3 TJ as depicted in Figure 4-8(d).



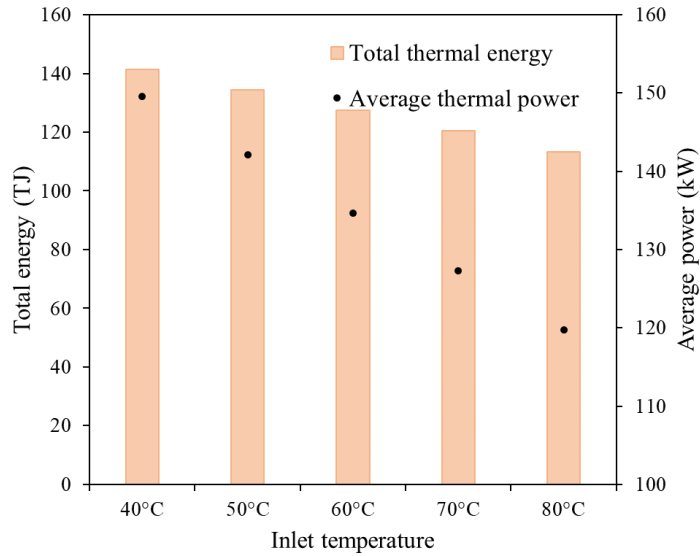
(a)



(b)



(c)



(d)

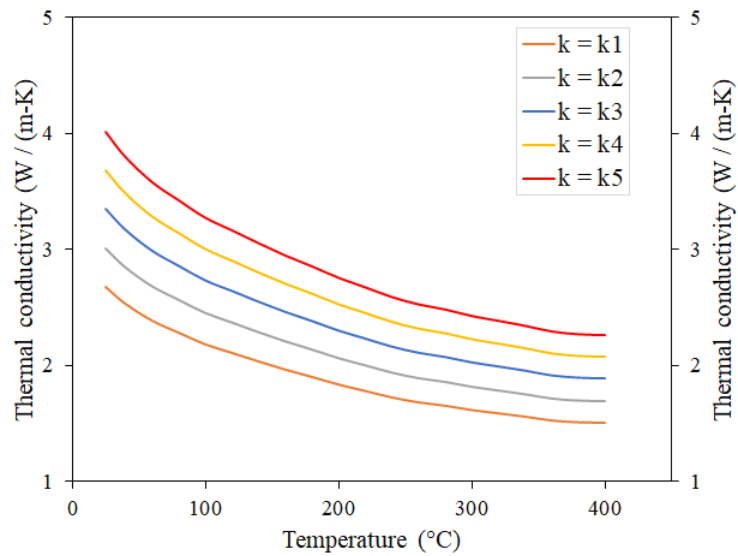
**Figure 4-8 Parametric study results on inlet water temperature.**

#### 4.6.2.3 Effect of ground thermal conductivity

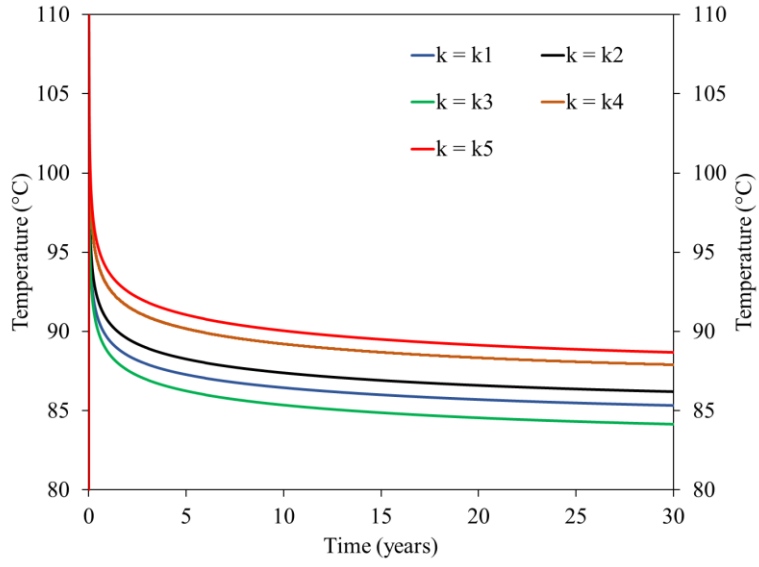
This section presents the results of the CBHE system with changes in the thermal conductivity of the ground. The thermal conductivity is both increased and decreased from the base case scenario of the measured value in the lab, denoted as  $k = k_3$  in Figures 4-9(a), 4-9(b), 4-9(c), and 4-9(d). Conductivities corresponding to  $k_1$ ,  $k_2$ ,  $k_4$ , and  $k_5$  are 80 %, 90 %, 110%, and 120% of the measured thermal conductivity, respectively. The comparison of these thermal conductivities is presented in Figure 4-9(a).

It is observed that the thermal conductivity of the ground significantly influences the performance of the system in terms of power generation and the outlet temperature. A higher thermal conductivity facilitates more efficient heat transfer within the rock formation towards the lower-temperature borehole. Consequently, more heat is absorbed by the Heat Transfer Fluid (HTF) from the conductor pipe. This results in a higher outlet temperature of the HTF and an increased thermal

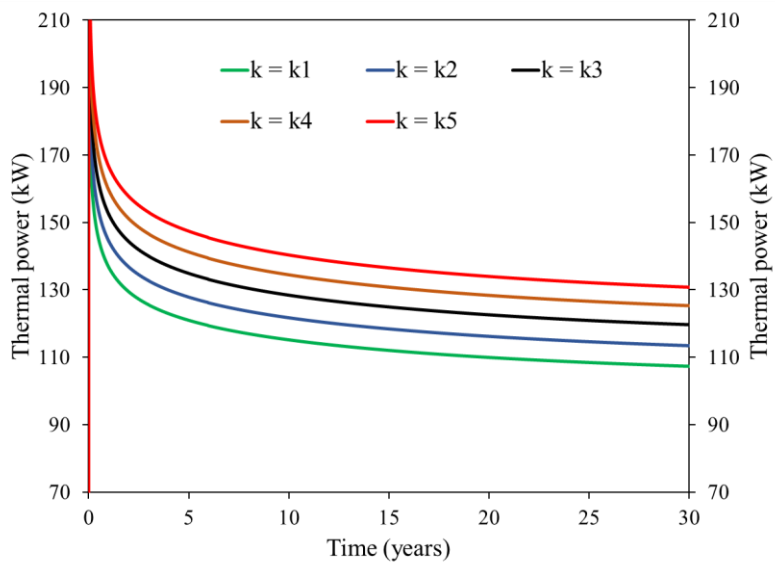
power output from the system, as depicted in Figure 4-9(b) and Figure 4-9(c). As shown in Figure 4-9(d), the total thermal energy extracted from the system reaches 108.9 TJ to 132.8 TJ when the thermal conductivity of the ground increases from  $k_1$  to  $k_5$ . This corresponds to a 21.8% increase in energy compared to the initial system. Similarly, the average power generated by the CBHE system is 115.2 kW, 121.7 kW, 128.4 kW, 134.5 kW, and 140.3 kW for conductivities of  $k_1$ ,  $k_2$ ,  $k_3$ ,  $k_4$ , and  $k_5$ , respectively.



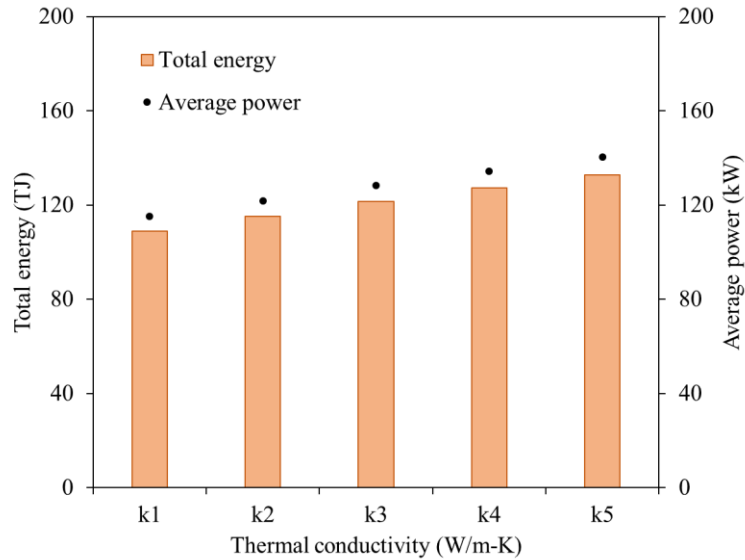
(a)



(b)



(c)

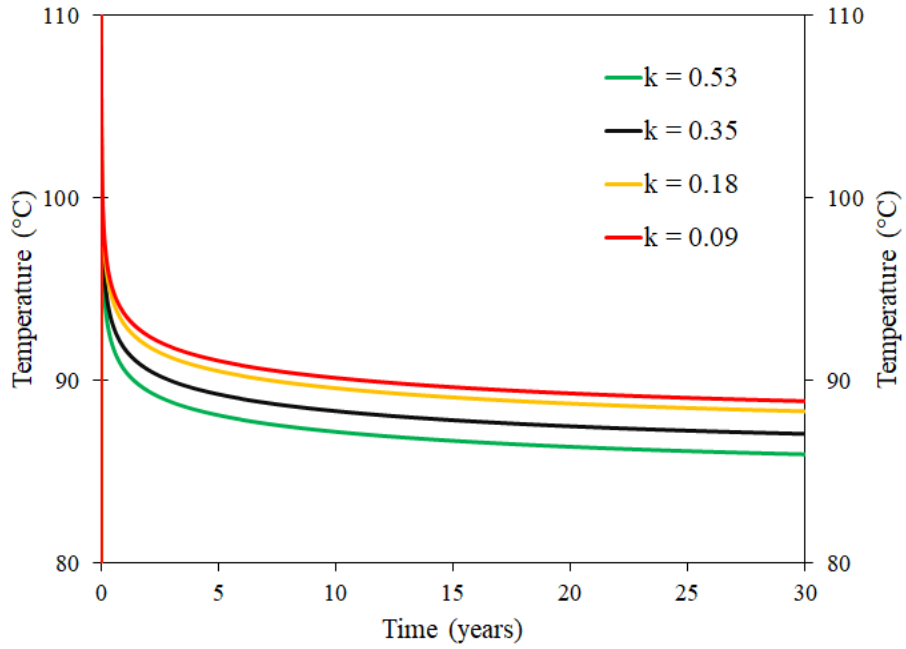


(d)

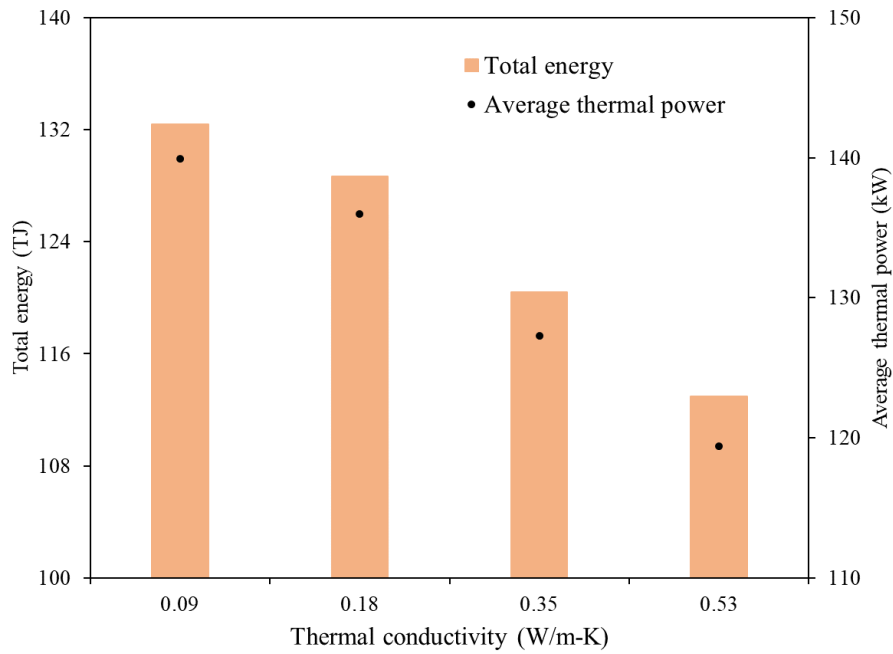
**Figure 4-9 Parametric study results on thermal conductivity of ground.**

#### **4.6.2.4 Effect of insulator pipe thermal conductivity**

In this section, the thermal conductivity of the inner insulated pipe is varied to observe its effect on the CBHE system. The water that exchanges heat with the subsurface in the annulus region exits from this pipe to the surface. Water at the bottom of the borehole carries high temperature, resulting in heat loss as it ascends to the earth surface through the inner insulated pipe. The simulation revealed that a lower thermal conductivity of the insulating pipe leads to improved CBHE performance. The system outlet temperature increased from 86.0°C to 87.8°C when reducing the thermal conductivity from 0.53 W/(m-K) to 0.09 W/(m-K). This is presented in Figure 4-10(a). Similarly, from Figure 4-10(b), with the exact change in thermal conductivity, the total thermal energy extracted from the system increased from 113.0 TJ to 132.4 TJ. Hence, for better thermal performance, it is recommended to use an inner pipe with a lower thermal conductivity.



(a)



(b)

**Figure 4-10 Parametric study on insulator pipe thermal conductivity.**

## 4.7 Conclusions

A three-dimensional conjugate fluid flow and heat transfer numerical model is developed using a finite volume approach to calibrate seepage velocity, validate the numerical model, and predict the performance of the CBHE. A depth-varying seepage velocity that aligns with the experimental temperature distribution of the subsurface is calibrated. Numerical results are validated against the experimental outcomes in terms of outlet temperature and the ground temperature distribution profiles for the extraction-recovery period. The model is employed to simulate the CBHE system under different design and operating conditions. Findings indicate the presence of three distinct seepage velocities at different depths. The calibrated seepage velocity has an impact of about 20% on the thermal output from the system. Sensitivity analysis indicates that a higher mass flow rate leads to increased thermal power output and greater energy generation. However, it also requires more pumping power, leading to a decreased outlet fluid temperature. Additionally, while a higher inlet temperature results in a higher outlet temperature, it generates less power and energy. The thermal conductivity of the ground is directly proportional to the outlet temperature, power, and energy generated by the geothermal system. For improved thermal performance, it is recommended to use an insulating pipe with a lower thermal conductivity.

## Chapter 5: Reduced Order 1+3D Numerical Model for Evaluating the Performance of Coaxial Boreholes in Solar Geothermal Heating System

### Preface

In this chapter, we present the development of a numerical model for the heat and mass transfer mechanisms in a rectangular array of ( $N \times M$ ) coaxial boreholes used in a solar-geothermal heating system. Additionally, we design a solar-geothermal heating system using the developed model for a large size residential building located in Ontario, Canada. Furthermore, we also discuss the economic and environmental analysis associated with replacing a natural gas heating system with the proposed solar-geothermal system for the considered building size.

Publications from this chapter:

- **Pokhrel, Sajjan**, Amiri, L., Poncet, S., & Ghoreishi-Madiseh, S. A. (2023). Reduced order 1+ 3D numerical model for evaluating the performance of solar borehole thermal energy storage systems. *Journal of Energy Storage*, 66, 107503.
- **Pokhrel, Sajjan**, Amiri, L., Poncet, S., Sasmito, A. P., & Ghoreishi-Madiseh, S. A. (2022). Renewable heating solutions for buildings; a techno-economic comparative study of sewage heat recovery and solar borehole thermal energy storage system. *Energy and Buildings*, 259, 111892.

## 5.1 Introduction

This study presents a computationally efficient numerical model for solving the fluid flow and heat transfer phenomena in co-axial borehole heat exchangers arranged on a rectangular grid ( $N \times M$ ) pattern. Such systems of boreholes are an integral component of a solar-geothermal heating system for seasonal thermal energy storage applications. The numerical model couples a one-dimensional fluid flow and convective heat transfer model in the heat exchanger with a three-dimensional model of conductive heat transfer in the rock strata. In addition to solving mass and heat transfer in borehole systems, the developed model integrates a solar thermal collector system and building dynamic thermal load. This integration is aimed at designing a solar-geothermal system for an 826-unit residential apartment building. The simulation also considers and evaluates the conductive, convective, and radiative thermal losses from the system. The model is validated using experimental data from a coaxial borehole heat exchanger and compared to the results of a commercial finite volume solver for multiple coaxial boreholes. It also examines the economic viability and environmental impact of substituting natural gas boilers with solar-geothermal systems. The capital and operating costs of the proposed solar-geothermal system and the existing natural gas heating system are evaluated and compared, as well as the energy savings and the payback period. The computational cost of the developed numerical model is 194 times less than that of a commercial finite volume solver.

Solar-geothermal system simulation is performed for five years considering hourly fluctuations in solar irradiance and building dynamic thermal energy demand. A parametric study is performed on the depth and spacing of boreholes, and mass flow rate in the solar thermal collectors. It is found that a system of 450 boreholes, each 100 m deep, linked to 3032 solar thermal collectors can provide the heating for the building with a total thermal demand of 25 TJ per year. The findings

show that the solar-geothermal system is technically feasible to execute on the studied construction site. The financial viability of other sites is determined by the difference in the unit cost of energy from electricity and natural gas.

## **5.2 System schematics**

Figure 5-1 represents the system-level design schematics of a solar-geothermal heating system. The system runs on solar energy, which is collected in the form of thermal energy using solar thermal collectors. To acquire thermal energy from solar radiation, a Heat Transfer Fluid (HTF) such as water or glycol is pumped through the solar collectors. The HTF from the collectors is routed to a short-term storage tank, where it is temporarily stored. Hot HTF is either sent to the building to meet the building thermal demand at the time, or it is sent to boreholes to be stored underground. Each borehole is a Coaxial Borehole Heat Exchanger (CBHE). The system of CBHEs in this thesis is also referred to as the Borehole Thermal Energy Storage (BTES) system, as it stores thermal energy from solar collectors. When the building demand exceeds the solar availability, this stored thermal energy is withdrawn from the BTES system. This could happen during low-solar-availability hours of the day when available solar energy does not meet the building thermal demand or during non-solar hours. Solar irradiance is higher in the summer and lower in the winter in northern areas such as Canada. Due to this solar pattern, thermal energy from the collectors is stored in the boreholes largely in the summer and retrieved in the winter resulting in seasonal thermal storage.

### 5.3 Building description

The total land area available for the building site is 73,500 m<sup>2</sup>. The proposed complex will have a total of 826 apartments in two 17-floor buildings. A total area of 35,000 m<sup>2</sup> is allocated for the solar system installation. This project will combine all conceivable technologies to support and endure as a self-sufficient complex using renewable and alternative energy for space and water heating.

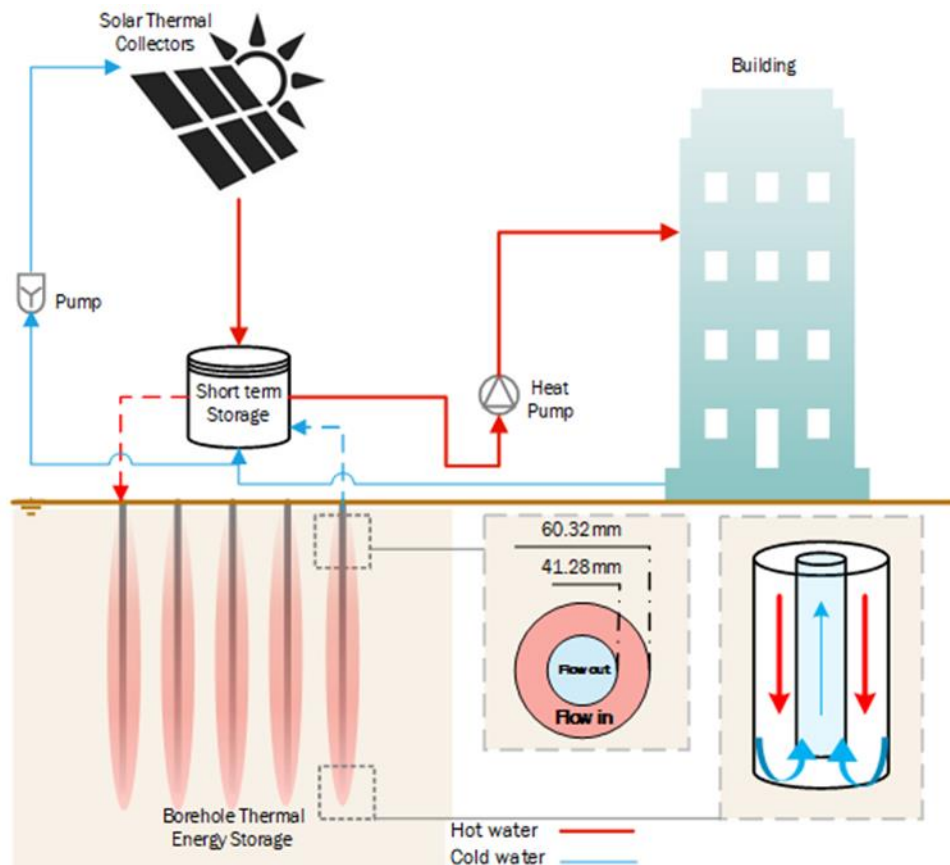


Figure 5-1 Solar-geothermal heating system schematics.

## 5.4 Methodology

BTES, solar thermal collectors, and the building thermal demand are the three primary components of the solar-geothermal system. The first step in developing the dynamic solar-geothermal system model is programming the 1+3D model to solve heat and mass transfer processes in BTES. Dynamic building thermal demand and dynamic solar yield were incorporated into the developed model after model validation. To obtain simulation results for the considered solar-geothermal system, dynamic simulations were performed on an hourly basis for five years. The process for developing the 1+3D code, estimating the building heat demand, designing a solar collector system, and compiling the integrated solver are all covered in the subsections that follow.

### 5.4.1 1+3D model development

1+3D model solves the heat and mass transfer mechanisms in BTES system. In this model, a one-dimensional flow equation in boreholes is coupled with a 3-dimensional heat transfer equation outside the boreholes or in the surrounding rock or soil mass. Associated equations in the heat exchanger and the surrounding rock or soil mass are explained in the next section.

BTES consists of  $N \times M$  co-axial boreholes with specific depths and spacing between the boreholes. A schematic of a co-axial borehole heat exchanger is presented in Figure 5-2(a), which consists of two concentric pipes with different diameters. HTF is pumped into the borehole from the annulus region after which the fluid exchanges thermal energy between HTF and surrounding soil mass via conductor pipe. The inner pipe is an insulator pipe that carries HTF from the bottom to the outlet with a minimum heat transfer. A system of 16 such boreholes in a 4×4 rectangular field borehole system is shown in Figure 5-2(b). The X-Y plane is parallel to the Earth surface and the vertical Z- axis is the pipe length.

Geometry development and discretization are the first steps in model development. The number of boreholes, their depth, and the layout of the three-dimensional control volume could be changed based on the user input in the developed numerical code. The discretization process follows model development. The full control volume is discretized into uniformly sized and cubed-shaped smaller control volumes in this step. There are two types of elements in the domain, those with heat exchangers and those without as shown in Figure 5-3. These are also called source term and non-source term elements. Elements with a heat exchanger in them are called source-term elements since heat is either absorbed or rejected by these elements via the HTF. Figure 5-3, which depicts the top discretized view of the domain, has both types of these elements. An example of a source term element is highlighted in red, while an example of a non-source term element is shown in green. The energy equation is solved in each of these control volumes for each time step to obtain the time-dependent temperature distribution.

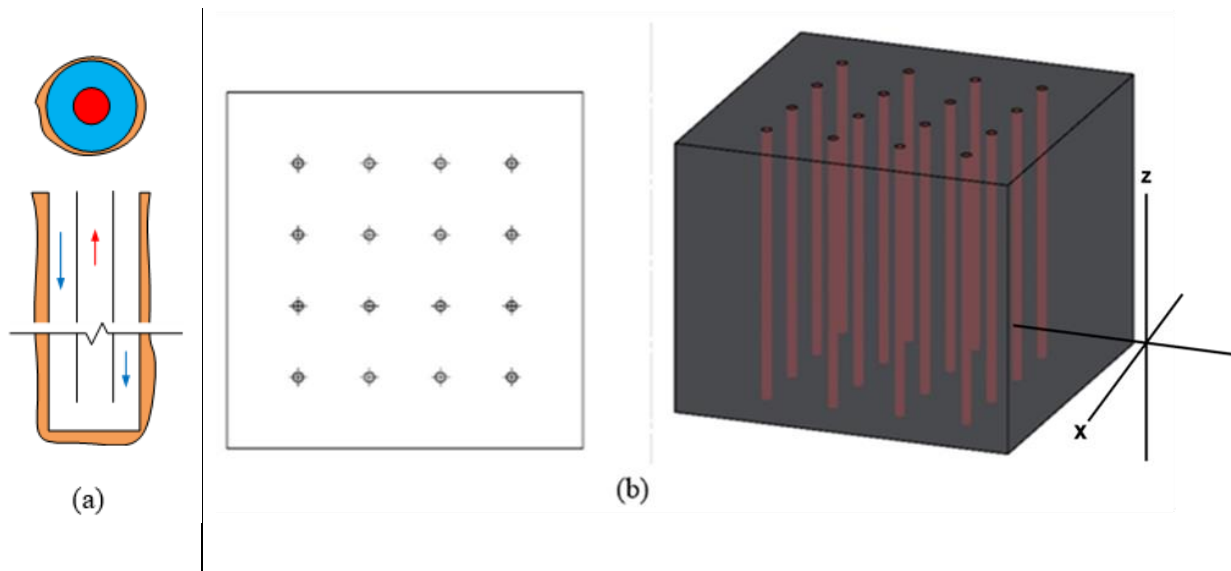


**Figure 5-2 (a) Co-axial borehole heat exchanger during heat extraction, (b) top and isometric view of the three-dimensional geometry of the BTES domain.**

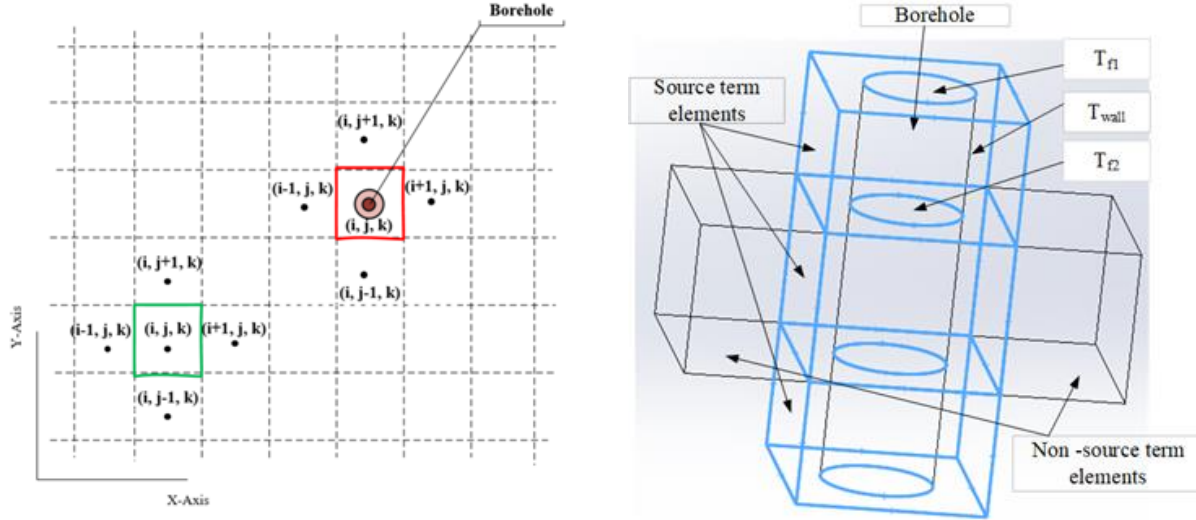


**Figure 5-3 Top discretized view of the domain section with a borehole in it (left) and a conceptual figure representing source and non-source term elements (right).**

#### 5.4.1.1 Governing equations

The unsteady-state heat transfer mechanism in the solid domain without any source term is governed by Equation (5.1).

$$\rho C_p \frac{\partial}{\partial t} T = \nabla \cdot (k \nabla T) \quad (5.1)$$

Where,  $\rho$ ,  $C_p$ ,  $k$ , and  $T$  are the density, specific heat capacity, thermal conductivity, and temperature of a control volume, respectively. Similarly, for the elements with the source term, this equation becomes:

$$\rho C_p \frac{\partial}{\partial t} T = \nabla \cdot (k \nabla T) + S_h \quad (5.2)$$

Where,  $S_h$  is the source term that represents the quantity of heat either added or removed from the control volume. Similarly, the mathematical formulation of the Heat Transfer Fluid is performed by the Log Mean Temperature Difference (LMTD) approach defined by Equation (5.3). LMTD

approach determines the effective representation of temperature difference between the two ends of heat exchanger and is widely being used for designing different heat exchangers [119]. According to this model, heat transfer in the element with source term is given by Equation (5.4). The variables  $T_{wall}$ ,  $T_{f1}$ , and  $T_{f2}$  are defined in Figure 5-3(right), where  $T_{wall}$  is the temperature of the wall of the heat exchanger,  $T_{f1}$  and  $T_{f2}$  are the temperature of the HTF at the entrance and exit of the heat exchanger, respectively.

$$LMTD = \frac{(T_{f2} - T_{wall}) - (T_{f1} - T_{wall})}{\ln\left(\frac{T_{f2} - T_{wall}}{T_{f1} - T_{wall}}\right)} \quad (5.3)$$

$$\dot{Q} = hA(LMTD) \quad (5.4)$$

Where  $h$  is the convective heat transfer coefficient of the fluid and  $A$  is the cross-sectional area of the contact between the heat exchanger and the ground given by:

$$A = \pi \times D \times \Delta Z \quad (5.5)$$

where  $D$  and  $\Delta Z$  are the outer diameters of the borehole which is in contact with the rock and the source term grid element length in the Z-direction, respectively. Similarly, heat transfer to the rock mass from the HTF is governed by:

$$\dot{Q} = m_f c_{p,f} (T_{f2} - T_{f1}) \quad (5.6)$$

From the conservation of energy principle, heat transfer from the HTF should be equal to the amount of heat received by the soil and vice versa. Hence, from Equations (5.4) and (5.6), the HTF temperature at the exit of the heat exchanger can be obtained as follows:

$$T_{f2} = T_{wall} - (T_{wall} - T_{f1}) \times e^{-\left(\frac{h\pi D \Delta Z}{m_f c_{p,f}}\right)} \quad (5.7)$$

The second-order centered discretization scheme in space and the explicit Euler scheme in time are implemented to compute the numerical solution. The resulting discretized energy equation with non-source term elements is

$$T_{i,j,k}^{n+1} = T_{i,j,k}^n + k_g \rho_g C_{p,g} \Delta t \left( \frac{T_{i+1,j,k}^n - 2T_{i,j,k}^n + T_{i-1,j,k}^n}{\Delta x^2} \right. \quad (5.8)$$

$$\left. + \frac{T_{i,j+1,k}^n - 2T_{i,j,k}^n + T_{i,j-1,k}^n}{\Delta y^2} + \frac{T_{i,j,k+1}^n - 2T_{i,j,k}^n + T_{i,j,k-1}^n}{\Delta z^2} \right)$$

where, n is the time step number and i, j, and k are unit direction vectors in X, Y, and Z directions, respectively. Similarly, for a cell with a source term governed by Equation (5.2), the discretized equation is represented in Equation (5.9). The term  $\frac{m_f C_{p,f} \Delta T}{\rho_g C_{p,g} \Delta x \Delta y \Delta z}$  represents  $S_h$  in Equation (5.2).

$$T_{i,j,k}^{n+1} = T_{i,j,k}^n + k_g \rho_g C_{p,g} \Delta t \left( \frac{T_{i+1,j,k}^n - 2T_{i,j,k}^n + T_{i-1,j,k}^n}{\Delta x^2} \right. \quad (5.9)$$

$$\left. + \frac{T_{i,j+1,k}^n - 2T_{i,j,k}^n + T_{i,j-1,k}^n}{\Delta y^2} + \frac{T_{i,j,k+1}^n - 2T_{i,j,k}^n + T_{i,j,k-1}^n}{\Delta z^2} \right)$$

$$- \frac{m_f C_{p,f} \Delta t}{\rho_g C_{p,g} \Delta x \Delta y \Delta z} (T_{f2} - T_{f1})$$

#### 5.4.1.2 Initial and boundary conditions

The initial condition is assigned based on the initial ground temperature distribution of the rock, which is a measured value for the location. This is given by Equation (5.10). Domain independence

test is conducted such that the far boundary condition of constant temperature is used. Far boundary temperature is a function of depth and is represented by Equation (5.11). Similarly, convection and radiation heat transfer boundary conditions are imposed at the top surface as given by Equation (5.12).

$$T_{(x,y,z,o)} = f(y) \quad (5.10)$$

$$T_{(walls,t)} = f(y) \quad (5.11)$$

$$-k_g \left. \frac{\partial T_g}{\partial n} \right|_{topwall} = h(T_g - T_a) + \epsilon \sigma (T_g^4 - T_a^4) \quad (5.12)$$

This study utilizes the explicit Euler scheme to solve the heat equation. The explicit Euler method is a first-order accurate method that introduces numerical errors proportional to the time step size, resulting in a conditionally stable numerical method. Therefore, the time step size must satisfy a stability condition to prevent numerical instability in the solution. For the centered second-order space discretization scheme used in this study, the von Neumann stability analysis yields a stability condition of  $\Delta t \leq (\Delta x^2) / (2a)$ , where  $\Delta x$  is the grid spacing and  $a$  is the thermal diffusivity. This condition determines the maximum allowable time step size for the analysis.

Assumptions made in the numerical analysis are:

- a) Based on field measurement data, the soil is homogeneous throughout the depth; hence soil thermal properties do not vary along the axial or radial direction.

- b) No heat transfer is assumed from the inner insulator pipe, and grout is not considered in the analysis.
- c) The presence of permeability degrades the performance of solar-geothermal systems as it washes away the thermal energy stored. Soil domain is assumed as non-permeable and hence no presence of seepage.
- d) The range of the HTF average temperature change is 6°C to 30°C. Hence, HTF properties do not change with temperature.

#### **5.4.2 Conjugate model development**

The  $4 \times 4$  borehole is generated in ANSYS Fluent, and a conjugate simulation is performed to validate the developed numerical model on multiple heat exchangers. For this, a rectangular borehole geometry filled with sixteen boreholes is generated and meshed. Generated mesh and its top surface magnified view at the inlet of four boreholes are displayed in Figure 5-4(a) and Figure 5-4(b), respectively. The top surface arrows represent the inlet of the sixteen boreholes in Figure 5-4(a). A boundary independence test is performed to determine the distance between boreholes and the far wall boundary. A mesh-independent test is performed to determine the optimum mesh size.

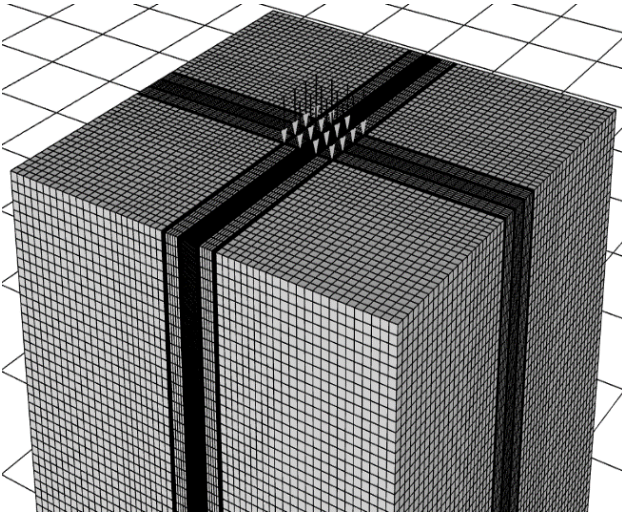
The pure conduction heat transfer mechanism takes place in the solid domain while the convective heat transfer process takes place in the boreholes. The pure conduction phenomenon in the soil is governed by Equation (5.1). Similarly, the fluid flow and heat transfer process in the borehole is obtained by solving the mass, momentum, and energy equations represented by Equations (5.13), (5.14), and (5.15) respectively.

$$\nabla \cdot (\vec{v}) = 0 \quad (5.13)$$

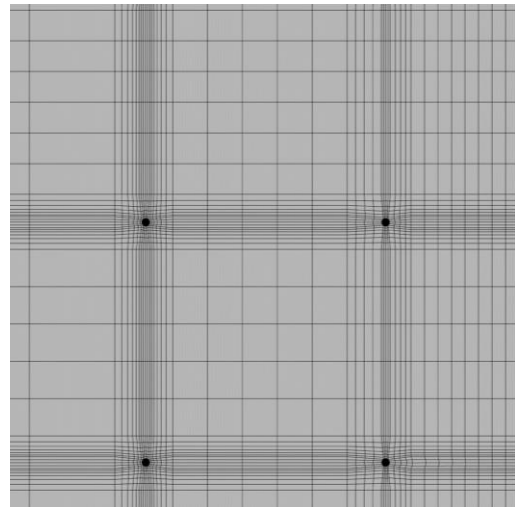
$$\frac{\partial}{\partial t}(\rho \vec{v}) + \nabla \cdot (\rho \vec{v} \vec{v}) = -\nabla p + \nabla \cdot (\bar{\tau}) + \rho \vec{g} \quad (5.14)$$

$$\rho_f c_{p,f} \frac{\partial}{\partial t} T + \nabla \cdot (\rho_f c_{p,f} \vec{v} T) = \nabla \cdot (k_f \nabla T_g) \quad (5.15)$$

In Equations (5.13), (5.14), and (5.15), subscript  $g$  represents the ground. Subscript  $f$  is HTF, and  $T$ ,  $\rho$ ,  $c_p$ ,  $t$ ,  $\vec{v}$  and  $k$  are the temperature, density, specific heat, time, velocity vector, and thermal conductivity, respectively. These governing equations are solved by a Finite Volume Solver, ANSYS Fluent version 2020 R2. Identical boundary conditions are employed at the boundaries, convection, and radiation at the top surface, and isothermal boundary conditions at the side walls. Numerical simulations are performed by varying the inlet temperature and mass flow rate and the outlet temperature is recorded and compared with the output of the developed 1+3D numerical solver.



(a)



(b)

**Figure 5-4 (a) Domain discretization of a conjugate model, and (b) magnified top view with the four boreholes inlet.**

### **5.4.3 Building thermal demand**

After the fluid flow and heat transfer model development, the numerical code is extended to incorporate the building thermal demand and solar thermal collector system. Before incorporating these two parameters, the estimation of the building thermal demand and design of the solar thermal collector system is of critical importance.

The considered building has a total number of apartment units of 826 and a total floor area of 58,500 square meters. The location of the building under consideration is Ontario, Canada. Heating Degree days (HDD) are calculated to measure how cold the considered location is over a year using Equation (5.16). The housing project is specifically designed for senior residents, and the building balance temperature for comfortable living is set slightly higher at 21°C, which exceeds the typical standard of around 18-19°C used for general purposes. The total number of Heating Degree Days (HDD) obtained for the examined location is 6160.

$$HDD = \sum_{i=1}^N (T_b - \bar{T}_i)^- \quad (5.16)$$

Here, N is the number of days in a month,  $T_b$  is the base temperature to which the degree days are calculated, and  $\bar{T}_i$  is the mean daily temperature calculated by adding the maximum and minimum temperatures for a given day, then dividing by 2. The superscript – indicates that only the positive values are considered. The total thermal load of buildings is contributed by fresh air heating demand, envelope thermal energy loss, and hot water heating demand.

#### 5.4.3.1 Fresh air intake

Flowrate for fresh air needed is approximated with a rate of 0.06 cfm ft<sup>-2</sup>[120]. Overall fresh air intake for buildings is computed from Equation (5.17), where the suffixes *b* and *a* reflect the balance and ambient temperatures, respectively. The thermal load is calculated on an hourly basis using the location historical ambient temperature.

$$\dot{Q}_{f-a} = \dot{m}c_{p,air}(T_b - T_a) \quad (5.17)$$

#### 5.4.3.2 Envelope thermal loss

Heat is released into the surrounding environment, due to its lower temperature than the building. This heat escapes through walls, windows, floors, and roofs. The area of each of these parts is determined independently, and the heat loss is calculated using the R-values of the construction materials. Composite material walls with higher filler content are used in the analysis with an R-value of 4.75 m<sup>2</sup>kW<sup>-1</sup>. The insulated aluminum frame windows have an R-value of 0.44 m<sup>2</sup>kW<sup>-1</sup> [121]. Similarly, 3.52 m<sup>2</sup>kW<sup>-1</sup> is used for roofs and floors. Equation (5.18) gives the total heat loss from buildings. Suffices *w*, *win*, *r*, and *fl* represent walls, windows, roof, and floor respectively.

$$\dot{Q}_{h-l} = (T_b - T_a) \times (R_w \times A_w + R_{win} \times A_{win} + R_r \times A_r + R_{fl} \times A_{fl}) \quad (5.18)$$

#### 5.4.3.3 Hot water demand

When calculating the hot water needs for a building, an assumption is made. Hot water demand is consistent throughout the year, regardless of the season. Equation (5.19) is used to calculate the amount of energy required to meet the hot water consumption demand. Here, suffices *b* and *i*

represent the balance and initial temperatures, respectively. A required hot water temperature of 60 °C is chosen in the analysis.

$$\dot{Q}_{h_w} = \dot{m}c_{p,water}(T_b - T_i) \quad (5.19)$$

Heat load is evaluated on an hourly basis. Using Equations (5.17), (5.18), and (5.19), the total heat load of buildings is calculated as:

$$\dot{Q}_{tot} = \dot{Q}_{f_a} + \dot{Q}_{h_l} + \dot{Q}_{h_w} \quad (5.20)$$

Hence, Equation (5.21) gives the total annual energy demand of the considered apartment units in kWh.

$$E_{tot} = \sum_{i=1}^{8760} \frac{\dot{Q}_{tot}}{1000} \quad (5.21)$$

Figure 5-5 represents the annual energy and power demand of the building. The maximum and minimum power and energy demand are in January and July, respectively.

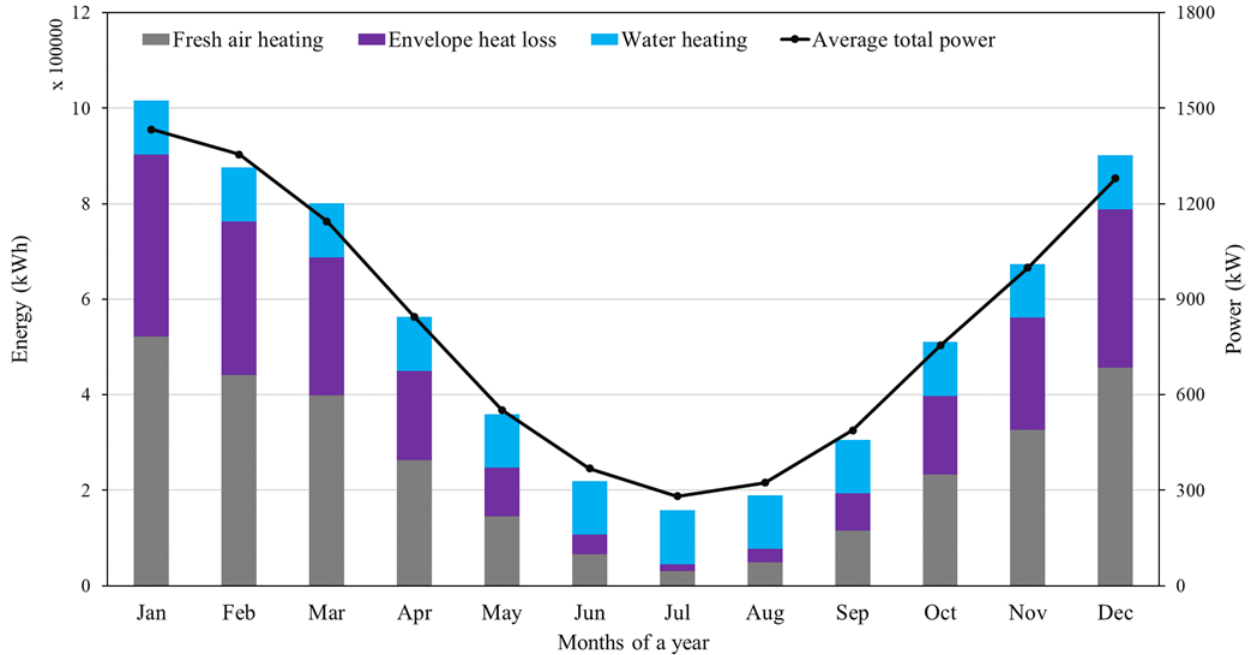


**Figure 5-5 Annual thermal power and energy demand of the building.**

#### **5.4.4 Solar field design**

Similarly, the next step is the design of the solar thermal collector system. This solar collector field is a function of solar availability, collector performance, and building load demand. Solar energy available for the location under consideration is presented in Figure 5-6. This graph has a horizontal axis where the starting point, represented by the number 0, corresponds to the first day of January, and the endpoint, represented by the number 365, corresponds to the last day of the year, which is the 31st of December. Figure 5-7 presents the performance of the solar thermal collector under different HTF temperatures in solar collectors [122].

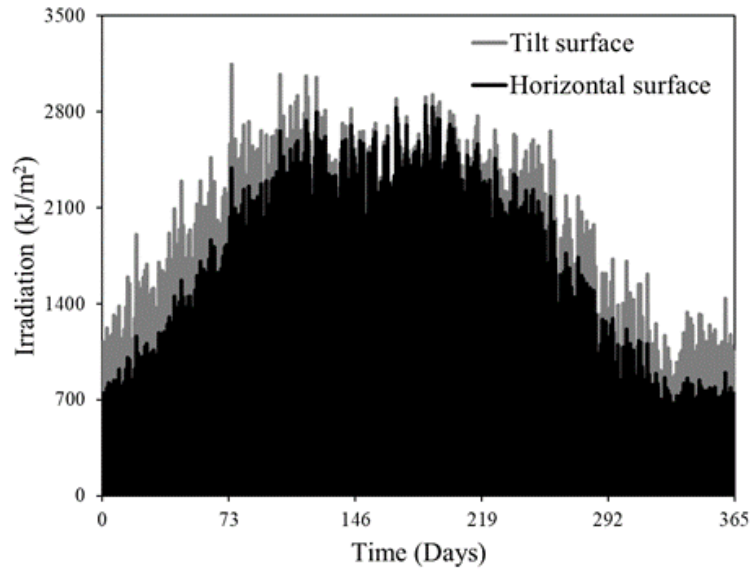


**Figure 5-6 Available solar irradiation for the studied location.**

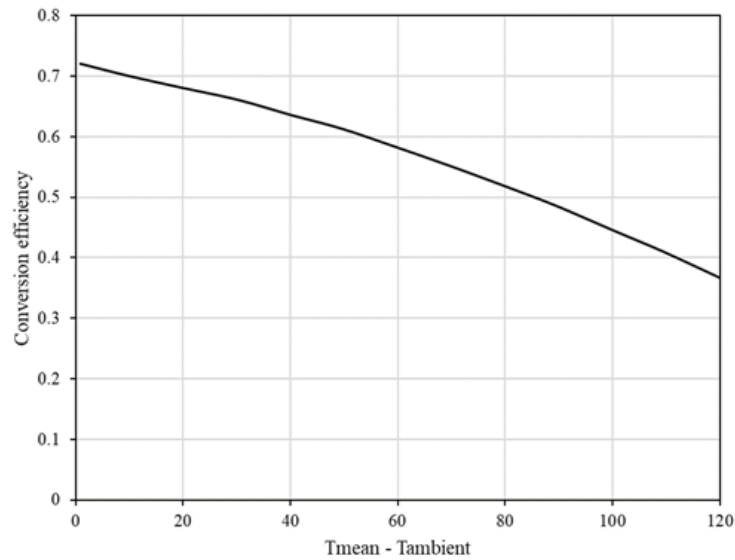


**Figure 5-7 Solar thermal collector efficiency for different HTF temperatures.**

The solar collector field should be able to provide enough energy to serve the building, as determined by Equation (5.21). In addition, the losses from the solar collector system and the

BTES system should be factored into the design. The piping network in a solar thermal collector system loses a significant quantity of heat energy to the environment. Similarly, only a portion of the energy stored in BTES may be retrieved. Some of it will be used to raise the ground temperature, while the rest will be lost to the surrounding rock mass and the environment via conduction, convection, and radiation. Considering these factors, the total energy to be injected into the BTES system is computed using Equation (5.22). Here,  $E_{actual}$  is the actual energy demand of the building and  $BTES_{ster}$  is the BTES injection to extraction ratio. Similarly, Equation (5.23) gives the energy to be generated from solar-collector systems. Here,  $HLF_{sur}$  is the heat loss factor to the surroundings from the solar-thermal collector system.

$$E_{BTES} = \frac{E_{actual}}{BTES_{ster}} \quad (5.22)$$

$$E_{sol} = \frac{E_{BTES}}{HLF_{sur}} \quad (5.23)$$

The type of solar thermal collector employed in this analysis is ETC-30 developed by Apricus Solar. The performance curve of the solar thermal collector is represented by Equation (5.24) [122]. Thermal performance depends on solar availability, ambient temperature, and the inlet temperature of the fluid. In Equation (5.24),  $T_{mean}$  and  $T_a$  represent the mean fluid temperature in the collector and ambient temperature, respectively, while  $G$  is the total solar irradiance at that instant.

$$\eta = 0.714 - 1.2430 \left( \frac{T_{mean} - T_a}{G} \right) - \left( \frac{(T_{mean} - T_a)^2}{G} \right) \quad (5.24)$$

The estimation of solar thermal field size is based on the energy output from a single collector. Based on energy output from a single collector, Equation (5.25) computes the total number of collectors needed for the system. Spacing between the collectors is accounted for in determining the solar field size. Equation (5.26) calculates the total field size needed for the solar thermal system. In Equations (5.25) and (5.26),  $N_c$  and  $A_{field}$  are the total number of collectors and the area of the field, respectively. Additionally,  $E_{pc}$  is the annual energy generation per collector and  $A_{c,g}$  is the gross area of the collector.

$$N_c = \frac{E_{sol}}{E_{pc}} \quad (5.25)$$

$$A_{field} = N_c \times A_{c,g} \times 1.15 \quad (5.26)$$

Based on these calculations, the solar collector field parameters obtained are presented in tabular form in Table 5-1.

**Table 5-1 Solar thermal collector system parameters.**

<b>S.N.</b>	<b>Item</b>	<b>Quantity</b>	<b>Unit</b>
1	Single collector area	4.4	m <sup>2</sup>
2	Average solar irradiation	321.9	kJ.m <sup>-2</sup> .hr <sup>-1</sup>
3	Single collector yield per year	2328	kWh
4	Total collectors needed	3032	m <sup>2</sup>
5	Total area needed for solar installation	15,370	m <sup>2</sup>

After incorporating the solar collector system, and building thermal demand into the reduced order BTES model, multiple simulations were performed to design a BTES system for the considered building.

#### 5.4.5 Economic analysis

The total cost of the heating system is divided into two categories: Capital Expenditure, referred to as CAPEX hereafter, and Cost of Energy referred to as COE hereafter. The size of a natural gas boiler is determined by the building's peak thermal demand. Based on total energy demand, the total amount of natural gas required is computed. Tables 5-2, 5-3, and 5-4 represent the CAPEX and COE breakdowns for a natural gas system, Solar thermal collector system, and BTES system, respectively. Engineering and design costs are assumed as 10% of the total cost.

**Table 5-2 Cost estimation for the natural gas heating system.**

S.N.	Item	Quantity	Rate (US \$)	Cost type
1	Boiler (Trane)	1	306 per kW	CAPEX
2	Engineering and design	-	10 % of boiler cost	
3	Tax	-	15 % of total	
4	Fuel cost	-	8.67 per GJ	COE

**Table 5-3 Cost estimation for Solar thermal collector system.**

<b>S.N.</b>	<b>Item</b>	<b>Quantity</b>	<b>Rate (US \$)</b>	<b>Cost type</b>
1	Evacuated tube collector set (including tubes, heat pipes, front tracks, bottom track, tube clips, and nuts) (Apricus-2021)	3032	1193 per unit	CAPEX
2	Pipe connectors	3032 × 2	12 per unit	
3	Installation of legs and fasteners	3032	89 per unit	
4	Engineering and design	-	10 % of total	
5	Tax	-	15 % of total	
6	Electricity cost		0.10 per kWh	COE

**Table 5-4 Cost estimation for BTES system.**

<b>S.N.</b>	<b>Item</b>	<b>Rate (US \$)</b>	<b>Cost type</b>
1	Drilling	50 per unit length	CAPEX
2	Coaxial pipe Installation	16 per u nit length	
3	Pipe cost	0.8 per unit length	
4	Pipe connectors	12 per borehole	
5	Thermal grout	10 per unit	
6	Insulation	0.4 per unit area	
7	Engineering and design	10 % of total	
8	Tax	15 % of total	
9	Electricity cost	0.10 per kWh	COE

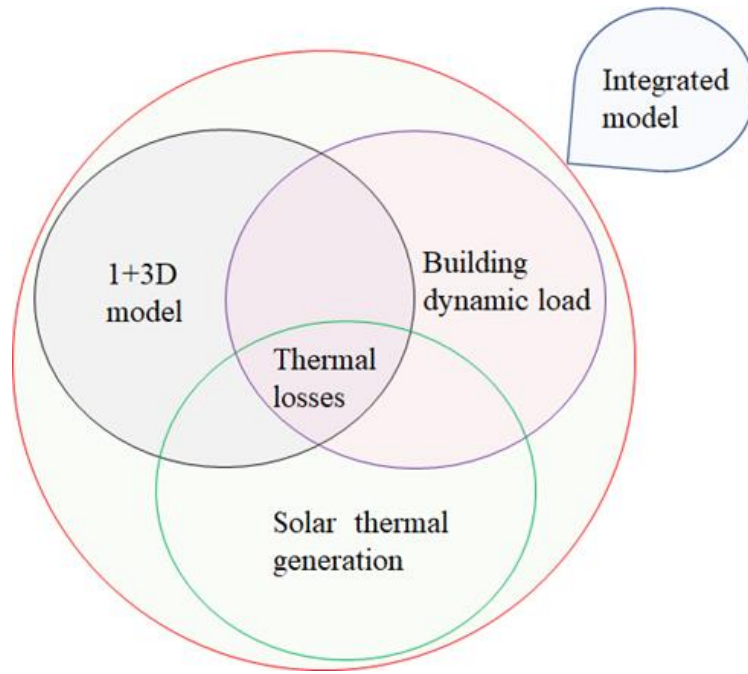
The simple payback period of the solar-geothermal system is calculated with reference to the natural gas heating system. To evaluate this, the following formula is used:

$$\text{Payback period} = \frac{\Delta CAPEX}{\Delta COE} \quad (5.27)$$

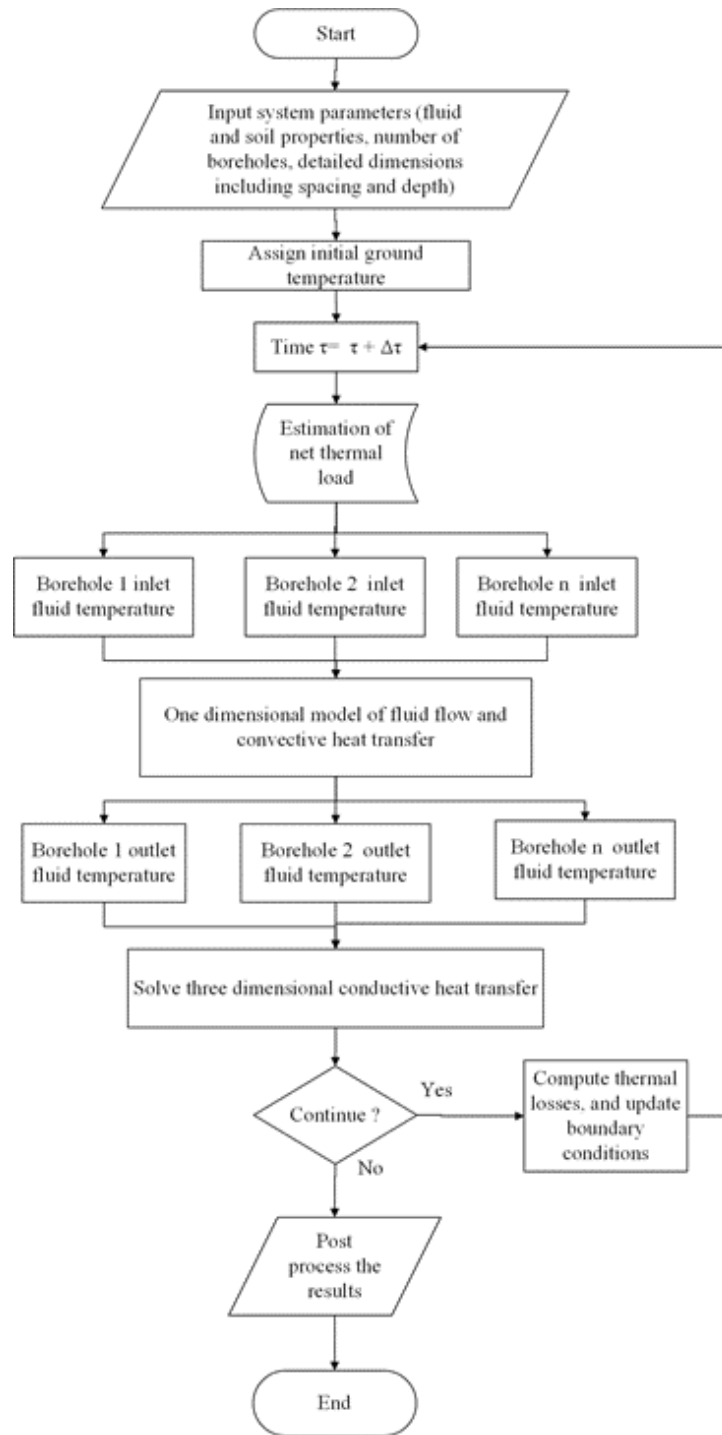
Here,  $\Delta CAPEX$  and  $\Delta COE$  are the capital cost difference and the operation cost difference between the proposed system and the natural gas heating system.

#### **5.4.6 Integrated model development**

After the 1+3D numerical model development, estimation of the building thermal demand, and design of the solar thermal collector system, the next step is to integrate these systems. A conceptual diagram of this integrated numerical model is shown in Figure 5-8(a) and the flowchart of the model is presented in Figure 5-8(b). Hourly thermal demand and thermal energy available from the solar collector system are computed at that instant of time and net thermal load is calculated. Net thermal load is the difference between the available solar thermal energy and building thermal demand at the instant of time. For positive net thermal load, available solar thermal energy is surplus compared to the building thermal demand resulting in the injection of thermal energy. Similarly, for negative thermal demand, solar thermal energy is less than the building thermal load resulting in the extraction of energy from the borehole system. Hence, the system operates continuously either in injection or extraction mode depending on the energy demand and supply.



(a)



(b)

Figure 5-8 Integrated numerical model (a) Conceptual diagram and (b) Flowchart.

For each time step, the inlet temperature of the boreholes is determined based on the injection or extraction cycle. It is equal to the outlet temperature of the solar thermal collectors during injection and the HTF temperature from the building during extraction. Similarly, the borehole outlet temperature is the collectors' inlet temperature during injection and the building inlet temperature during extraction. With the determination of the borehole inlet temperature, the heat transfer from boreholes to soil or vice versa is computed. This heat transfer to or from boreholes is solved in one dimension for all the source term elements in the Z-direction successively and thus the borehole outlet temperature is determined. After computing the borehole outlet temperature, the conductive heat transfer through the soil is computed for that time step. Two different discretized equations are solved for the conductive model; one for the source term elements and another for the non-source term elements as mentioned in Equations (5.8) and Equations (5.9), respectively. BTES thermal losses are computed, and boundary conditions are updated at each time step before moving to the next time step. Other operating characteristics of the proposed system are:

- i) For a base case scenario, HTF temperature change of 20°C during injection and 6°C during extraction is maintained by regulating the mass flow rate in the boreholes. Other options are also considered in the parametric analysis.
- ii) The solar-geothermal system starts to operate at the beginning of May.

#### **5.4.7 Grid independence test**

In this analysis, a grid independence study is performed to decide the mesh size for further simulations. Since the mesh generated is structured, both in the axial and radial directions, a grid independence test is performed. Figure 5-9 is the results of the grid independence study.

Time-step size of 3600s is used in the analysis and the outlet temperature after 124 hours (5 days) of flow time is measured to compare the results. In the axial direction, a temperature difference of less than 0.5% is obtained between the mesh sizes of 1 m and 2 m. Hence, the mesh size of 2 m in the axial direction is used in further analysis. Similarly, in the radial direction, a temperature difference of less than 0.5% is obtained between the mesh sizes of 0.22 m and 0.20 m. Hence the mesh size of 0.22 m in the radial direction is used in further analysis. The final mesh represents a total number of 17.6 million cells for a BTES domain with 450 boreholes each 100 m deep.

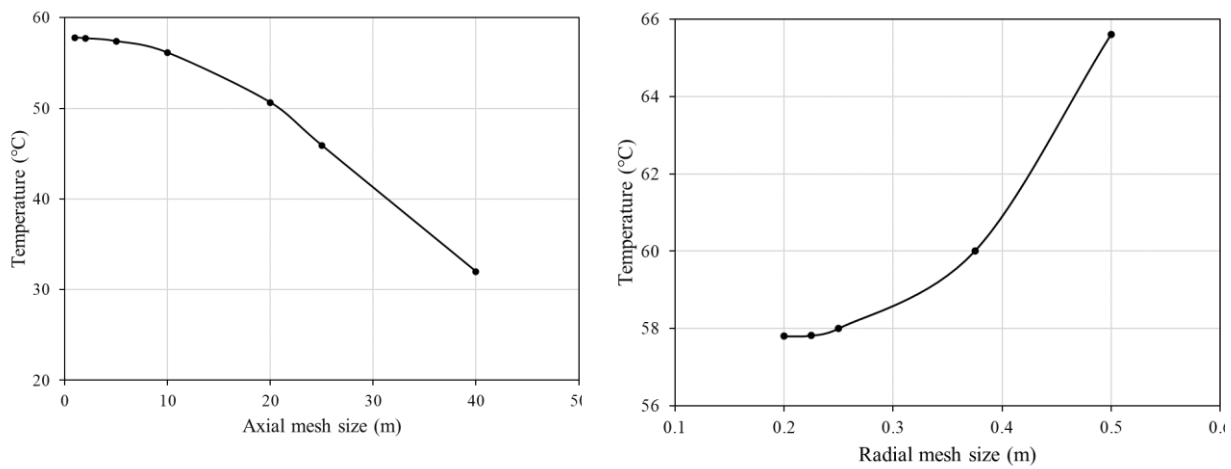


**Figure 5-9 Outlet temperature variation after 124 hours with different mesh sizes in the axial and radial directions.**

## 5.5 Model validation

### 5.5.1 Single borehole validation

The field-test experimental data from Morita et al. [50] for a co-axial borehole heat exchanger system are used to validate the developed numerical model. To do this, the 1+3D numerical code was simplified to a single borehole system. The exchanger dimensions and operating conditions

remain the same as in the experiments. Time-step size of 3600s is used for this analysis. Figure 5-10 displays the temporal evolution of the outlet temperature. For identical initial and operating conditions, there is a strong correlation between the numerical and experimental results, demonstrating the validity of the numerical code.

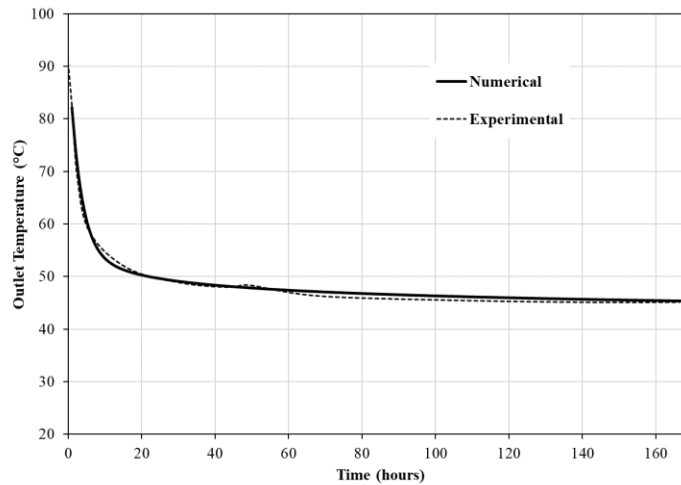


**Figure 5-10 Temporal evolution of the outlet temperature for a single borehole. Comparison between the present numerical result and field test experimental data from Morita et al.**

### **5.5.2 Multiple boreholes validation**

Additionally, the numerical model is validated for sixteen boreholes with a commercially accessible finite volume solver, ANSYS Fluent. For validation, a  $4 \times 4$  rectangle drilling field with 100 m depth is simulated using ANSYS Fluent and a 1+3D numerical model. Time-step size of 3600s is used for both simulation models. The inlet condition is the time-varying inlet temperature and flow rate in each borehole. The outlet temperature of each borehole in different cases is recorded. The average temperature of the HTF output from the boreholes is presented in Figure 5-11. A maximum error of less than 2 percent is observed compared to the Fluent model, which supports the validity of the 1+3D numerical model with several boreholes.

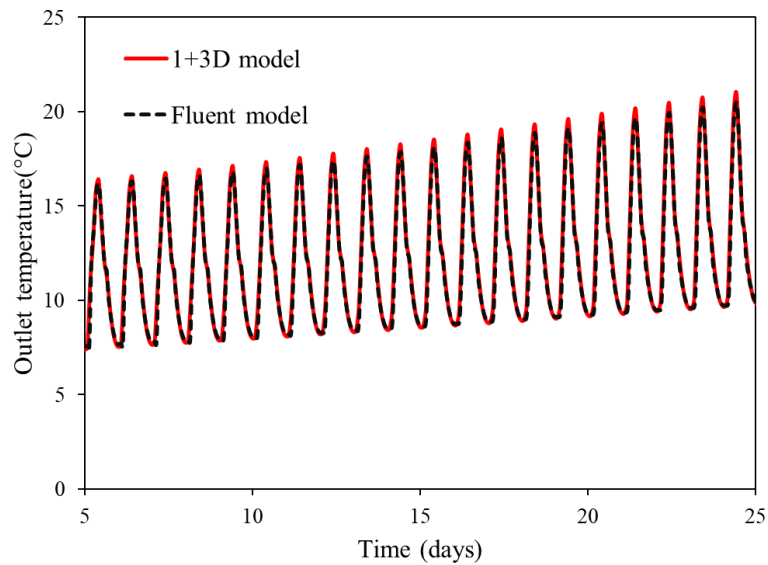


**Figure 5-11 Temporal evolution of the outlet temperature for multiple boreholes. Comparison between the developed 1+3D numerical code and results from ANSYS Fluent.**

## 5.6 Computational cost

The computational cost of the developed 1+3D model is compared with the commercially available software, ANSYS Fluent, in this analysis. For both platforms, a  $4 \times 4$  computational domain consisting of 16 boreholes is simulated. Even though the total domain volume is the same, the number of elements varies due to the various meshing strategies. While the Fluent model has a varied mesh density at various distances from the boreholes, the 1+3D approach has a uniform mesh throughout all domains. The model created in Fluent has a total mesh count of 1,274,112 while the model created in 1+3D has a total mesh count of 615,040. This is slightly more than a factor of two. The computational time to solve the same physical phenomena varies due to the mesh count and numerical methodology differences between the two solvers. Both simulations are done on the same machine for comparative purposes. The 1+3D solver is 194 times faster than the

Fluent in terms of computational performance. To illustrate more, for a typical solar-geothermal size of 100 boreholes, it took about 102 hours for the 1+3D code to simulate five years of flow time. However, it would take more than 19,750 hours with Fluent, which is impractical. Moreover, meshing 100 boreholes in a single domain is very complicated for a commercial solver if not impossible.

## **5.7 Results**

The simulation is run for five years of operation time. Time-step size of 3600s is used for obtaining all the results. It is noticed that in the solar-geothermal system after five years of continuous operation, the system acquired a stable state.

### **5.7.1 Base case scenario**

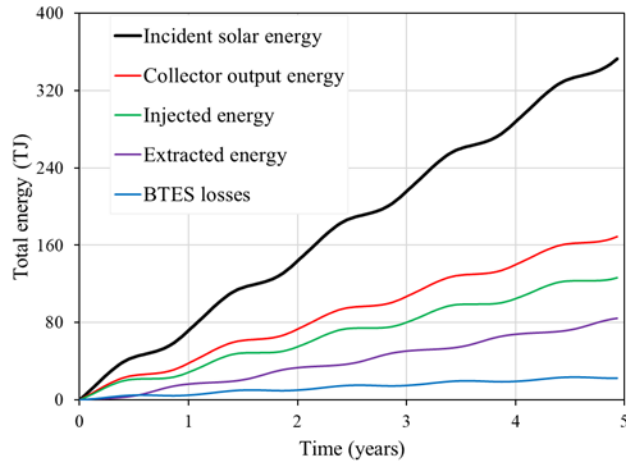
Figure 5-12 illustrates the results of a base case scenario. The base-case scenario entails 450 boreholes, spaced 3m apart and 100 m deep. Additionally, there are 3032 collectors, each measuring 4.4 square meters. The total number of control volumes for the base case scenario is 17.6 million.

Figure 5-12(a) quantifies the energy generated, stored, extracted, and lost from the solar-geothermal system for the base case scenario. As seen from Figure 5-12(a), out of 356 TJ of incident solar thermal energy over five years, only 169 TJ of thermal energy is converted to usable thermal energy. This thermal energy is divided into three categories: supplied to BTES, delivered to the building, and lost to the ambient via piping networks. Not all the energy supplied to the BTES system is recovered; some of it is utilized to raise the temperature of the ground, and some of it is lost owing to thermal losses, including conductive, convective, and radiative losses.

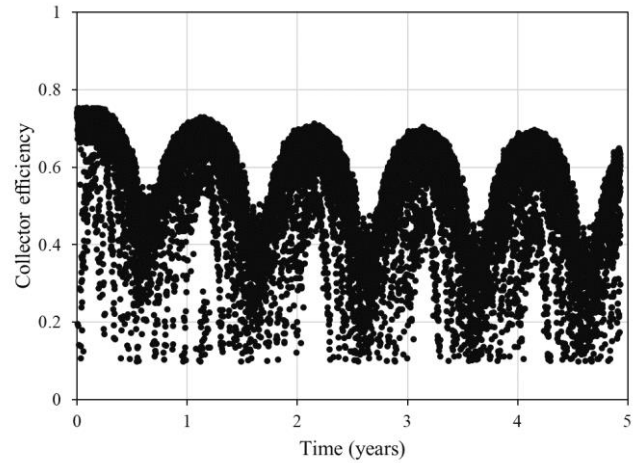
Although incident solar energy is constant, all other values could fluctuate depending on the design and operational conditions, which are discussed later in this study.

Another major element to consider is presented in Figure 5-12(b), which displays the hourly scatter plot of solar thermal collectors' efficiency over time. It is seen that the average solar thermal collector efficiency gradually declines over time. This is because, in a solar-geothermal system, HTF from boreholes is relayed to solar thermal collectors. In other words, the fluid entering the solar collectors is the fluid leaving the BTES. The borehole outlet temperature increases with time as the average ground temperature rises. The efficiency of the solar thermal collectors is inversely proportional to the fluid inlet temperature, due to which the efficiency decreases. The average thermal efficiency of collectors over five years period is 0.55. But for the first and fifth years of operation, the average thermal efficiency is 0.62 and 0.51 respectively.

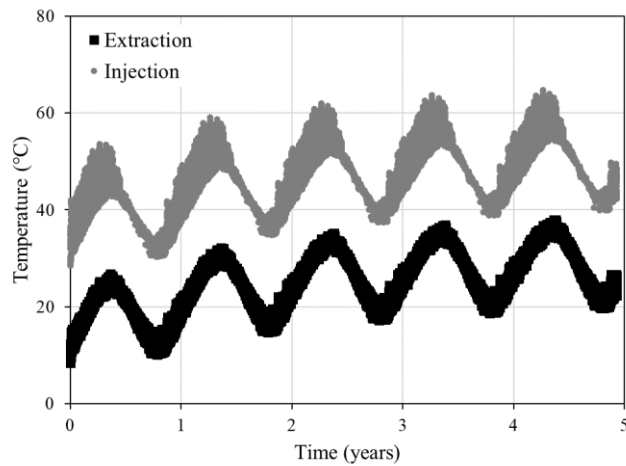
Additional major parameters are the HTF inlet and outlet temperatures from the boreholes and the average ground temperature. These two parameters are presented in Figure 5-12(c) and Figure 5-12(d), respectively. Figure 5-12(c) displays the BTES inlet and outlet temperatures at a specific point in time during injection and extraction, respectively, and therefore has a discrete distribution. It is crucial to monitor the BTES inlet temperature during the injection cycle because it is also the collector outlet temperature. Similarly, the BTES outlet temperature during the extraction cycle is important as it is also the inlet temperature of the fluid on the building site. The BTES outlet temperature during the extraction cycle is also responsible for the Coefficient of Performance -



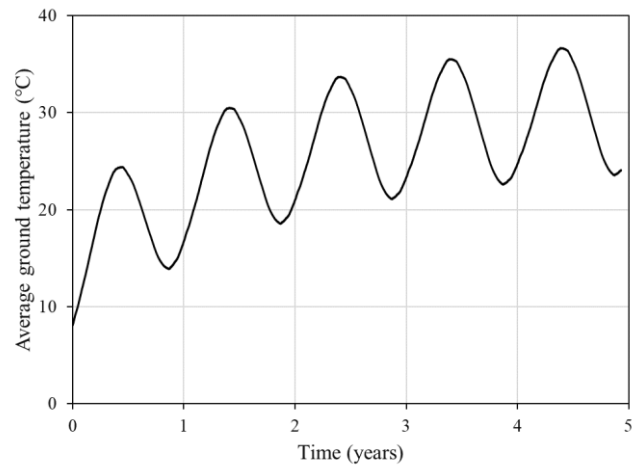
(a)



(b)



(c)



(d)

**Figure 5-12 Temporal evolutions of the (a) Cumulative total energy, (b) Solar thermal collector efficiency with time, (c) BTES injection inlet temperature and extraction outlet temperature, and (d) Average ground temperature. Results obtained by the 1+3D numerical model.**

(COP) of the heat pumps on the building side. The higher the average ground temperature, the higher the COP, and vice versa. For the base case scenario, after 5 years of operation, the average peak ground temperature during summer reaches 36.6°C while the lowest peak temperature during

winter decreases to 23.0°C. Also, the peak fluid temperature inlet to the BTES is 64.7°C in summer while the lowest fluid temperature outlet from BTES during winter is 19.7°C.

### **5.7.2 Parametric analysis**

In this section, results are recorded for different designs and operating conditions of the solar-geothermal System. Adjustments in the boreholes' center-to-center (c-c) distance and depth are examples of design variability. The change in temperature of the HTF in the solar collector is analyzed as an operating condition. This objective can be achieved by changing the mass flow rate in the solar collector system. The design conditions, including the borehole length, remain constant while analyzing different operating conditions, whereas the operating parameters are fixed when analyzing different design conditions. While the financial ramifications of modifying the design and operational conditions are not thoroughly examined, the technical outcomes of the parametric analysis are.

#### **5.7.2.1 Effect of depth variation**

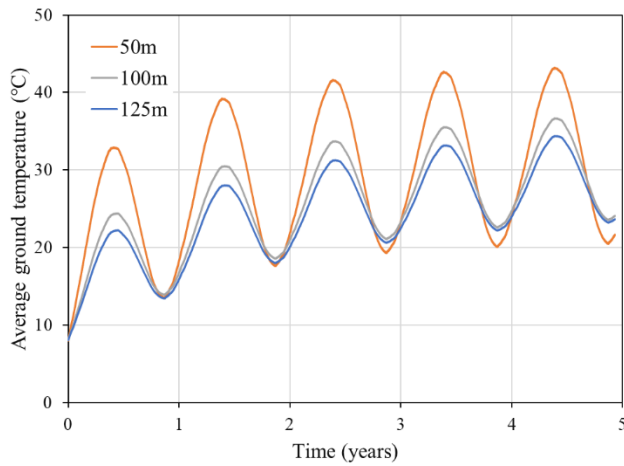
In this parametric study, the borehole depth is modified but all other solar-geothermal parameters are left unchanged. Deeper boreholes result in a reduced power per unit length of the borehole at both the injection and extraction cycles. The consequences of changing the borehole depth from 50 to 125 meters are examined. The outcomes of this parametric analysis are shown in Figure 5-13.

The total mass and volume of the BTES alter with the borehole depth thanks to higher BTES average temperature for shallower depths. For borehole depths of 50, 100, and 125 meters, the average BTES temperatures over five years are 29.0°C, 25.5°C, and 24.2°C, respectively.

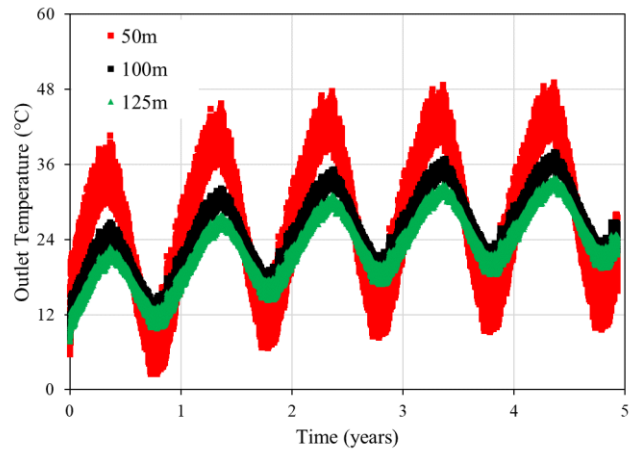
Shallower depth boreholes have greater average ground temperatures over five years, but in the winter, these have lower average temperatures. This may be seen following the third cycle of the solar-geothermal system as presented in Figure 5-13(a). Figure 5-13(a) also provides more detailed temperature variation over a five-year operational period. It is determined that shorter depths have lower heat capacities than deeper ones, which causes these systems to gain or lose energy more quickly than deeper boreholes. Additionally, it may be deduced that shallower depth boreholes have greater fluctuations in borehole outlet temperature than deeper boreholes.

For shallower boreholes, higher fluid temperatures are attained in summer, but this comes at the cost of a lower temperature during winter months. This is also evident from the borehole outlet temperature distribution as portrayed in Figure 5-13(b). For boreholes of 50 m depth, winter borehole outlet temperatures are almost 10°C less than that of 125 m boreholes. Not only are the BTES outlet and average temperatures higher in deeper boreholes but also the gross solar energy produced by the solar thermal collectors. This is expressed quantitatively in Figure 5-13(c). For five years, the total solar yield increased from 152.1 TJ to 173.7 TJ as the depth increased from 50 m to 125 m. It represents a 14% increase in solar thermal energy production. This is because solar yield predominantly depends on two variables: solar irradiation and HTF inlet temperature to solar collectors. The HTF entrance temperature to the collectors varies depending on the scenario, even if the solar irradiation remains the same in all of them. Since the boreholes and solar thermal collectors are connected directly, the thermal collectors' intake is the borehole outflow.

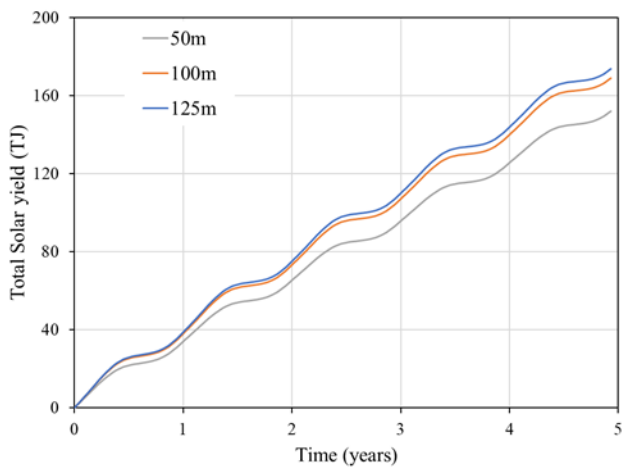
The thermal losses from the BTES system are another crucial factor. Conduction, convection, and radiation losses are all types of thermal losses. According to simulation results, conduction is seen to be the main mode of BTES thermal losses, followed by convection and radiation. According to Figure 5-13(d), fewer losses are noted in the analysis because shorter boreholes have less surface



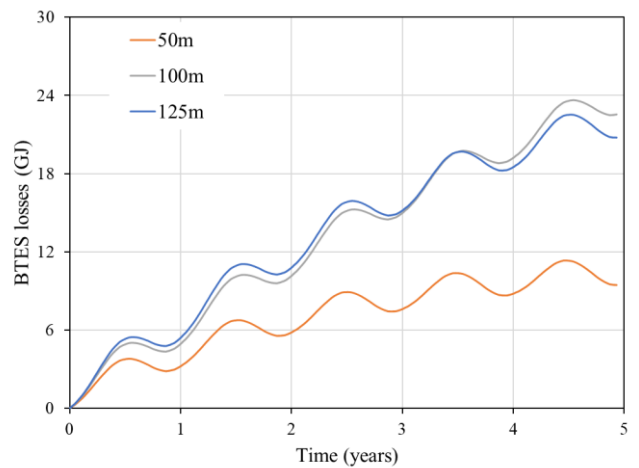
(a)



(b)



(c)



(d)

**Figure 5-13 Temporal evolutions of the (a) Average BTES temperature, (b) Borehole outlet temperature during extraction, (c) Total solar yield from solar thermal collector system, and (d) BTES thermal losses.**

**Results obtained by the 1+3D numerical model.**

area of exposure to the surrounding rock mass. From 11.3 TJ of losses in the 50 m borehole system, the total thermal losses for the 125 m borehole system grow to 22.5 TJ. The winter months are

more important for providing heat to the buildings. As a result, deeper boreholes are preferred over shallower ones.

#### **5.7.2.2 Effect of center-center distance variation**

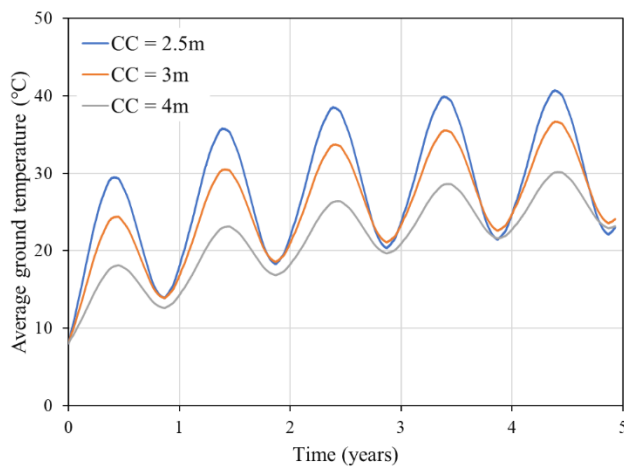
Here, the center-center (c-c) distance of boreholes is varied to examine any effects on the operation of the solar-geothermal System. All other factors, such as the borehole depth, the size of the solar collector field, and the operating circumstances, were left unchanged for this investigation. In this parametric analysis, the c-c distance can range from 2.5 to 4.0 meters.

The expected impact of c-c variation is the BTES average temperature. The total mass and volume of the BTES system are directly proportional to the c-c distance of boreholes. The average temperature of a BTES system decreases as c-c increases due to the larger volume of the system, as shown in Figure 5-14(a). Even though shorter c-c distances can attain greater BTES average temperatures, particularly in winter when thermal demand is highest, the average ground temperature once the system reaches a steady state is almost similar for longer and shorter c-c distances. The wintertime average ground temperature after five years of operation for the 4.0 m c-c distance BTES system is marginally greater than that for the 2.5m c-c distance. This is also evident in Figure 5-14(b), which shows the temperature of the HTF exit from the boreholes during the extraction cycle. For a c-c distance of 3.0 m compared to 2.5 m, the outlet temperature is higher in the winter. The shorter c-c BTES system can be interpreted to not only gain temperature quickly but also lose heat quickly, resulting in a smaller heat capacity.

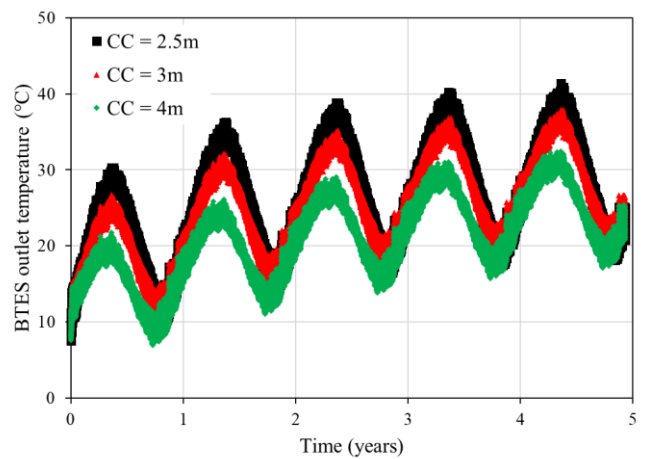
The solar yield is a crucial factor to consider when comparing changes in c-c distance. The cumulative solar yield for various c-c borehole configurations is shown in Figure 5-14(c). The solar yield is the highest at the maximum c-c distance and least at the minimized c-c distance. The

solar yield increases by 7% when the c-c distance is expanded from 2.5 to 4.0 meters. For the same reason, the average solar thermal efficiency increases from 55% to 60%. The system can supply solar thermal energy for 18,876 hours out of 43,800 hours throughout the five years of operation. However, for a c-c distance of 2.5 meters, this number lowers to 17,941 hours. This is driven by a rise in the HTF input temperature in solar thermal collectors for a c-c distance of 2.5 meters as opposed to 4.0 meters.

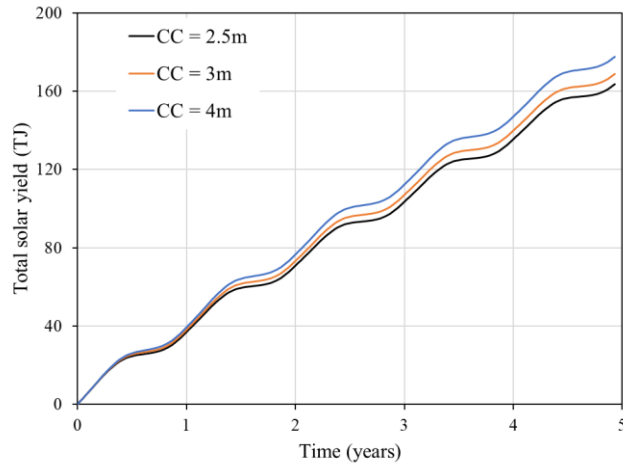
Thermal losses from the system should also be considered. The average temperature of the BTES system is higher at shorter c-c distances leading to higher thermal losses. The thermal losses from larger c-c BTES systems are lowest for the same reason, as shown in Figure 5-14(d).



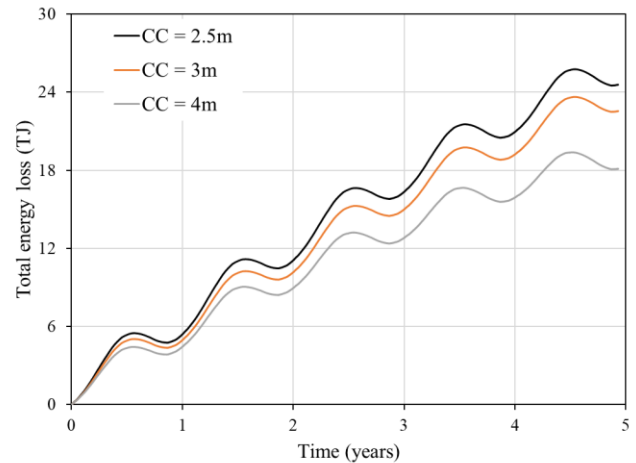
(a)



(b)



(c)



(d)

**Figure 5-14** Temporal evolutions of the (a) Average BTES temperature, (b) Borehole outlet temperature during extraction, (c) Total solar yield from solar thermal collector system, and (d) BTES thermal losses. Results obtained by the 1+3D numerical model for 3 values of the center-center distance between 2 boreholes.

### 5.7.2.3 Effect of delta temperature ( $\Delta T$ ) variation

In this study, the operational parameter is altered compared to the design parameters in the previous section. The parameter under study is the HTF temperature change in the solar thermal collectors. Fixed temperature gain in solar thermal collectors is accomplished by adjusting the mass flow rate in the collectors. A constant  $6^{\circ}\text{C}$  change during extraction and a constant  $20^{\circ}\text{C}$  change during injection was assumed in previous studies. Here, the effect of temperature gain change in solar thermal collectors during injection is studied. This temperature gain is varied from  $16^{\circ}\text{C}$  to  $31^{\circ}\text{C}$ . Figure 5-15 represents the results of the two extreme occurrences of this variance. A discernible difference is seen for the BTES inlet temperature or solar collector outlet temperature as the temperature change in solar collectors increases as presented in Figure 5-15(a). During injection, the temperature at the collector outlet or BTES inlet rose by around  $10^{\circ}\text{C}$ . Also, from Figure 5-

15(b), small variations are observed in the BTES outlet temperature during the extraction cycle. The outlet temperature from the boreholes is slightly higher for  $\Delta T$  of  $31^{\circ}\text{C}$  than for  $\Delta T$  of  $16^{\circ}\text{C}$ , which is also better in terms of BTES performance because the higher temperature is achieved during the extraction phase and supplied to the building, resulting in better COP of heat pumps in the winter and consuming less energy.

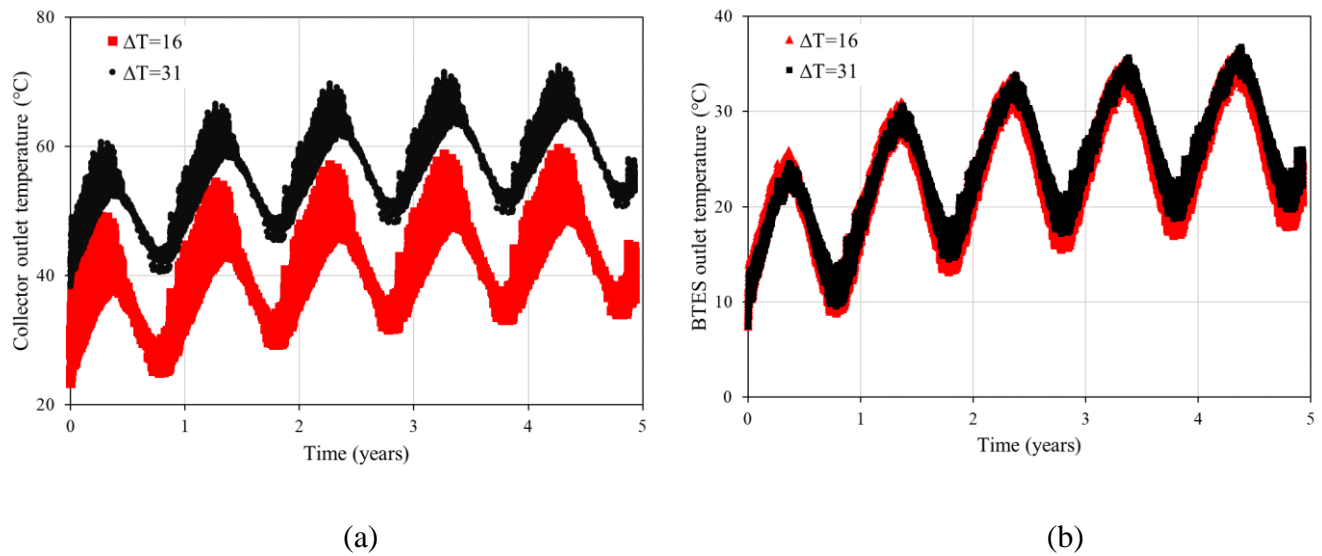


**Figure 5-15** Temporal evolutions of the (a) Collector outlet temperature and (b) BTES outlet temperature during the extraction cycle. Results obtained by the 1+3D numerical model for 2 values of the temperature change during the injection phase.

The change in mass flow rate in the solar collectors and heat exchangers during the injection cycle is another aspect of  $\Delta T$  that should be mentioned. A smaller mass flowrate is required to raise the temperature by  $31^{\circ}\text{C}$  as opposed to  $16^{\circ}\text{C}$ , which results in a lower pumping cost for the HTF. HTF overall average flow rate reduces from  $34.7 \text{ kg/s}$  to  $28.8 \text{ kg/s}$ , a decrease of more than 20 % when  $\Delta T$  is raised from  $16^{\circ}\text{C}$  to  $31^{\circ}\text{C}$ . Hence, a larger temperature rise in solar thermal collectors is

suggested for better performance. It is also worth mentioning that no noticeable difference is observed in solar thermal collector yield and efficiency by just changing this operating condition.

## **5.8 Economic and environmental analysis**

### **5.8.1 Capital expenditure (CAPEX)**

Figure 5-16 represents the capital costs waterfall chart for both of the analyzed scenarios. Capital costs of the solar-geothermal system are higher accounting for US\$ 9.2 million while the total capital cost is US\$ 0.3 million for the natural gas system. The capital costs of the BTES system are slightly higher than that of the solar thermal collector system. The rated peak power output of the designed solar thermal collector system is 6.1 MW, and with this data capital costs per unit of power are calculated at US\$ 700/kW. The total amount of thermal energy to be stored in the BTES system is 20.2 TJ and US\$ 4.9 million is the capital cost for its construction. Hence, capital costs per kWh of energy storage are under US\$ 1. For the sake of comparison, the corresponding energy storage cost for lithium-ion battery storage technology is in the range of US\$ 350 – 400 [123]. Hence, for seasonal energy storage applications, the BTES system is quite superior to battery storage technology. Capital costs for a natural gas heating system are very low, as it only requires the boiler and accessories with some engineering work. No energy storage technology is needed for this system as energy can be directly fed to the buildings.

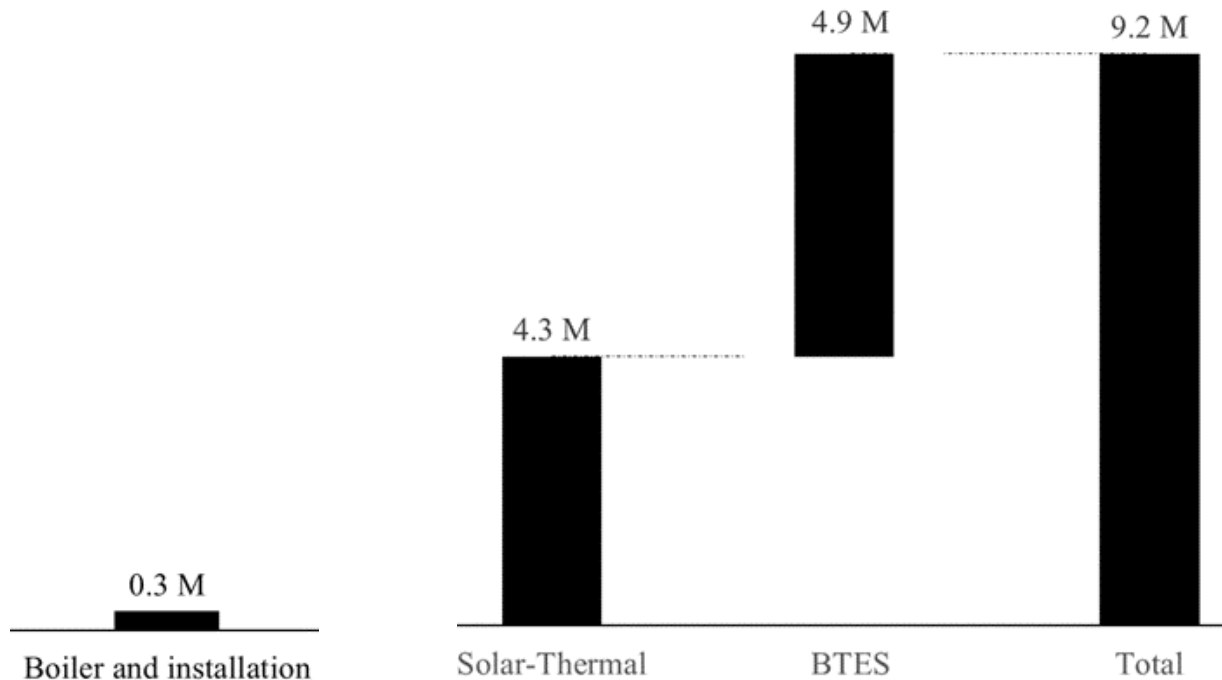


**Figure 5-16 Capital costs in US \$ of (left) Natural gas heating system, (right) solar-geothermal system.**

### 5.8.2 Cost of energy (COE)

COE is an important parameter and may decide the economic feasibility of the system. Figure 5-17 shows the COE to operate two systems. The energy cost of natural gas heating systems is attributed to the cost of natural gas needed to burn to supply the heating demand of the buildings. The energy cost of a solar-geothermal system is attributed to the pumping cost in solar thermal collectors and the BTES system which is supplied with electricity. The unit cost of electricity is currently 3.4 times greater than the unit cost of natural gas in Ontario, Canada. The energy cost for the natural gas system is higher in the winter months, whereas the energy cost of solar-geothermal is the opposite. While it is common to have greater energy costs in the winter months due to higher thermal load demand, this is not always the case. In the case of solar-geothermal, the summer months are the injection period, and these months have higher solar irradiation. This creates a

higher flow rate in the boreholes than in the winter months. Therefore, COE is higher in the summer months for the solar-geothermal system. The COE of the solar-geothermal system is lower. This cost is around 20% of the COE of the natural gas heating system. The solar-geothermal system also operates the majority of the time of the year and the maximum flow rate in the solar collector distribution network is  $20 \text{ kg s}^{-1}$ . Despite the longer operation time, static head lift in this system is lower. Because the entrance and exit of boreholes are both in equilibrium with atmospheric pressure, the energy required is just to counteract the friction loss in the pipes. The total annual energy cost of the natural gas system is US \$ 203K, while solar-geothermal system energy costs are US \$ 42K. Figure 5-17 is based on the current rates of electricity and natural gas for the studied location.

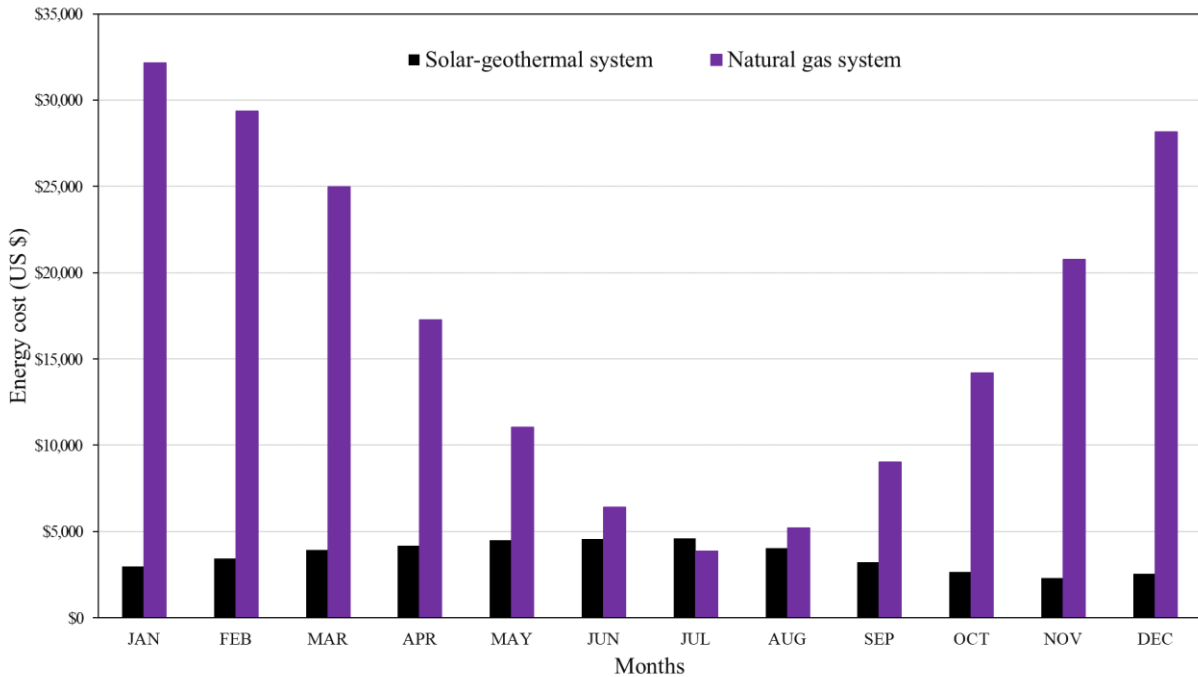


**Figure 5-17 COE comparison for two systems.**

### 5.8.3 Cost savings and global perspective

This section includes the results of annual energy cost savings achieved by replacing the conventional system with the proposed system. The natural gas heating system is used as a baseline to compare the alternative. The solar-geothermal system requires electricity to function. However, the unit cost of natural gas and electricity varies by region. These costs are also subject to change over time. In Canada, for example, starting in 2023, the government will raise the benchmark price by CA \$ 15 per tonne of carbon per year, eventually reaching CA \$ 170 per tonne of carbon pollution in 2030 [124]. As a result, a contour map of annual cost savings is shown to provide a global perspective of the system efficacy. Figure 5-18 shows yearly cost reductions for a variety of situations. The unit cost of energy from natural gas and electricity is changed between US ¢3 and US ¢21 per kWh, and the results are reported. As shown in Figure 5-18, a solar-geothermal system is more suited for locations where the unit cost of natural gas is higher compared to the cost of electricity. The region with the lowest yearly cost savings is dark blue, which is not the desired outcome for the suggested solution. In the investigated range, yearly cost savings for the solar-geothermal system are always positive, regardless of natural gas or electricity costs. Even under the worst-case scenario, the solar-geothermal combination saves at least US\$ 138 K per year.

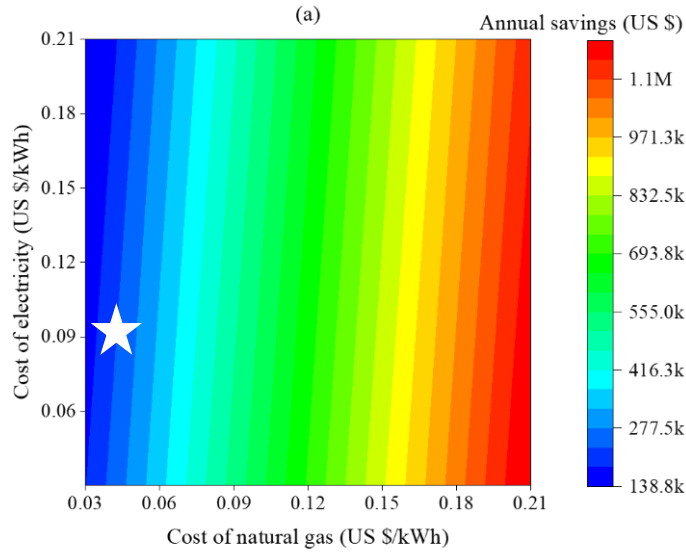


**Figure 5-18 Annual cost savings for the solar-geothermal system (the star sign denotes the current energy rates).**

#### 5.8.4 Payback period

The payback period is an important parameter in the project feasibility in addition to the energy cost savings. A simple payback period is calculated in this analysis. The payback period is determined for two possible scenarios. To begin, the payback period is determined using the CAPEX referenced in Section 5.6.1. Another payback period is calculated based on the premise that the CAPEX varies from the base case scenario due to price structure uncertainty. CAPEX for the solar-geothermal system has been increased by 15% over the original estimate. Because the solar-geothermal system adopts a set of design and infrastructural criteria, cost estimates are unlikely to alter dramatically. As a result, only 15% increase in CAPEX is considered. With this assumption, the power cost of the solar-geothermal system ranges between US\$ 700 and US\$ 805 per kW. The payback periods for various CAPEX scenarios are shown in Figure 5-19 and Figure 5-20. Furthermore, these images consider potential changes in electricity and natural gas prices. In

both figures, a payback period of more than 50 years is deemed financially unviable and is highlighted in dark red. According to the findings, the lower cost of electricity and higher cost of natural gas have the lowest payback period.

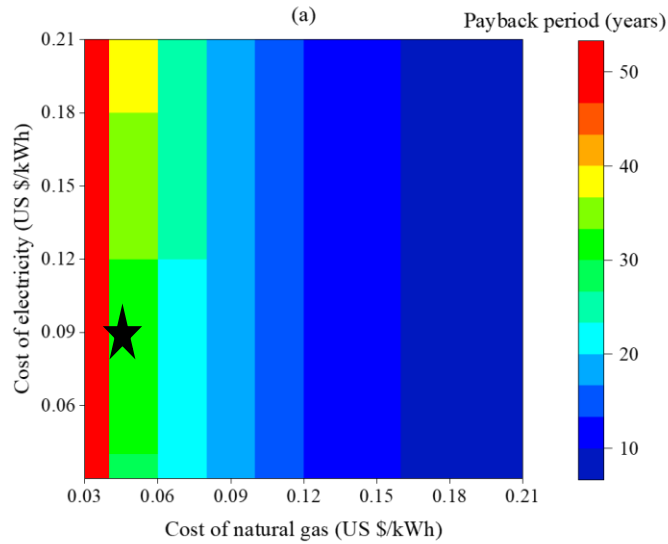


**Figure 5-19. The payback period for capital costs of US\$ 700/kW of installed capacity (the star sign denotes the current energy rates).**

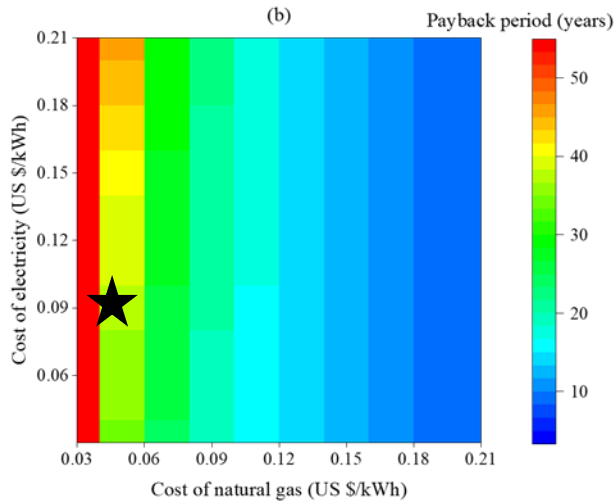


**Figure 5-20 Payback period for capital costs of US\$ 805/kW of installed capacity (the star sign denotes the current energy rates).**

## 5.9 Conclusions

This research developed a computationally efficient and integrated numerical model to solve thermal generation, storage, extraction, and losses from a solar-geothermal system. The type of heat exchanger considered is a co-axial borehole heat exchanger. One-dimensional fluid flow and convective heat transfer in the borehole are solved in conjunction with the three-dimensional conduction process in the surrounding strata. Hourly fluctuations in building thermal energy demand and solar thermal collectors' generation are accounted for. Validation of the BTES numerical model is performed against the field-test experimental data for a single borehole and against a commercially available Finite Volume solver for multiple boreholes. In addition, it also presented the financial implications of replacing conventional energy sources in building heating with a solar-geothermal system. System-level design analysis was undertaken and technical feasibility was assessed with state-of-the-art technology. Capital cost, energy savings, and payback period were quantified for the proposed system based on variable electricity and natural gas costs. It is concluded that the developed BTES numerical model can solve the heat transfer process in BTES 194 times faster than the commercially available solver. Overall, in any location that is being considered, with known soil properties and solar availability, one can design a solar-geothermal system using the proposed numerical code. From the results, it is also concluded that the building with 826 residential units may be entirely heated by 3032 solar thermal collectors, each having a surface area of  $4.4 \text{ m}^2$ . Better solar-geothermal performance is achieved with deeper boreholes, however, the rate of performance increase declines for boreholes deeper than 100 m due to low-temperature gain. Another important consideration when building a solar-geothermal system is the Centre-Centre distance between the boreholes. In comparison to greater distances, where BTES temperature gain is gradual and unsatisfactory, smaller distances exhibit swift

temperature gain and loss. The performance of the BTES is slightly improved by higher temperature change in solar thermal collectors with lower mass flowrate compared to lower temperature change with higher mass flowrate. Thermal conduction is the major source of heat losses from the BTES system followed by convection and radiation, respectively.

The financial analysis determined that implementing the solar-geothermal system for the studied building size requires a total capital cost of US\$ 9.2 million. By adopting this system, at current energy rates, significant energy cost savings of about US\$ 300,000 or more, attributed to reduced natural gas expenses, can be achieved. The payback period is mainly contingent on the electricity and natural gas rates at the specific location under study. At the current location and prevailing rates, the estimated payback period is 30 years. However, even a slight increase in natural gas costs would lead to a considerable decrease in the payback period.

## **Chapter 6: Discussion of Findings**

### **Preface**

Within these pages, we summarize the work accomplished and the major findings. Furthermore, we aim to highlight the contribution that this research has made to the wider scientific community. Subsequently, we also address the limitations of our current work, paving the way for promising future directions.

### **6.1 Overview of research problems**

Geothermal energy is a significant source of clean energy that can provide a stable base load capacity and be utilized for both heat and power, depending on user needs. Although the scientific community has recently recognized the importance of this energy system and many start-ups have emerged as a result, it still faces several issues that demand further fundamental and applied knowledge.

In particular, deep comprehension of geothermal heating and power systems necessitates robust numerical and thermodynamic modeling. Accurately modeling such systems and predicting their performance is challenging due to various factors, such as the non-uniform lithosphere, the presence of fluid and its movement, and its impact on geothermal system performance. The literature lacks both sufficient availability of field-scale experimental results obtained using state-of-the-art technology and detailed numerical modeling of heat transfer and fluid flow in both the heat exchanger and the formation.

Moreover, large-scale solar-geothermal heating systems without the presence of porous and permeable rocks, where the heat transfer process is purely conductive, may consist of hundreds of boreholes. Numerically modeling such systems and estimating their performance is equally challenging due to the extensive computational domain and the challenge of incorporating thermal interference between boreholes. Additionally, the literature lacks a comprehensive tool to understand the overall system performance, including the thermal energy sources such as solar collectors, and sinks, which are often large-scale buildings or clusters of distributed homes in the neighborhood.

## **6.2 Major findings**

This thesis is divided into three major chapters to address the three research problems included above.

Firstly, we conduct an analysis of the field-test results performed on a 500 m deep coaxial borehole heat exchanger, situated in a high-temperature gradient porous and permeable volcanic rock formation. The results of the field-test analysis contribute new experimental data to the existing literature, generated using state-of-the-art technology. Specifically, the extraction-recovery temperature profile of the subsurface will assist engineers in designing future experiments on geothermal systems, as these curves are key parameters for understanding the behavior of the geothermal reservoir. Furthermore, a lab test was conducted to measure the physical, thermal, and hydraulic properties of the rock samples, contributing to a better understanding. The study revealed that the rock properties varied at different depths of the reservoir, which influenced the extraction and recovery temperature profiles of the geothermal reservoir. Given the significance of these

curves in the existing literature, a detailed 3D numerical model was developed to replicate this field test experiment.

The developed numerical model is a 3D replication of the experimental setup capable of solving the conjugate heat transfer and fluid flow mechanisms in the heat exchanger and the porous and permeable rock layers. By utilizing the in-situ temperature distribution profile and the measured rock properties from the lab, the developed numerical model successfully replicated the field-test experiment and calibrated the seepage characteristics of the subsurface reservoir. Using this validated model, additional simulations were conducted to predict the thermal power and energy output from the system under various design and operating conditions. The study concluded that the total thermal energy output from the system over 30 years would range between 141.5 TJ to 113.3 TJ, considering different operation parameters. In addition, the numerical model also predicted the effect of seepage on the thermal power output from the system over the project operation, and it was observed that the total energy output would increase by over 19.5% due to the presence of seepage with calibrated velocity.

The final chapter of this thesis focused on developing a reduced-order model to solve the fluid flow and heat transfer processes in a pure conductive rock with multiple boreholes. The system of boreholes was employed in a solar-geothermal heating system, aimed at storing thermal energy during the summer months and providing heating for a large building with 826 apartments during dark and cold winter periods. The developed model was validated using experimental data for a single borehole and compared with a commercial solver for multiple boreholes. Results showed that the developed model achieved a 194-times faster solution for the fluid flow and heat transfer analysis in the borehole system, while also simulating all other components of the solar-geothermal system. Using the validated numerical toolkit, a solar-geothermal system was designed for the

considered building size. It was concluded that 450 boreholes, each with a depth of 100 m, in combination with 3032 solar collectors of 4.4 m<sup>2</sup> area each, were sufficient to meet the uninterrupted thermal demand for the building in the given location. Moreover, it was determined that the payback period of the project is influenced by the energy rates of the location. With the current energy rates for natural gas and electricity at the considered location, the investment of US\$ 9.2 million in the project would take approximately 30 years to pay back.

### 6.3 Contribution to knowledge

This thesis contributes to both fundamental and applied knowledge in the existing literature on geothermal heat and power systems using coaxial borehole heat exchangers. Specifically, the following contributions to geothermal power systems are made from the current research project.

- **Fundamental:** Presented a set of extraction-recovery curves and outlet temperature curves for geothermal exploration, which will serve as a foundation for further exploration of similar geothermal sites.
- **Fundamental:** Developed a numerical model to simulate the complex subsurface physical phenomena, utilizing all measured and obtained reservoir details and characteristics. The model is capable of estimating the performance of the borehole heat exchange system not only for extraction, but also for recovery.
- **Fundamental:** Calibrated the seepage velocity in the geothermal reservoir using the generated experimental dataset and the developed numerical model. Additionally, evaluated the performance enhancement of the geothermal reservoir with and without the presence of seepage.

- **Applied:** The design and operating characteristics of the borehole have a significant impact on the performance of the geothermal system. Varying the flow rate or the fluid inlet temperature may be identified as crucial parameters that determine the quality of thermal energy extracted from the system.
- **Applied:** Understanding the seepage velocity and flow in the reservoir can aid in identifying the porous and permeable layers, which may be targeted for directional drilling to enhance the thermal yield from the geothermal system.

As for the solar-geothermal heating system with a system of coaxial boreholes, the following contributions are made:

- **Fundamental:** A Reduced Order Numerical (ROM) model is developed to solve the heat and mass transfer processes in a system of boreholes used in a large-scale solar-geothermal heating system with co-axial borehole heat exchangers. The developed model has a superior computational performance compared to commercial solvers and provides a better understanding of the heat transfer characteristics in the borehole system and its thermal losses.
- **Fundamental:** The ROM numerical toolkit was extended to dynamically simulate a solar-geothermal system for a building structure with 826 apartments and 3032 solar thermal collectors.
- **Applied:** Several factors influence the performance of the solar-geothermal system, such as the spacing and depth of boreholes, flow rate, and temperature rise in the solar thermal collectors.

- **Applied:** The economic viability of such systems depends on the unit energy cost of natural gas and electricity at the studied location, considering the natural gas heating system as the existing heating energy source.

#### 6.4 Limitations and future work

In this thesis, a field-scale experimental and two different numerical models were developed to understand the performance of geothermal systems aimed at geothermal heat and power. It should be noted that while the numerical model developed accurately solves the fluid flow and heat transfer physics in the reservoir and the heat exchanger, material properties provided to the model correspond to properties of rocks of similar compositions/properties at a nearby location. The earth formation is more heterogeneous both axially and radially, and it is acknowledged that the conclusions drawn from this analysis could differ if the subsurface properties were different from those employed in this study. For both of the developed numerical models, although the sensitivity analysis was performed for different variables, all other design and operating variables were kept constant during the process. A multi-variable optimization methodology might yield a better design to achieve the most favorable outcome.

The target of this work was to provide recommendations to better understand the complex physics involved in geothermal systems. Future recommendations for single borehole experimental setups and numerical modeling include:

- The analysis performed as part of this thesis delves into the experimental and numerical study of a coaxial borehole heat exchanger and the geothermal reservoir. Conducting such field-scale experiments demands substantial financial and human resources. Hence, developing a numerical model based on experimental findings is a crucial step in

understanding the performance of the system with limited human resources and capital investment. The author recommends developing numerical models to study geothermal sites as it could significantly reduce the cost of experiments.

- The current model studies the performance of the system based on water as a Heat Transfer Fluid (HTF) in the heat exchanger; more analysis on other working fluids for the system should be done, including phase change carbon dioxide or liquid ammonia. Literature suggests that using ammonia as the HTF results in lower pressure losses, thus reducing pumping costs [125]. On the other hand, with supercritical CO<sub>2</sub>, a phase change occurs, enabling the capitalization of the latent heat of vaporization, thereby increasing the heat capacity of the HTF [126], [127].
- More drilling, and if possible, directional drilling into the layer is recommended, as the characteristics of certain layers may be more favorable for geothermal heat extraction and can lead to better thermal yield.

Similarly, future work recommendations for a multiple-borehole system in a solar-geothermal heating system are as follows:

- The use of solar-geothermal systems could contribute to decarbonization of heating in cold climates where the heating load is dominant, and there is insufficient sunshine intensity during winter.
- In the developed numerical model, further studies could be conducted by testing different configurations of the boreholes to achieve better thermal performance of the system, including circular or triangular arrangements of boreholes.
- The current study assumes uniform charging and discharging from the boreholes, where equal flow rates are assumed during the process. Exploring the effect of charging and

discharging with varying flow rates from the boreholes might help optimize the system in the future.

- The developed ROM employs an explicit time discretization scheme. It could be improved by using an implicit solver. Additionally, enhancements could be made to incorporate depth-varying soil properties and the conductive-convective heat transfer process in the soil.

## References

- [1] Y. N. Harari, *Sapiens: A brief history of humankind*. Random House, 2014.
- [2] H. Ritchie, L. Rodés-Guirao, E. Mathieu, and M. Gerber, “Population Growth,” *Our World in Data*, 2023.
- [3] H. Ritchie, M. Roser, and P. Rosado, “CO<sub>2</sub> and Greenhouse Gas Emissions,” *Our World in Data*, 2020.
- [4] H. Ritchie, M. Roser, and P. Rosado, “CO<sub>2</sub> and Greenhouse Gas Emissions,” *Our World in Data*, 2020.
- [5] L. Boulton, “Hot rocks - Geothermal and the role of nickel,” Nickel Institute.
- [6] IEA, “Technology Roadmap - Geothermal Heat and Power,” Paris, 2011. Accessed: Jul. 09, 2023. [Online]. Available: [technologyroadmapscontact@iea.org](mailto:technologyroadmapscontact@iea.org)
- [7] A. Richter, “GreenFire Energy wins partner for pilot project in Japan,” <https://www.thinkgeoenergy.com/greenfire-energy-wins-partner-for-pilot-project-in-japan/>.
- [8] MCFadden, “Types of Geothermal Systems,” <https://www.mcfaddenheating.com/products/geothermal/>.
- [9] A. Ritcher, “GreenFire Energy announces partner for its closed-loop geothermal power system pilot project,” <https://www.thinkgeoenergy.com/greenfire-energy-announces-partner-for-its-closed-loop-geothermal-power-system-pilot-project/>.
- [10] GreenFire Energy, “Case Study—Using Closed-Loop Technology to Unlock Geothermal That Cannot Be Accessed with Conventional Technology,” GreenFire Energy.
- [11] Emission Reduction Alberta, “EAVOR-LOOP DEMONSTRATION PROJECT,” <https://www.eralberta.ca/projects/details/eavor-loop-demonstration-project/>.

- [12] Eavor, “The world’s first Eavor-Loop™ for heat and power is under construction in Germany.,” <https://eavor-geretsried.de/en/>.
- [13] Energy.org, “DOE Awards \$8.4 Million for Accessing Geothermal Potential from Abandoned Oil and Gas Wells.” Accessed: Jun. 21, 2023. [Online]. Available: <https://www.energy.gov/eere/articles/doe-awards-84-million-accessing-geothermal-potential-abandoned-oil-and-gas-wells>
- [14] R-ACES, “Brødstrup district heating,” [https://r-aces.eu/use\\_case/braedstrup-district-heating/](https://r-aces.eu/use_case/braedstrup-district-heating/).
- [15] DLSC, “Drake Landing Solar Community,” <https://www.dlsc.ca/>.
- [16] ALTAROCK, “mmWave: Next Generation Deep Drilling Technology,” <https://altarockenergy.com/>.
- [17] J. W. Lund, “100 years of geothermal power product,” in *Proceedings Thirtieth Workshop on Geothermal Reservoir Engineering Stanford University*, 2005.
- [18] A. Richter, “ThinkGeoEnergy’s Top 10 Geothermal Countries 2022 – Power Generation Capacity (MW).” Accessed: Jun. 27, 2023. [Online]. Available: <https://www.thinkgeoenergy.com/thinkgeoenergys-top-10-geothermal-countries-2022-power-generation-capacity-mw/>
- [19] IEA, “Geothermal power generation in the Sustainable Development Scenario, 2000-2030.” Accessed: Jun. 27, 2023. [Online]. Available: <https://www.iea.org/data-and-statistics/charts/geothermal-power-generation-in-the-sustainable-development-scenario-2000-2030>, IEA. Licence: CC BY 4.0
- [20] L. Delevingne, W. Glazener, L. Grégoir, and K. Henderson, “Climate risk and decarbonization: What every mining CEO needs to know,” McKinsey sustainability.

- [21] E. Patsa, D. Van Zyl, S. J. Zarrouk, and N. Arianpoo, “Geothermal Energy in Mining Developments: Synergies and Opportunities Throughout a Mine’s Operational Life Cycle,” in *Proceedings World Geothermal Congress*, 2015, pp. 1–14.
- [22] A. Van Horn *et al.*, “New opportunities and applications for closed-loop geothermal energy systems,” *GRC Transactions*, vol. 44, pp. 1123–1143, 2020.
- [23] M. Kang *et al.*, “Direct measurements of methane emissions from abandoned oil and gas wells in Pennsylvania,” *Proceedings of the National Academy of Sciences*, vol. 111, no. 51, pp. 18173–18177, 2014.
- [24] O. Boucher, P. Friedlingstein, B. Collins, and K. P. Shine, “The indirect global warming potential and global temperature change potential due to methane oxidation,” *Environmental Research Letters*, vol. 4, no. 4, p. 44007, Oct. 2009, doi: 10.1088/1748-9326/4/4/044007.
- [25] EAVOR, “The Key Elements of an Eavor-Loop™,” <https://www.eavor.com/technology/>.
- [26] C. J. Wood, H. Liu, and S. B. Riffat, “Comparative performance of ‘U-tube’ and ‘coaxial’ loop designs for use with a ground source heat pump,” *Appl Therm Eng*, vol. 37, pp. 190–195, 2012, doi: <https://doi.org/10.1016/j.applthermaleng.2011.11.015>.
- [27] D. Quaggiotto *et al.*, “Simulation-Based Comparison Between the Thermal Behavior of Coaxial and Double U-Tube Borehole Heat Exchangers,” *Energies (Basel)*, vol. 12, no. 12, p. 2321, Jun. 2019, doi: 10.3390/en12122321.
- [28] J. Acuña, “Distributed thermal response tests : New insights on U-pipe and Coaxial heat exchangers in groundwater-filled boreholes,” KTH, Applied Thermodynamics and Refrigeration, 2013.

- [29] S. Javed, “Comparison of Performance and Effectiveness of Vertical Borehole Heat Exchanger Collectors,” 2018.
- [30] T. Sliwa and M. A. Rosen, “Efficiency analysis of borehole heat exchangers as grout varies via thermal response test simulations,” *Geothermics*, vol. 69, pp. 132–138, 2017.
- [31] J. A. Rangel Arista, J. J. Pacheco Ibarra, C. Rubio-Maya, O. J. González Pedraza, and D. Alcantar Martinez, “Numerical Analysis of Geothermal Heat Exchangers to be Implemented in a Geothermal-Solar Hybrid Power Plant for Electricity Production in Mexico,” in ASME International Mechanical Engineering Congress and Exposition, vol. Volume 6B: 2016. doi: 10.1115/IMECE2016-67869.
- [32] R. N. Horne, “Design considerations of a down-hole coaxial geothermal heat exchanger,” United States, 1980.
- [33] K. MORITA, F. MIZOGAMI, and W. S. BOLLMEIER, “Analysis of the Results from the Proof of Concept Experiment in Hawaii,” *Journal of the Geothermal Research Society of Japan*, vol. 15, no. 3, pp. 275–303, 1993.
- [34] Y. Noorollahi, S. Mohammadzadeh Bina, and H. Yousefi, “Simulation of Power Production from Dry Geothermal Well Using Down-hole Heat Exchanger in Sabalan Field, Northwest Iran,” *Natural Resources Research*, vol. 25, no. 2, pp. 227–239, 2016, doi: 10.1007/s11053-015-9270-3.
- [35] D. Siguenza, D. Wu, and G. Soriano, “Coaxial Borehole Heat Exchanger Simulation With Power Generation Potential for Chachimbiro, Ecuador,” in ASME International Mechanical Engineering Congress and Exposition, vol. Volume 6A: 2016. doi: 10.1115/IMECE2016-65862.

- [36] A. C. C. P, and S. E, “A comprehensive exergy evaluation of a deep borehole heat exchanger coupled with a ORC plant: the case study of Campi Flegrei,” *Energy*, vol. 189, p. 116100, 2019, doi: <https://doi.org/10.1016/j.energy.2019.116100>.
- [37] N. Yildirim, S. Parmanto, and G. G. Akkurt, “Thermodynamic assessment of downhole heat exchangers for geothermal power generation,” *Renew Energy*, vol. 141, pp. 1080–1091, 2019, doi: <https://doi.org/10.1016/j.renene.2019.04.049>.
- [38] K. Morita, M. Tago, and S. Ehara, “Case studies on small-scale power generation with the downhole coaxial heat exchanger,” in *Proceedings of the World Geothermal Congress. Turkey, Antalya*, 2005, pp. 1–8.
- [39] C. Dai, Y. Shi, L. Zeng, J. Li, and H. Lei, “Heat Extraction Performance of a Deep Downhole Heat Exchanger,” *Energy Procedia*, vol. 158, pp. 5602–5607, 2019.
- [40] P. J. Yekoladio, T. Bello-Ochende, and J. P. Meyer, “Design and optimization of a downhole coaxial heat exchanger for an enhanced geothermal system (EGS),” *Renew Energy*, vol. 55, pp. 128–137, 2013.
- [41] Y. Feng, M. Tyagi, and C. D. White, “A downhole heat exchanger for horizontal wells in low-enthalpy geopressured geothermal brine reservoirs,” *Geothermics*, vol. 53, pp. 368–378, 2015, doi: <https://doi.org/10.1016/j.geothermics.2014.07.007>.
- [42] Z. Wang, M. W. McClure, and R. N. Horne, “A single-well EGS configuration using a thermosiphon,” in *Workshop on Geothermal Reservoir Engineering, Stanford University, Stanford, California*, 2009.
- [43] A. Dahi Taleghani, “An improved closed-loop heat extraction method from geothermal resources,” *J Energy Resour Technol*, vol. 135, no. 4, 2013.

- [44] G. Nalla, G. M. Shook, G. L. Mines, and K. K. Bloomfield, “Parametric sensitivity study of operating and design variables in wellbore heat exchangers,” *Geothermics*, vol. 34, no. 3, pp. 330–346, 2005, doi: <https://doi.org/10.1016/j.geothermics.2005.02.001>.
- [45] J. D. Templeton, S. A. Ghoreishi-Madiseh, F. Hassani, and M. J. Al-Khawaja, “Abandoned petroleum wells as sustainable sources of geothermal energy,” *Energy*, vol. 70, pp. 366–373, Jun. 2014, doi: [10.1016/J.ENERGY.2014.04.006](https://doi.org/10.1016/J.ENERGY.2014.04.006).
- [46] Z. Hu *et al.*, “Thermal and fluid processes in a closed-loop geothermal system using CO<sub>2</sub> as a working fluid,” *Renew Energy*, vol. 154, pp. 351–367, 2020, doi: <https://doi.org/10.1016/j.renene.2020.02.096>.
- [47] D. Gordon, T. Bolisetti, D. S.-K. Ting, and S. Reitsma, “Experimental and analytical investigation on pipe sizes for a coaxial borehole heat exchanger,” *Renew Energy*, vol. 115, pp. 946–953, 2018, doi: <https://doi.org/10.1016/j.renene.2017.08.088>.
- [48] J. Nordbeck, C. Beyer, and S. Bauer, “Experimental and numerical analysis of a cement based thermal energy storage system with a helical heat exchanger,” *Appl Therm Eng*, vol. 185, p. 116339, 2021, doi: <https://doi.org/10.1016/j.applthermaleng.2020.116339>.
- [49] G. Emmi and M. Bottarelli, “Enhancement of shallow ground heat exchanger with phase change material,” *Renew Energy*, vol. 206, pp. 828–837, 2023, doi: <https://doi.org/10.1016/j.renene.2023.02.079>.
- [50] K. Morita, W. S. Bollmeier, and H. Mizogami, “An experiment to prove the concept of the downhole coaxial heat exchanger (DCHE) in Hawaii,” 1992.
- [51] Z. Wang, F. Wang, J. Liu, Z. Ma, E. Han, and M. Song, “Field test and numerical investigation on the heat transfer characteristics and optimal design of the heat exchangers

- of a deep borehole ground source heat pump system,” *Energy Convers Manag*, vol. 153, pp. 603–615, 2017, doi: <https://doi.org/10.1016/j.enconman.2017.10.038>.
- [52] C. Dai, J. Li, Y. Shi, L. Zeng, and H. Lei, “An experiment on heat extraction from a deep geothermal well using a downhole coaxial open loop design,” *Appl Energy*, vol. 252, p. 113447, 2019.
- [53] Y. Huang, Y. Zhang, Y. Xie, Y. Zhang, X. Gao, and J. Ma, “Field test and numerical investigation on deep coaxial borehole heat exchanger based on distributed optical fiber temperature sensor,” *Energy*, vol. 210, p. 118643, 2020.
- [54] D. Gordon, T. Bolisetti, D. S.-K. Ting, and S. Reitsma, “Short-term fluid temperature variations in either a coaxial or U-tube borehole heat exchanger,” *Geothermics*, vol. 67, pp. 29–39, 2017.
- [55] Y. Luo, H. Guo, F. Meggers, and L. Zhang, “Deep coaxial borehole heat exchanger: Analytical modeling and thermal analysis,” *Energy*, vol. 185, pp. 1298–1313, 2019.
- [56] S. Erol and B. François, “Multilayer analytical model for vertical ground heat exchanger with groundwater flow,” *Geothermics*, vol. 71, pp. 294–305, 2018.
- [57] A. Pan, L. Lu, P. Cui, and L. Jia, “A new analytical heat transfer model for deep borehole heat exchangers with coaxial tubes,” *Int J Heat Mass Transf*, vol. 141, pp. 1056–1065, 2019.
- [58] C. Alimonti and E. Soldo, “Study of geothermal power generation from a very deep oil well with a wellbore heat exchanger,” *Renew Energy*, vol. 86, pp. 292–301, 2016, doi: <https://doi.org/10.1016/j.renene.2015.08.031>.

- [59] F. T. Adler, A. C. Ingersoll, L. R. Ingersoll, and H. J. Plass, *Theory of earth heat exchangers for the heat pump*. [Emmitsburg, MD]: [National Emergency Training Center], 1950.
- [60] D. Mottaghy and L. Dijkshoorn, “Implementing an effective finite difference formulation for borehole heat exchangers into a heat and mass transport code,” *Renew Energy*, vol. 45, pp. 59–71, 2012.
- [61] X. Song *et al.*, “Numerical analysis of heat extraction performance of a deep coaxial borehole heat exchanger geothermal system,” *Energy*, vol. 164, pp. 1298–1310, 2018, doi: <https://doi.org/10.1016/j.energy.2018.08.056>.
- [62] X. Hu, J. Banks, L. Wu, and W. V. Liu, “Numerical modeling of a coaxial borehole heat exchanger to exploit geothermal energy from abandoned petroleum wells in Hinton, Alberta,” *Renew Energy*, vol. 148, pp. 1110–1123, 2020.
- [63] J. C. Choi, J. Park, and S. R. Lee, “Numerical evaluation of the effects of groundwater flow on borehole heat exchanger arrays,” *Renew Energy*, vol. 52, pp. 230–240, 2013.
- [64] E.-J. Kim, J.-J. Roux, G. Rusaouen, and F. Kuznik, “Numerical modelling of geothermal vertical heat exchangers for the short time analysis using the state model size reduction technique,” *Appl Therm Eng*, vol. 30, no. 6–7, pp. 706–714, 2010.
- [65] Y. Noorollahi, M. Pourarshad, S. Jalilinasrabad, and H. Yousefi, “Numerical simulation of power production from abandoned oil wells in Ahwaz oil field in southern Iran,” *Geothermics*, vol. 55, pp. 16–23, 2015.
- [66] S. Iry and R. Rafee, “Transient numerical simulation of the coaxial borehole heat exchanger with the different diameters ratio,” *Geothermics*, vol. 77, pp. 158–165, 2019.

- [67] F. Luo, R.-N. Xu, and P.-X. Jiang, “Numerical investigation of fluid flow and heat transfer in a doublet enhanced geothermal system with CO<sub>2</sub> as the working fluid (CO<sub>2</sub>-EGS),” *Energy*, vol. 64, pp. 307–322, 2014.
- [68] S. Pokhrel *et al.*, “Thermal performance evaluation of integrated solar-geothermal system; a semi-conjugate reduced order numerical model,” *Appl Energy*, vol. 303, p. 117676, 2021, doi: <https://doi.org/10.1016/j.apenergy.2021.117676>.
- [69] M. A. Alzoubi and A. P. Sasmito, “Thermal performance optimization of a bayonet tube heat exchanger,” *Appl Therm Eng*, vol. 111, pp. 232–247, 2017.
- [70] T. Renaud, P. Verdin, and G. Falcone, “Numerical simulation of a Deep Borehole Heat Exchanger in the Krafla geothermal system,” *Int J Heat Mass Transf*, vol. 143, p. 118496, 2019.
- [71] H. Holmberg, J. Acuña, E. Næss, and O. K. Sønju, “Thermal evaluation of coaxial deep borehole heat exchangers,” *Renew Energy*, vol. 97, pp. 65–76, 2016, doi: <https://doi.org/10.1016/j.renene.2016.05.048>.
- [72] E. Zanchini, S. Lazzari, and A. Priarone, “Improving the thermal performance of coaxial borehole heat exchangers,” *Energy*, vol. 35, no. 2, pp. 657–666, 2010.
- [73] T. Renaud, P. Verdin, L. Pan, and G. Falcone, “Heat Transfer Modelling of an Unconventional, Closed-Loop Geothermal Well,” 2020.
- [74] H. Tang, B. Xu, A. R. Hasan, Z. Sun, and J. Killough, “Modeling wellbore heat exchangers: Fully numerical to fully analytical solutions,” *Renew Energy*, vol. 133, pp. 1124–1135, 2019, doi: <https://doi.org/10.1016/j.renene.2018.10.094>.

- [75] C. Li, Y. Guan, R. Yang, X. Lu, W. Xiong, and A. Long, “Effect of inner pipe type on the heat transfer performance of deep-buried coaxial double-pipe heat exchangers,” *Renew Energy*, vol. 145, pp. 1049–1060, 2020.
- [76] R. A. Beier, M. Fossa, and S. Morchio, “Models of thermal response tests on deep coaxial borehole heat exchangers through multiple ground layers,” *Appl Therm Eng*, vol. 184, p. 116241, 2021, doi: <https://doi.org/10.1016/j.applthermaleng.2020.116241>.
- [77] T. Renaud, P. Verdin, and G. Falcone, “Numerical simulation of a Deep Borehole Heat Exchanger in the Krafla geothermal system,” *Int J Heat Mass Transf*, vol. 143, p. 118496, 2019, doi: <https://doi.org/10.1016/j.ijheatmasstransfer.2019.118496>.
- [78] J. Ma, Q. Jiang, Q. Zhang, Y. Xie, Y. Wang, and F. Yi, “Effect of groundwater forced seepage on heat transfer characteristics of borehole heat exchangers,” *Geothermal Energy*, vol. 9, no. 1, p. 11, 2021, doi: 10.1186/s40517-021-00192-1.
- [79] S. Geng, Y. Li, X. Han, H. Lian, and H. Zhang, “Evaluation of Thermal Anomalies in Multi-Boreholes Field Considering the Effects of Groundwater Flow,” *Sustainability*, vol. 8, no. 6, 2016, doi: 10.3390/su8060577.
- [80] W. Zhang, H. Yang, L. Fang, P. Cui, and Z. Fang, “Study on heat transfer of pile foundation ground heat exchanger with three-dimensional groundwater seepage,” *Int J Heat Mass Transf*, vol. 105, pp. 58–66, Feb. 2017, doi: 10.1016/J.IJHEATMASSTRANSFER.2016.09.066.
- [81] W. Zhang, H. Yang, X. Guo, M. Yu, and Z. Fang, “Investigation on groundwater velocity based on the finite line heat source seepage model,” *Int J Heat Mass Transf*, vol. 99, pp. 391–401, Aug. 2016, doi: 10.1016/J.IJHEATMASSTRANSFER.2016.03.057.

- [82] A. Tolooiyan and P. Hemmingway, “A preliminary study of the effect of groundwater flow on the thermal front created by borehole heat exchangers,” *International Journal of Low-Carbon Technologies*, vol. 9, no. 4, pp. 284–295, Dec. 2014, doi: 10.1093/ijlct/cts077.
- [83] G. Brunetti, H. Saito, T. Saito, and J. Šimůnek, “A computationally efficient pseudo-3D model for the numerical analysis of borehole heat exchangers,” *Appl Energy*, vol. 208, pp. 1113–1127, Dec. 2017, doi: 10.1016/J.APENERGY.2017.09.042.
- [84] C. Li, P. J. Cleall, J. Mao, and J. J. Muñoz-Criollo, “Numerical simulation of ground source heat pump systems considering unsaturated soil properties and groundwater flow,” *Appl Therm Eng*, vol. 139, pp. 307–316, Jul. 2018, doi: 10.1016/J.APPLTHERMALENG.2018.04.142.
- [85] Y. Wang, Z. Liu, X. Yuan, X. Niu, and J. Liu, “Investigation of the influence of groundwater seepage on the heat transfer characteristics of a ground source heat pump system with a 9-well group,” *Build Simul*, vol. 12, no. 5, pp. 857–868, 2019, doi: 10.1007/s12273-019-0526-4.
- [86] K. Chen, J. Zheng, J. Li, J. Shao, and Q. Zhang, “Numerical study on the heat performance of enhanced coaxial borehole heat exchanger and double U borehole heat exchanger,” *Appl Therm Eng*, vol. 203, p. 117916, 2022, doi: <https://doi.org/10.1016/j.applthermaleng.2021.117916>.
- [87] L. Amiri, S. A. Ghoreishi-Madiseh, F. P. Hassani, and A. P. Sasmito, “Estimating pressure drop and Ergun/Forchheimer parameters of flow through packed bed of spheres with large particle diameters,” *Powder Technol*, vol. 356, pp. 310–324, 2019, doi: <https://doi.org/10.1016/j.powtec.2019.08.029>.

- [88] S. Warkerkar, S. Schmitz, J. Goettsche, B. Hoffschmidt, M. Reißel, and R. Tamme, “Air-Sand Heat Exchanger for High-Temperature Storage,” *J Sol Energy Eng*, vol. 133, no. 2, Apr. 2011, doi: 10.1115/1.4003583.
- [89] N. Pastore, C. Cherubini, D. Rapti, and C. I. Giasi, “Experimental study of forced convection heat transport in porous media,” *Nonlinear Process Geophys*, vol. 25, no. 2, pp. 279–290, 2018, doi: 10.5194/npg-25-279-2018.
- [90] J. Chen and F. Jiang, “A numerical study of EGS heat extraction process based on a thermal non-equilibrium model for heat transfer in subsurface porous heat reservoir,” *Heat and Mass Transfer*, vol. 52, no. 2, pp. 255–267, 2016, doi: 10.1007/s00231-015-1554-y.
- [91] Y. Ma, Y. Zhang, Y. Huang, Y. Zhang, and Z. Hu, “Experimental study on flow and heat transfer characteristics of water flowing through a rock fracture induced by hydraulic fracturing for an enhanced geothermal system,” *Appl Therm Eng*, vol. 154, pp. 433–441, 2019, doi: <https://doi.org/10.1016/j.applthermaleng.2019.03.114>.
- [92] S. K. Shah, L. Aye, and B. Rismanchi, “Seasonal thermal energy storage system for cold climate zones: A review of recent developments,” *Renewable and Sustainable Energy Reviews*.
- [93] J. Formhals, H. Hemmatabady, B. Welsch, D. O. Schulte, and I. Sass, “A Modelica Toolbox for the Simulation of Borehole Thermal Energy Storage Systems,” *Energies (Basel)*, vol. 13, no. 9, 2020, doi: 10.3390/en13092327.
- [94] F. Zhang *et al.*, “Long-term dynamic heat transfer analysis for the borehole spacing planning of multiple deep borehole heat exchanger,” *Case Studies in Thermal Engineering*, vol. 38, p. 102373, 2022.

- [95] R. Al-Khoury, T. Kölbl, and R. Schramedei, “Efficient numerical modeling of borehole heat exchangers,” *Comput Geosci*, vol. 36, no. 10, pp. 1301–1315, 2010.
- [96] C. Verhelst and L. Helsen, “Low-order state space models for borehole heat exchangers,” *HVAC&R Res*, vol. 17, no. 6, pp. 928–947, Dec. 2011, doi: 10.1080/10789669.2011.617188.
- [97] S. Pokhrel *et al.*, “Evaluation of a novel integrated solar-borehole thermal energy storage system for residential high-rise building heating applications,” in *International Conference on Applied Energy*, Bangkok/virtual, 2020.
- [98] A. S. Ramadan, “Parametric Study of Vertical Ground Loop Heat Exchangers for Ground Source Heat Pump Systems,” The University of Western Ontario, 2016. doi: . Electronic Thesis and Dissertation Repository. 3521.
- [99] C. G. Cvetkovski, “Modelling of flow and heat transport in vertical loop ground heat exchangers,” 2014.
- [100] Y. Luo, J. Yu, T. Yan, L. Zhang, and X. Liu, “Improved analytical modeling and system performance evaluation of deep coaxial borehole heat exchanger with segmented finite cylinder-source method,” *Energy Build*, vol. 212, p. 109829, 2020, doi: <https://doi.org/10.1016/j.enbuild.2020.109829>.
- [101] W. Cai *et al.*, “Analysis of heat extraction performance and long-term sustainability for multiple deep borehole heat exchanger array: A project-based study,” *Appl Energy*, vol. 289, p. 116590, 2021, doi: <https://doi.org/10.1016/j.apenergy.2021.116590>.
- [102] S. Chen, F. Witte, O. Kolditz, and H. Shao, “Shifted thermal extraction rates in large Borehole Heat Exchanger array – A numerical experiment,” *Appl Therm Eng*, vol. 167, p. 114750, 2020, doi: <https://doi.org/10.1016/j.applthermaleng.2019.114750>.

- [103] A. F. Zueter, M. Xu, M. A. Alzoubi, and A. P. Sasmito, “Development of conjugate reduced-order models for selective artificial ground freezing: Thermal and computational analysis,” *Appl Therm Eng*, vol. 190, p. 116782, 2021, doi: <https://doi.org/10.1016/j.applthermaleng.2021.116782>.
- [104] E. Zanchini and S. Lazzari, “New g-functions for the hourly simulation of double U-tube borehole heat exchanger fields,” *Energy*, vol. 70, pp. 444–455, 2014.
- [105] I. M. Kutasov and L. V Eppelbaum, “Determination of formation temperature from bottom-hole temperature logs—a generalized Horner method,” *Journal of Geophysics and Engineering*, vol. 2, no. 2, pp. 90–96, 2005.
- [106] R. J. Schoepfel and S. Gilarranz, “Use of well log temperatures to evaluate regional geothermal gradients,” *Journal of Petroleum Technology*, vol. 18, no. 06, pp. 667–673, 1966.
- [107] W. L. Dowdle and W. M. Cobb, “Static formation temperature from well logs—an empirical method,” *Journal of Petroleum Technology*, vol. 27, no. 11, pp. 1326–1330, 1975.
- [108] W. H. Fertl and D. J. Timko, “Parameters for identification of overpressure formations,” in *SPE Drilling and Rock Mechanics Conference*, SPE, 1971, p. SPE-3223.
- [109] A. P. Davis and E. E. Michaelides, “Geothermal power production from abandoned oil wells,” *Energy*, vol. 34, no. 7, pp. 866–872, 2009, doi: <https://doi.org/10.1016/j.energy.2009.03.017>.
- [110] K. Kitaoka, “Water circulation rates in a geothermal field: a study of tritium in the Beppu hydrothermal system, Japan,” *Geothermics*, vol. 19, no. 6, pp. 515–539, 1990.

- [111] R. G. Allis, “Geophysical anomalies over epithermal systems,” *J Geochem Explor*, vol. 36, no. 1–3, pp. 339–374, 1990.
- [112] Y. Yusa and S. Ohsawa, “Age of the Beppu hydrothermal system, Japan,” in *Proceedings of the World Geothermal Congress, Kyushu-Tohoku, Japan*, 2000, pp. 305–308.
- [113] R. G. Allis and Y. Yusa, “Fluid flow processes in the Beppu geothermal system, Japan,” *Geothermics*, vol. 18, no. 5–6, pp. 743–759, 1989.
- [114] D. A. Nield and A. Bejan, *Convection in porous media*, vol. 3. Springer, 2006.
- [115] M. Kaviany, *Principles of heat transfer in porous media*. Springer Science & Business Media, 2012.
- [116] R. G. Carbonell and S. Whitaker, “Heat and mass transfer in porous media,” in *Fundamentals of transport phenomena in porous media*, Springer, 1984, pp. 121–198.
- [117] W. J. Minkowycz, A. Haji-Sheikh, and K. F. Vafai, “On departure from local thermal equilibrium in porous media due to a rapidly changing heat source: the Sparrow number,” *Int J Heat Mass Transf*, vol. 42, no. 18, pp. 3373–3385, 1999.
- [118] N. C. Sturchio, S. Ohsawa, Y. Sano, G. Arehart, K. Kitaoka, and Y. Yusa, “Geochemical characteristics of the Yufuin outflow plume, Beppu hydrothermal system, Japan,” *Geothermics*, vol. 25, no. 2, pp. 215–230, 1996.
- [119] R. A. Bowman, A. C. Mueller, and W. M. Nagle, “Mean temperature difference in design,” *Transactions of the American Society of Mechanical Engineers*, vol. 62, no. 4, pp. 283–293, 1940.
- [120] 2010. ASHRAE, “ANSI/ASHRAE Standard 62.1-2010, Ventilation for Acceptable Indoor Air Quality,” 2010.

- [121] N. Granzotto *et al.*, “Energy and acoustic performances of windows and their correlation,” *Energy Build*, vol. 136, pp. 189–198, Feb. 2017, doi: 10.1016/J.ENBUILD.2016.12.024.
- [122] Apricus eco-energy, “No TETC-30 Solar Collector.” Accessed: Jul. 13, 2021. [Online]. Available: <https://www.apricus.com/ETC-30-Solar-Collector-pd43215927.html>
- [123] S. Pokhrel, A. F. Kuyuk, H. Kalantari, and S. A. Ghoreishi-Madiseh, “Techno-Economic Trade-Off between Battery Storage and Ice Thermal Energy Storage for Application in Renewable Mine Cooling System,” *Applied Sciences*, vol. 10, no. 17, 2020, doi: 10.3390/app10176022.
- [124] Canada government, “CANADA’S 2021 NATIONALLY DETERMINED CONTRIBUTION UNDER THE PARIS AGREEMENT,” Ottawa, 2021. [Online]. Available: [https://www4.unfccc.int/sites/ndcstaging/PublishedDocuments/Canada First/Canada%27s Enhanced NDC Submission1\\_FINAL EN.pdf](https://www4.unfccc.int/sites/ndcstaging/PublishedDocuments/Canada%27s%20Enhanced%20NDC%20Submission1_FINAL%20EN.pdf)
- [125] J. Dai, J. Li, T. Wang, L. Zhu, K. Tian, and Z. Chen, “Thermal performance analysis of coaxial borehole heat exchanger using liquid ammonia,” *Energy*, vol. 263, p. 125986, 2023, doi: <https://doi.org/10.1016/j.energy.2022.125986>.
- [126] M. Bai, F. Wang, J. Liu, W. Cai, and Z. Wang, “Discrepancies in using CO<sub>2</sub> or water as heat-carrier fluid on the output temperature of deep coaxial borehole heat exchanger,” *Energy Build*, vol. 270, p. 112279, 2022, doi: <https://doi.org/10.1016/j.enbuild.2022.112279>.
- [127] G. Zhao, L. Wang, Z. Liang, Q. Liu, and F. Jiang, “Thermal response analysis of a medium-deep coaxial borehole heat exchanger by circulating CO<sub>2</sub>,” *Geothermics*, vol. 112, p. 102746, 2023, doi: <https://doi.org/10.1016/j.geothermics.2023.102746>.

## Appendices

### Appendix A : Fluent UDF

```
#include "udf.h"

DEFINE_INIT(my_init_func, d)
{
    cell_t c;
    Thread* t;
    real xc[ND_ND]; /*location vector*/
    real x; /*depth*/

    /* loop over all cell threads in the domain */
    thread_loop_c(t, d)

    {
        if (THREAD_ID(t) == 44 || THREAD_ID(t) == 45 || THREAD_ID(t) == 46 ||
            THREAD_ID(t) == 47 || THREAD_ID(t) == 48 || THREAD_ID(t) == 49 ||
            THREAD_ID(t) == 50)
            { /* loop over all cells */
                begin_c_loop(c, t)

                    {
                        C_CENTROID(xc, c, t); /*centroid of the cell*/
                        x = xc[1];
                        if (x >= 250)
                            {
                                C_T(c, t) = 304.15;
                            }
                        else if (x >= 245.00)
                            {
                                C_T(c, t) = (-1.03 * (x - 1 * 250.00)) + 304.15;
                            }
                        else if (x >= 240.17)
                            {
                                C_T(c, t) = (-1.55 * (x - 1 * 245.00)) + 309.29;
                            }
                        else if (x >= 235.11)
                            {
                                C_T(c, t) = (-2.37 * (x - 1 * 240.17)) + 316.76;
                            }
                        else if (x >= 230.04)
                            {
                                C_T(c, t) = (-3.18 * (x - 1 * 235.11)) + 328.74;
                            }
                        else if (x >= 224.98)
                            {
                                C_T(c, t) = (-1.91 * (x - 1 * 230.04)) + 344.86;
                            }
                        else if (x >= 219.92)
                            {
                                C_T(c, t) = (-1.13 * (x - 1 * 224.98)) + 354.54;
                            }
                    }
            }
        }
    }
}
```

```

}
else if (x >= 214.85)
{
    C_T(c, t) = (-1.62 * (x - 1 * 219.92)) + 360.27;
}
else if (x >= 209.79)
{
    C_T(c, t) = (-0.89 * (x - 1 * 214.85)) + 368.48;
}
else if (x >= 204.72)
{
    C_T(c, t) = (-0.34 * (x - 1 * 209.79)) + 372.99;
}
else if (x >= 199.66)
{
    C_T(c, t) = (-0.29 * (x - 1 * 204.72)) + 374.73;
}
else if (x >= 194.60)
{
    C_T(c, t) = (-0.39 * (x - 1 * 199.66)) + 376.19;
}
else if (x >= 189.53)
{
    C_T(c, t) = (-0.36 * (x - 1 * 194.60)) + 378.18;
}
else if (x >= 185.48)
{
    C_T(c, t) = (-0.57 * (x - 1 * 189.53)) + 380.01;
}
else if (x >= 180.42)
{
    C_T(c, t) = (-1.09 * (x - 1 * 185.48)) + 382.30;
}
else if (x >= 175.35)
{
    C_T(c, t) = (-1.15 * (x - 1 * 180.42)) + 387.81;
}
else if (x >= 170.29)
{
    C_T(c, t) = (-0.81 * (x - 1 * 175.35)) + 393.64;
}
else if (x >= 165.22)
{
    C_T(c, t) = (-0.43 * (x - 1 * 170.29)) + 397.74;
}
else if (x >= 160.16)
{
    C_T(c, t) = (-1.05 * (x - 1 * 165.22)) + 399.93;
}
else if (x >= 155.10)
{
    C_T(c, t) = (-1.12 * (x - 1 * 160.16)) + 405.24;
}
else if (x >= 150.03)
{

```

```

    C_T(c, t) = (-1.40 * (x - 1 * 155.10)) + 410.91;
}
else if (x >= 146.99)
{
    C_T(c, t) = (-1.33 * (x - 1 * 150.03)) + 417.99;
}
else if (x >= 142.94)
{
    C_T(c, t) = (-0.56 * (x - 1 * 146.99)) + 422.04;
}
else if (x >= 136.87)
{
    C_T(c, t) = (-0.18 * (x - 1 * 142.94)) + 424.31;
}
else if (x >= 129.78)
{
    C_T(c, t) = (-0.20 * (x - 1 * 136.87)) + 425.42;
}
else if (x >= 124.71)
{
    C_T(c, t) = (-0.36 * (x - 1 * 129.78)) + 426.80;
}
else if (x >= 121.67)
{
    C_T(c, t) = (-1.33 * (x - 1 * 124.71)) + 428.62;
}
else if (x >= 119.65)
{
    C_T(c, t) = (-1.99 * (x - 1 * 121.67)) + 432.68;
}
else if (x >= 106.48)
{
    C_T(c, t) = (-1.65 * (x - 1 * 119.65)) + 436.70;
}
else if (x >= 103.44)
{
    C_T(c, t) = (0.00 * (x - 1 * 106.48)) + 458.45;
}
else if (x >= 93.31)
{
    C_T(c, t) = (-0.00 * (x - 1 * 103.44)) + 458.45;
}
else if (x >= 75.08)
{
    C_T(c, t) = (-0.08 * (x - 1 * 93.31)) + 458.48;
}
else if (x >= 74.07)
{
    C_T(c, t) = (0.25 * (x - 1 * 75.08)) + 459.87;
}
else if (x >= 73.06)
{
    C_T(c, t) = (0.00 * (x - 1 * 74.07)) + 459.61;
}
else if (x >= 72.00)

```

```

{
  C_T(c, t) = (0.00 * (x - 1 * 73.06)) + 459.61;
}
else if (x >= 71.00)
{
  C_T(c, t) = (0.00 * (x - 1 * 72.00)) + 459.61;
}
else if (x >= 70.00)
{
  C_T(c, t) = (0.00 * (x - 1 * 71.00)) + 459.61;
}
else if (x >= 65.00)
{
  C_T(c, t) = (0.12 * (x - 1 * 70.00)) + 459.61;
}
else if (x >= 50.00)
{
  C_T(c, t) = (0.60 * (x - 1 * 65.00)) + 459.03;
}
else if (x >= 25.00)
{
  C_T(c, t) = (0.15 * (x - 1 * 50.00)) + 450.07;
}
else if (x >= 0.00)
{
  C_T(c, t) = (0.11 * (x - 1 * 25.00)) + 446.20;
}
else if (x >= -25.00)
{
  C_T(c, t) = (0.03 * (x - 1 * 0.00)) + 443.52;
}
else if (x >= -50.00)
{
  C_T(c, t) = (-0.04 * (x - 1 * -25.00)) + 442.78;
}
else if (x >= -75.00)
{
  C_T(c, t) = (-0.12 * (x - 1 * -50.00)) + 443.68;
}
else if (x >= -100.00)
{
  C_T(c, t) = (-0.15 * (x - 1 * -75.00)) + 446.64;
}
else if (x >= -125.00)
{
  C_T(c, t) = (-0.19 * (x - 1 * -100.00)) + 450.31;
}
else if (x >= -150.00)
{
  C_T(c, t) = (-0.22 * (x - 1 * -125.00)) + 455.12;
}
else if (x >= -175.00)
{
  C_T(c, t) = (-0.23 * (x - 1 * -150.00)) + 460.58;
}
}

```



```

}
else if (x >= 183.46)
{
    C_T(c, t) = ((-0.36) * (x - 193.58)) + 415.92;
}
else if (x >= 170.29)
{
    C_T(c, t) = ((-0.68) * (x - 183.46)) + 419.61;
}
else if (x >= 154.08)
{
    C_T(c, t) = ((-0.29) * (x - 170.29)) + 428.62;
}
else if (x >= 144.97)
{
    C_T(c, t) = ((1.12) * (x - 154.08)) + 433.40;
}
else if (x >= 140.92)
{
    C_T(c, t) = ((1.62) * (x - 144.97)) + 423.21;
}
else if (x >= 136.87)
{
    C_T(c, t) = ((0.51) * (x - 140.92)) + 416.65;
}
else if (x >= 131.80)
{
    C_T(c, t) = ((1.85) * (x - 136.87)) + 414.57;
}
else if (x >= 128.76)
{
    C_T(c, t) = ((-1.36) * (x - 131.80)) + 405.19;
}
else if (x >= 126.74)
{
    C_T(c, t) = ((-2.64) * (x - 128.76)) + 409.31;
}
else if (x >= 119.65)
{
    C_T(c, t) = ((-1.17) * (x - 126.74)) + 414.64;
}
else if (x >= 115.6)
{
    C_T(c, t) = ((-5.06) * (x - 119.65)) + 422.93;
}
else if (x >= 113.57)
{
    C_T(c, t) = ((-3.52) * (x - 115.60)) + 443.41;
}
else if (x >= 110.53)
{
    C_T(c, t) = ((-1.12) * (x - 113.57)) + 450.56;
}
else if (x >= 82.17)
{

```

```

    C_T(c, t) = ((-0.11) * (x - 110.53)) + 453.95;
}
else if (x >= 72.05)
{
    C_T(c, t) = ((-0.09) * (x - 82.17)) + 457.21;
}
else if (x >= 67.99)
{
    C_T(c, t) = ((2.23) * (x - 72.05)) + 458.15;
}
else if (x >= 61.92)
{
    C_T(c, t) = ((0.66) * (x - 67.99)) + 449.11;
}
else if (x >= 51.79)
{
    C_T(c, t) = ((0.26) * (x - 61.92)) + 445.10;
}
else if (x >= 34.57)
{
    C_T(c, t) = ((0.13) * (x - 51.79)) + 442.47;
}
else if (x >= 17.35)
{
    C_T(c, t) = ((0.16) * (x - 34.57)) + 440.31;
}
else if (x >= -1.89)
{
    C_T(c, t) = ((0.04) * (x - 17.35)) + 437.60;
}
else if (x >= -31.26)
{
    C_T(c, t) = ((0.04) * (x + 1.89)) + 436.79;
}
else if (x >= -59.62)
{
    C_T(c, t) = ((-0.08) * (x + 31.26)) + 435.64;
}
else if (x >= -85.95)
{
    C_T(c, t) = ((-0.13) * (x + 59.62)) + 437.86;
}
else if (x >= -109.25)
{
    C_T(c, t) = ((-0.16) * (x + 85.95)) + 441.26;
}
else if (x >= -138.89)
{
    C_T(c, t) = ((-0.19) * (x + 109.25)) + 444.95;
}
else if (x >= -171.03)
{
    C_T(c, t) = ((-0.23) * (x + 138.62)) + 450.48;
}
else if (x >= -180.14)

```

```

        {
            C_T(c, t) = ((-0.25) * (x + 171.03)) + 457.89;
        }
        else if (x >= -186.22)
        {
            C_T(c, t) = ((-0.20) * (x + 180.14)) + 460.18;
        }
        else if (x >= -198.38)
        {
            C_T(c, t) = ((-0.19) * (x + 186.22)) + 461.37;
        }
        else if (x >= -229.77)
        {
            C_T(c, t) = ((-0.19) * (x + 198.38)) + 463.70;
        }
        else
        {
            C_T(c, t) = 469.77;
        }
    }
    end_c_loop(c, t)
}
}
}

```

```

DEFINE_PROFILE(temperature_profile, t, i)
{
    #if PARALLEL

        real x[ND_ND]; /*location vector*/
        real y; /*depth*/
        real p;
        face_t f;
        begin_f_loop(f, t)

            {
                F_CENTROID(x, f, t); /*centroid of the cell*/
                y = x[1];

                if (y >= 250.0)
                {
                    p = 304.15;
                }
                else if (y >= 245.00)
                {
                    p = (-1.03 * (y - 1 * 250.00)) + 304.15;
                }
                else if (y >= 240.17)
                {
                    p = (-1.55 * (y - 1 * 245.00)) + 309.29;
                }
                else if (y >= 235.11)
            }
        }
    }

```

```

{
  p = (-2.37 * (y - 1 * 240.17)) + 316.76;
}
else if (y >= 230.04)
{
  p = (-3.18 * (y - 1 * 235.11)) + 328.74;
}
else if (y >= 224.98)
{
  p = (-1.91 * (y - 1 * 230.04)) + 344.86;
}
else if (y >= 219.92)
{
  p = (-1.13 * (y - 1 * 224.98)) + 354.54;
}
else if (y >= 214.85)
{
  p = (-1.62 * (y - 1 * 219.92)) + 360.27;
}
else if (y >= 209.79)
{
  p = (-0.89 * (y - 1 * 214.85)) + 368.48;
}
else if (y >= 204.72)
{
  p = (-0.34 * (y - 1 * 209.79)) + 372.99;
}
else if (y >= 199.66)
{
  p = (-0.29 * (y - 1 * 204.72)) + 374.73;
}
else if (y >= 194.60)
{
  p = (-0.39 * (y - 1 * 199.66)) + 376.19;
}
else if (y >= 189.53)
{
  p = (-0.36 * (y - 1 * 194.60)) + 378.18;
}
else if (y >= 185.48)
{
  p = (-0.57 * (y - 1 * 189.53)) + 380.01;
}
else if (y >= 180.42)
{
  p = (-1.09 * (y - 1 * 185.48)) + 382.30;
}
else if (y >= 175.35)
{
  p = (-1.15 * (y - 1 * 180.42)) + 387.81;
}
else if (y >= 170.29)
{
  p = (-0.81 * (y - 1 * 175.35)) + 393.64;
}
}

```

```

else if (y >= 165.22)
{
    p = (-0.43 * (y - 1 * 170.29)) + 397.74;
}
else if (y >= 160.16)
{
    p = (-1.05 * (y - 1 * 165.22)) + 399.93;
}
else if (y >= 155.10)
{
    p = (-1.12 * (y - 1 * 160.16)) + 405.24;
}
else if (y >= 150.03)
{
    p = (-1.40 * (y - 1 * 155.10)) + 410.91;
}
else if (y >= 146.99)
{
    p = (-1.33 * (y - 1 * 150.03)) + 417.99;
}
else if (y >= 142.94)
{
    p = (-0.56 * (y - 1 * 146.99)) + 422.04;
}
else if (y >= 136.87)
{
    p = (-0.18 * (y - 1 * 142.94)) + 424.31;
}
else if (y >= 129.78)
{
    p = (-0.20 * (y - 1 * 136.87)) + 425.42;
}
else if (y >= 124.71)
{
    p = (-0.36 * (y - 1 * 129.78)) + 426.80;
}
else if (y >= 121.67)
{
    p = (-1.33 * (y - 1 * 124.71)) + 428.62;
}
else if (y >= 119.65)
{
    p = (-1.99 * (y - 1 * 121.67)) + 432.68;
}
else if (y >= 106.48)
{
    p = (-1.65 * (y - 1 * 119.65)) + 436.70;
}
else if (y >= 103.44)
{
    p = (0.00 * (y - 1 * 106.48)) + 458.45;
}
else if (y >= 93.31)
{
    p = (-0.00 * (y - 1 * 103.44)) + 458.45;
}

```

```

}
else if (y >= 75.08)
{
    p = (-0.08 * (y - 1 * 93.31)) + 458.48;
}
else if (y >= 74.07)
{
    p = (0.25 * (y - 1 * 75.08)) + 459.87;
}
else if (y >= 73.06)
{
    p = (0.00 * (y - 1 * 74.07)) + 459.61;
}
else if (y >= 72.00)
{
    p = (0.00 * (y - 1 * 73.06)) + 459.61;
}
else if (y >= 71.00)
{
    p = (0.00 * (y - 1 * 72.00)) + 459.61;
}
else if (y >= 70.00)
{
    p = (0.00 * (y - 1 * 71.00)) + 459.61;
}
else if (y >= 65.00)
{
    p = (0.12 * (y - 1 * 70.00)) + 459.61;
}
else if (y >= 50.00)
{
    p = (0.60 * (y - 1 * 65.00)) + 459.03;
}
else if (y >= 25.00)
{
    p = (0.15 * (y - 1 * 50.00)) + 450.07;
}
else if (y >= 0.00)
{
    p = (0.11 * (y - 1 * 25.00)) + 446.20;
}
else if (y >= -25.00)
{
    p = (0.03 * (y - 1 * 0.00)) + 443.52;
}
else if (y >= -50.00)
{
    p = (-0.04 * (y - 1 * -25.00)) + 442.78;
}
else if (y >= -75.00)
{
    p = (-0.12 * (y - 1 * -50.00)) + 443.68;
}
else if (y >= -100.00)
{

```

```

        p = (-0.15 * (y - 1 * -75.00)) + 446.64;
    }
    else if (y >= -125.00)
    {
        p = (-0.19 * (y - 1 * -100.00)) + 450.31;
    }
    else if (y >= -150.00)
    {
        p = (-0.22 * (y - 1 * -125.00)) + 455.12;
    }
    else if (y >= -175.00)
    {
        p = (-0.23 * (y - 1 * -150.00)) + 460.58;
    }
    else if (y >= -200.00)
    {
        p = (-0.23 * (y - 1 * -175.00)) + 466.37;
    }
    else if (y >= -225.00)
    {
        p = (-0.18 * (y - 1 * -200.00)) + 472.07;
    }
    else if (y >= -250.00)
    {
        p = (-0.02 * (y - 1 * -225.00)) + 476.68;
    }
    else
    {
        p = 478.0;
    }
    F_PROFILE(f, t, i) = p;
}
end_f_loop(f, t)
#endif
}

```

```

DEFINE_PROFILE(seepage_velocity_profile, t, i)
{
    #if PARALLEL
        real x[ND_ND]; /*location vector*/
        real y; /*depth*/
        real p;
        face_t f;
        begin_f_loop(f, t)
        {
            F_CENTROID(x, f, t); /*centroid of the cell*/
            y = x[1];

            if (y >= 230.00)
            {
                p = 0.0;
            }
            else if (y >= 210.00)

```

```
    {
      p = 5e-5;
    }
    else if (y >= 110.00)
    {
      p = 1e-6;
    }
    else if (y >= 65.00)
    {
      p = 7e-6;
    }

    else
    {
      p = 0;
    }
    F_PROFILE(f, t, i) = p;
  }
  end_f_loop(f, t)
#endif
}
```

## **Appendix B : Seepage velocity calibration**

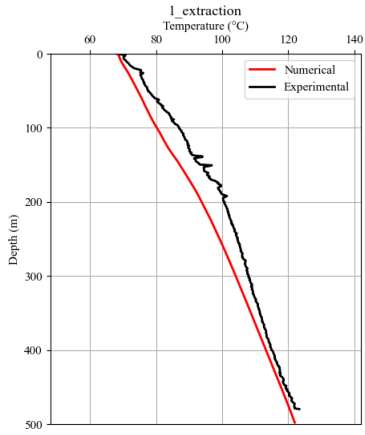
This appendix belongs to Chapter 4. In this section, the temperature profile results of some of the representative cases are discussed to give readers an idea of the seepage calibration process during the numerical simulation. One of these cases assumes that the entire domain is purely conductive, while other cases assume a seepage velocity more or less than the calibrated seepage velocity.

### **Case I: Pure conductive case**

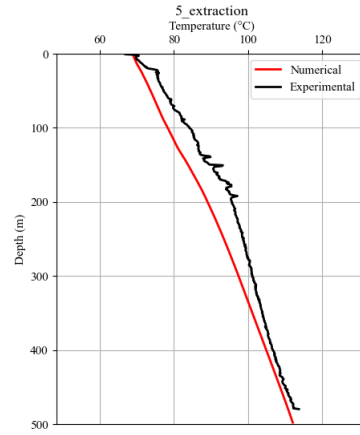
In the case of pure conductivity, where there was no presence of seepage, as displayed in Figure Appendix-1, subplots (a), (b), (c), and (d) show the temperature profiles during extraction, while subplots (e), (f), (g), and (h) depict the temperature profiles during the recovery period. As seen in the figure, with the pure conductive model, the numerical temperature profiles are lower than those of the experimental profiles both during extraction and the recovery period. It should also be noted that the recovery temperature profiles at depths of 185-500 m match this model. Following this, several trials were conducted to find seepage velocity values that could potentially align with both the extraction and recovery curves.

(a)

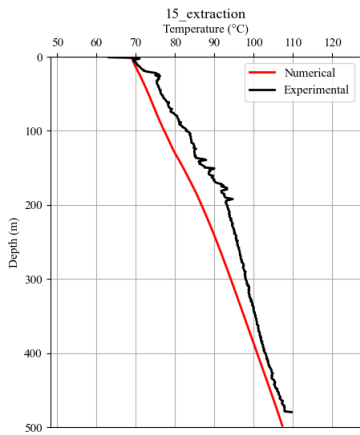
(b)



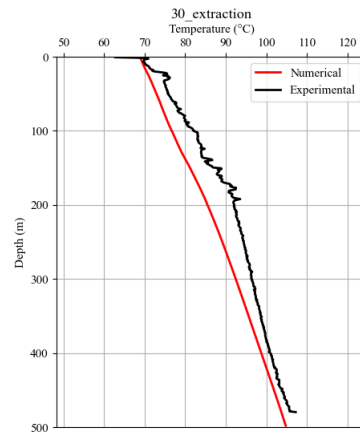
(c)



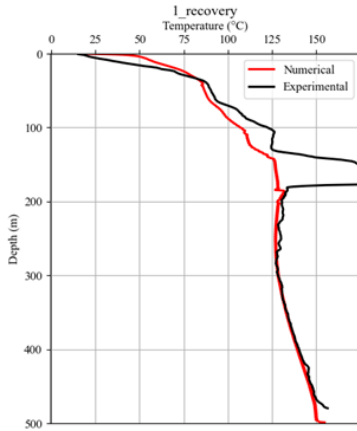
(d)



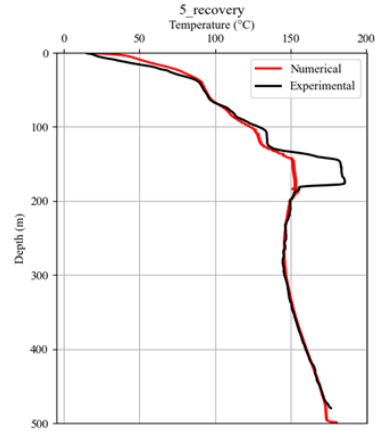
(e)



(f)



(g)



(h)

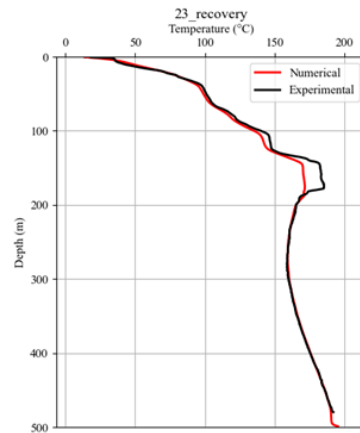
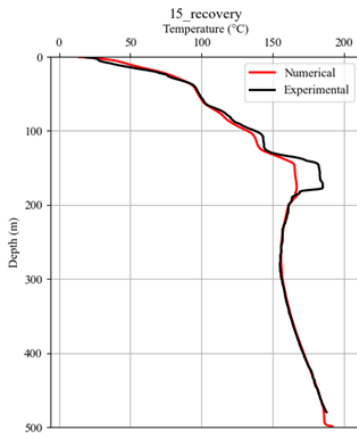


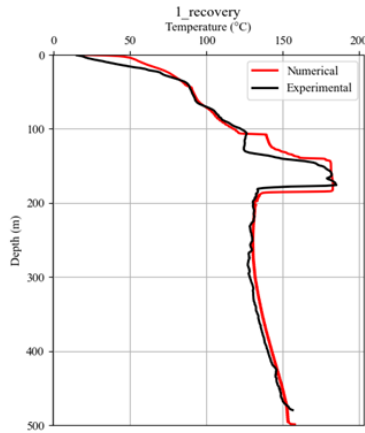
Figure Appendix-1. Extraction and recovery temperature profiles with pure conduction model.

**Case II: Seepage layer of 62.6 m/year at depths of 100-140 m**

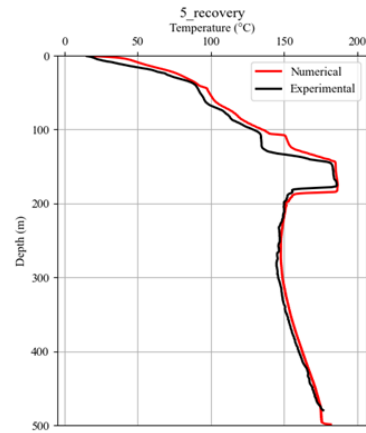
In this section, we report a case in which the seepage velocity was assumed to be higher than the calibrated seepage velocity mentioned in Chapter 4 for this specific depth. The calibrated seepage velocity at this depth is 31.5 m/year. However, if the seepage velocity at this depth were to increase to 62.6 m/year, then the temperature profiles, specifically during the recovery period, would not match, as shown in Figure 2(a), Figure 2(b), Figure 2(c), and Figure 2(d).

(a)

(b)



(c)



(d)

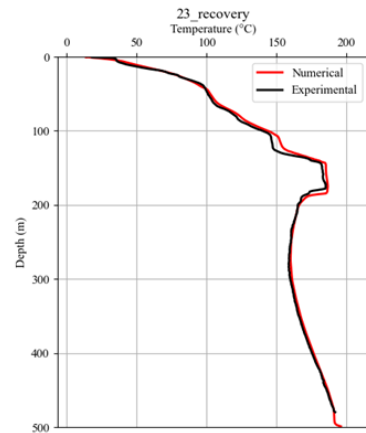
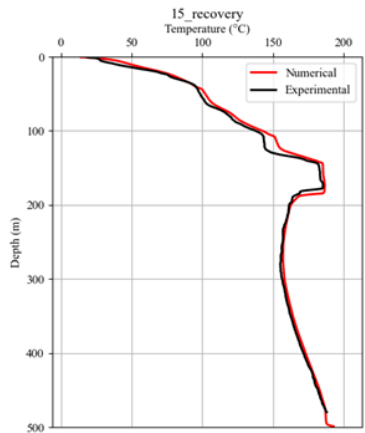
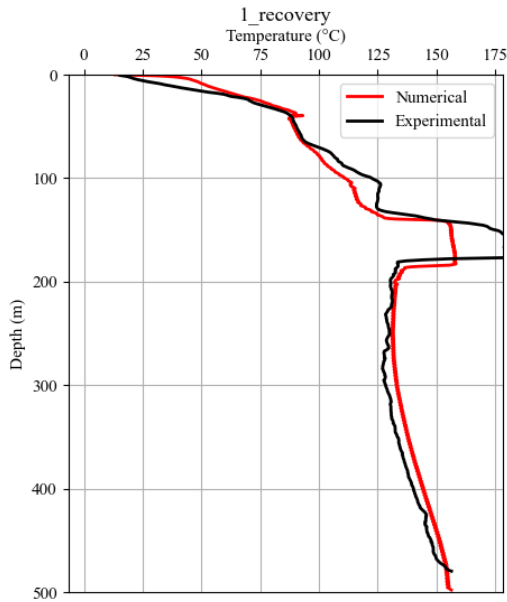


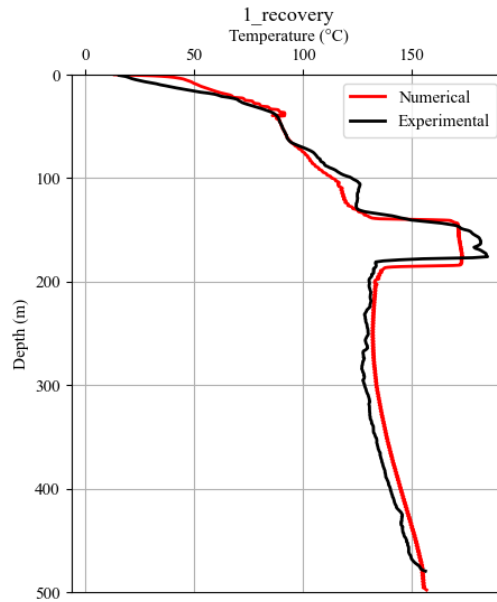
Figure Appendix-2. Recovery temperature profiles with an assumed seepage velocity of 250.5 m/year at a depth of 100-145 m.

**Case III: Seepage velocity smaller than calibrated velocity from 140-185 m**

Similarly, for the depth of 140-185 m, some recovery results for the first day of recovery are presented for smaller velocities than that of the calibrated velocity.



(a)



(b)

Figure Appendix-3: Recovery temperature profile on the first day of recovery for seepage velocities of (a) 55.1 m/year and (b) 110.2 m/year in the depth of 140-185 m.

## Appendix C :Other publications

A journal publication by the author during the Ph.D. studies but not included in this thesis is:

1. **Pokhrel, S.**, Kuyuk, A. F., Kalantari, H., & Ghoreishi-Madiseh, S. A. (2020). Techno-economic trade-off between battery storage and ice thermal energy storage for application in renewable mine cooling system. *Applied Sciences*, 10(17), 6022.